An investigation into the activation of methane using a tuneable femtosecond laser system

Martin Lombaard
12626961



NORTH-WEST UNIVERSITY
YUNIBESITI YA BOKONE-BOPHIRIMA
NOORDWES-UNIVERSITEIT
POTCHEFSTROOM CAMPUS

Dissertation submitted in partial fulfilment of the degree
Magister Scientiae in Chemistry
at North-West University

Supervisor: *Prof. C.A. Strydom*
Co-supervisor: *Dr. T. Dlamini*

November 2008

Declaration

I ..Martin Lombaard....., hereby declare that the work contained in this dissertation is my own original work and that I have not submitted it at any other university.

Signature.....

Date.....14/05/07.....

Dedicated to my Lord and Saviour...
Jesus Christ

Acknowledgements:

I would like to take the opportunity to thank the following persons and instances for their respective contributions:

- Prof. Christien Strydom and Dr. Thulani Dlamini for all their support and valuable insets to the study,
- Dr. Cornie van Sittert for all the support and advice on the molecular modelling,
- Dr. Anton du Plessis and Dr. Lourens Botha for all the advice, support and suggestions on the experimental work,
- Mr. Henk van Wyk and Mr. Hendrik Maat for all the technical support and assistance during the laser experiments in the laboratory,
- Mr. Jaco Kotze for the constant support and involvement in the laboratory,
- Mr. Dave Geddes for the language and grammar corrections of the dissertation,
- The NWU, SANHARP and NLC at CSIR for the technical- and financial support of this study,
- Ms. Nadine Hanekom for the prayers and emotional support throughout the study,
- My family and friends for the encouragement and constant support.

Lord, thank you for giving me strength, faith, perseverance and the opportunity to complete this study.

Father, I have knowledge
so I pray You'll show me now
How to use it wisely
and find a way somehow
To make the world I live in
a little better place,
And make life, with its problems,
a bit easier to face...
Grant me faith and courage
and put purpose in my days,
And show me how to serve Thee
in the most effective ways
So all my education,
my knowledge and my skill,
May find their true fulfilment
as I learn to do Thy will...
And may I ever be aware
in everything I do
That knowledge comes from learning -
And wisdom comes from You.

Helen Steiner Rice

Abstract:

Using a tuneable femtosecond- and nanosecond laser system at room temperature, it was observed that by photo-irradiation in the infrared region, methane can be photo-excited to undergo the coupling reaction in which ethane and hydrogen is formed. In similar conditions, the addition of carbon dioxide results in the formation of carbon monoxide through the photoreduction of carbon dioxide by methane.

Molecular modelling calculations were used to determine the photoabsorption wavelength needed for C–H bond activation of methane. Calculations showed that the $2\nu_3$ overtone at 1.67 μm was ideal for excitation. Fourier transform infrared spectroscopy was used to analyze the samples after excitation. These results suggested that partial dehydrogenation of ethane to ethylene also occurred during the coupling reaction of methane while traces of methanol were found in the CH_4/CO_2 mixture after excitation.

Although pleasing results were obtained with the nanosecond laser system, the femtosecond laser system proved more reliable and efficient.

Opsomming:

Die gebruik van 'n verstelbare femto- en nanosekonde laser stelsel by kamer temperatuur, het getoon dat deur bestraling in die infrarooi gebied kan metaan fotonies opgewek word om die koppelings reaksie waarin etaan en waterstof gevorm word, ondergaan. Onder soortgelyke kondisies het die toevoeging van koolstof dioksied gelei tot die vorming van koolstof monoksied deur die fotoreduksie van koolstof dioksied deur metaan.

Molekuulmodelering is gebruik om die fotoabsorpsie golflengte, benodig vir C–H bandaktivering, te bepaal. Berekeninge het getoon dat die $2\nu_3$ bo-toonvibrasie by 1.67 μm idiaal is vir opwekking. Fourier transform infrarooi spectroskopie is gebruik om die monsters te analiseer na opwekking. Hierdie resultate het aangedui dat gedeeltlike dehidrogenasie van etaan na etyleen ook plaas gevind het gedurende die koppelingsreaksie van metaan, asook dat daar aanduidings was van methanol ná die opwekking van die CH_4/CO_2 mengsel.

Alhoewel gunstige resultate verkry is met die nanosekonde laser stelsel, het die femtosekonde laser stelsel 'n hoër doeltreffendheid gehad.

Table of contents:

Acknowledgements i

Abstract v

Opsomming vii

Table of contents ix

Abbreviations xiii

Part 1 Introduction

Chapter 1: Introduction and purpose of study 2

1.1 Introduction 3
1.2 Aims of study 5

Part 2 Literature

Chapter 2: Background on methane 9

2.1 General 10
2.1.1 Structural- and thermodynamic properties 13
2.1.1.1 Bond dissociation energy 13
2.1.1.2 Rotational energy 14
2.1.1.3 Vibrational energy 15
2.1.1.4 Molecular- and electronic structure 16
2.1.2 Uses 22
2.1.2.1 Fuel 23
2.1.2.2 Industrial uses 23
2.1.3 Sources of methane 23
2.1.3.1 Natural gas fields 23
2.1.3.2 Alternative sources 24

2.2 Activation of methane 25
2.2.1 Activation via metal catalysts 25
2.2.2 Photoexcitation of methane 30

Chapter 3: Computational chemistry methods 33

3.1 Introduction and history 34
3.2 Development of models 35
3.3 Molecular mechanics 36
3.3.1 Basic theory 36
3.3.2 Force field models 37
3.4 Quantum mechanical models 38
3.4.1 Basic theory 38
3.4.2 Ab initio approximations 38
3.5 Semi-Empirical methods 40
3.5.1 Basic theory 40
3.5.2 Various semi-empirical methods 41
3.6 Density functional theory 43
3.6.1 Basic theory 43
3.6.2 Common basis sets 44

Chapter 4: Background on photochemistry 46

4.1 The nature of light 47
4.2 Absorption and emission of radiation 48
4.3 Electronic excitation 50
4.4 Wave mechanics and quantum numbers 51
4.5 Fates of excited species 52
4.6 Multiphoton photochemistry 53
4.7 Lasers 55
4.8 Femtochemistry 57
4.8.1 Introduction 57
4.8.2 Coherent control 58
4.8.3 Mode-locking 60

4.8.4 Pump-probe technique 62

Part 3 Experimental

Chapter 5: Experimental methods and procedures 67

5.1 Molecular modelling 68
5.1.1 Hardware 68
5.1.2 Software 68
5.2 Excitation reactions 70
5.2.1 Reagents 70
5.2.2 Nanosecond excitation reactions 71
5.2.2.1 Equipment 71
5.2.2.2 Important calculations and specifications 76
5.2.2.3 Experimental setup and procedures 78
5.2.3 Femtosecond excitation reactions 80
5.2.3.1 Equipment 80
5.2.3.2 Experimental setup and procedures 85

Part 4 Discussion and Conclusion

Chapter 6: Results and discussion 88

6.1 Molecular modelling 89
6.1.1 Geometry optimization calculations for methane 89
6.1.2 Electronic state calculations for methane 94
6.1.3 Excited state calculations for methane 96
6.1.4 Vibrational state calculations for methane 99
6.1.5 Calculations for reactions of methane 103
6.1.5.1 Methane reacting with itself 103
6.1.5.2 Methane reacting with carbon dioxide 106

6.2 Nanosecond excitation reactions 110
6.2.1 Methane reacting with itself 110
6.2.1.1 Without laser excitation 110
6.2.1.2 Excitation at 1.6 μm 112
6.2.1.2.1 Three hours experiment 112
6.2.1.2.2 Five hours experiment 116
6.2.2 Methane and carbon dioxide reactions 120
6.2.2.1 Without laser excitation 120
6.2.2.2 Excitation at 1.6 μm 122
6.2.2.2.1 Three hours experiment 122
6.2.2.2.2 Five hours experiment 127
6.3 Femtosecond excitation reactions 131
6.3.1 Methane reacting with itself 131
6.3.1.1 Three hours experiment 132
6.3.1.2 Five hours experiment 134
6.3.2 Methane and carbon dioxide reactions 137
6.3.2.1 Three hours experiment 137
6.3.2.2 Five hours experiment 140

Chapter 7: Summary and conclusions 145

7.1 Summary 146
7.1.1 Molecular modelling 146
7.1.2 Excitation experiments 148
7.2 Conclusion and recommendations 155

Bibliography 158

Abbreviations:

ΔG	:	Gibbs energy change
ΔH	:	Enthalpy change
A	:	Singular
ASE	:	Amplified spontaneous emission
$CH3^{\cdot}$	:	Methyl radical
CPU	:	Central processing unit
DFT	:	Density functional theory
DMR	:	Double Mixed Refrigerant process
DRM	:	Dry reforming process of methane
FTIR	:	Fourier transform infrared spectroscopy
GC	:	Gas chromatography
HCHO	:	Formaldehyde
HCO	:	Formyl radical
HF	:	Hartree-Fock
HOMO	:	Highest occupied molecular orbital
$h\nu$	:	Energy of a photon (Planck's constant multiplied by speed of light)
$\hbar\omega_{L\alpha}$	:	Light (radiation) at Lyman-alpha wavelength
IR	:	Infrared
LCAO	:	Linear combination of atomic orbital
LNG	:	Liquefied natural gas

LUMO	:	Lowest unoccupied molecular orbital
Lyman-α	:	Lyman-alpha wavelength
MIR	:	Mid-infrared
MMFF	:	Merck Molecular Force Field
MP	:	Møller-Plesset
MR	:	Mixed refrigerant
MTG	:	Methanol to gasoline process
Nd:YAG	:	Neodymium-doped yttrium aluminium garnet crystal
Nd:YVO_4	:	Neodymium-doped Yttrium Vanadate crystal
NG	:	Natural gas
NIR	:	Near-infrared
NOCM	:	Non-oxidative coupling of methane
OCM	:	Oxidative coupling of methane
OPO	:	Optical parametric oscillators
OPPO	:	Optical Parametric Power Oscillator
PES	:	Potential energy surface
PMR	:	Pre-cooled mixed refrigerant
POM	:	Partial oxidation process
RHF	:	Restricted Hartree-Fock
S	:	Spin multiplicity
SCF	:	Self consistent field method
SE	:	Semi-Empirical

SRM	:	Steam reforming method
Std	:	Standard
T	:	Triple degenerate
Ti:Sapphire	:	Titanium-doped Sapphire crystal
TOF MS	:	Time-of-flight mass spectroscopy
USA	:	united States of America
UV	:	Ultraviolet
VUV	:	Vacuum ultraviolet
π	:	Pi
σ	:	Sigma
Φ	:	Orientation wavefunction
Ψ	:	Wavefunction

Part 1

Introduction

Chapter 1

Introduction and purpose of study

1.1 Introduction

A research field in chemistry called photochemistry studies the interactions between atoms and/or molecules with light. These interactions are stimulated by the absorption of electromagnetic radiation (photons) by the atoms and/or molecules. The absorption of photons then may lead to photoionization or photo-excitation of the molecules according to Planck's Quantum Theory [http://www.thebigview.com/]. The mechanism involves an electron that absorbs the energy of a photon which then causes it to move to a higher energy state. This increase in energy can then provide the activation energy needed for the reaction to occur.

Photon absorption may also bring change to the symmetry of the molecule's electronic configuration which results in previously inaccessible reactions, to occur. This attribute makes photon absorption an ideal technique to activate reactants under normal conditions for reactions that require high activation energies.

One modern, specialized field in photochemistry that utilizes laser radiation to activate atomic- and/or molecular systems is called femtochemistry. Femtochemistry is the science that studies chemical reactions on extremely short timescales, approximately 10^{-15} seconds (this is one femtosecond, hence the name). The technique addresses the short timescale in which the chemical reactions take place by using ultra fast laser pulses as a means to activate the atoms or molecules. These pulses are high in energy and generated by a complex Ti:Sapphire-based laser system.

The rate at which a chemical reaction occurs, is determined by the forces that hold the atoms together in a molecule (stability of the molecule). For this reason, chemical reactions occur at varying velocities with reaction durations ranging from a few picoseconds to many years. The rate can be increased by increasing the temperature and/or pressure or by using a catalyst. These reaction enhancements provide a means of overcoming the activation barrier needed for the reaction to take place. However, what makes femtochemistry different from any other activation technique is the time-scale of the laser pulses (10-100 femtoseconds). These pulse durations are of the same magnitude as the vibrations between the atoms in molecules. As a result, the technique can be used to activate a molecule through excitation of the vibrational- or electronic state while at the same time, give information regarding the intermediate (transition) state. The technique can

even be used to investigate and better understand processes on surfaces such as catalysts.

As a result of recent events caused by climate change, a large rise in interest on the contributors to global warming and their resulting effects and posed dangers, has occurred. In particular, the two main contributing greenhouse gasses, methane and carbon dioxide, have received the most attention [http://www.ecobridge.org/]. Studies have shown that atmospheric concentrations of these two molecules have increased dramatically since the 1970's and that they had the greatest impact on the recent change in climate [Hansen, 2000]. For this reason, research on these two molecules' chemical properties and uses has increased [Solomon, et al., 2007].

The dry reforming process of methane (DRM), which involves the reaction of methane and carbon dioxide, is a way of converting these problematic, yet stable molecules into useful products with the use of catalysts [Wei, 2004, 43; Jachimowski, 1997; Seets,1997; Ross, 2005; Hu, 2004].

$$CH_4 + CO_2 \xrightarrow[catalyst]{} 2CO + 2H_2,\ \Delta G^0_{298\ K} = 170\ \text{kJ/mol}$$

The stability of the molecules cause the reaction to require a large amount of energy to take place, as can be seen from the large change in Gibbs energy. However, a recent study by Yuliati and co-workers [Yuliati, 2008] has shown that by using a gallium oxide-catalyst at mild temperatures (473 K) the photoreduction of carbon dioxide to carbon monoxide by methane can photocatalytically be achieved through UV-irradiation. By using light together with a photocatalyst, the thermodynamic barrier can more easily be overcome.

$$CH_4 + CO_2 + h\nu + \Delta \xrightarrow[Ga_2O_3]{} 2CO + 2H_2,\ \Delta G^0_{473\ K} = 126\ \text{kJ/mol}$$

Yuliati and co-workers also investigated the non-oxidative coupling of methane (NOCM) to ethane and hydrogen and successfully proved that the reaction could photocatalytically proceed at room temperature for the gallium oxide photocatalyst, silica-based photocatalysts [Yuliati, Itoh, 2006], zeolites [Kato, 2002], mesoporous silica [Yuliati, Tsubota, 2006], and ceria-based photocatalysts [Yuliati, 2005].

$$2CH_4 + h\nu \xrightarrow[Ga_2O_3]{} C_2H_6 + H_2,\ \Delta G^0_{298\ K} = 68.6\ \text{kJ/mol}$$

The results showed that for the NOCM, it was easier for the reaction to occur at room temperature than at higher temperatures.

$$2CH_4 + h\nu + \Delta \xrightarrow[Ga_2O_3]{} C_2H_6 + H_2,\ \Delta G^0_{473\ K} = 70.7\ \text{kJ/mol}$$

The advantages of using photo-irradiation together with a photocatalyst, to enhance the efficiency and rate of a reaction, can be seen from this example. The common problems normally associated with high temperatures and stable catalysts, such as deactivation of the catalyst, can now through process selectivity be avoided by irradiating the photocatalyst. The disadvantage however of using this technique is that the reaction mechanisms are difficult to understand and determine for reactions with heterogeneous catalysts. Thus, alternative or altered methods for activating reactions need to be investigated.

For the above mentioned reasons, this study will comprise the use of special laser systems to excite these stable molecules and potentially initiate the discussed reactions without the use of photocatalysts.

1.2 Aims of the Study

The inter-related aims of this research project are:

- To investigate and analyze methane in its ground- and excited state by using molecular modelling,
- To use molecular modelling to investigate the reaction of methane with carbon dioxide,
- To use molecular modelling to investigate the reaction of methane with itself to form ethane,
- To construct and use the molecular orbital diagram of methane to discuss the electronic state of the molecule,
- To conduct experiments where methane is excited by means of a nanosecond- and femtosecond laser system,
- To use Fourier transform infrared spectroscopy to analyze the samples after the excitation process,

- To compare results of laser induced experiments with findings of molecular modelling,
- To compare results of nanosecond experiments with results of femtosecond experiments,
- To compare the efficiency of laser induced processes with processes described in literature that use metal catalysts,
- To determine problems associated with laser photo-excitation,
- To make suggestions for optimizing future laser photo-activated experiments.

Part 2

Literature

Chapter 2

Background on methane

2.1 General

Methane is the simplest hydrocarbon known to man. The molecule consists of a centre carbon atom which has four hydrogen atoms bonded to it. The bonds are covalent and separated by an angle of 109.5°. This gives the molecule a tetrahedral shape. Methane was first produced in 1902 by Sabatier and Senderens by passing a mixture of hydrogen and the oxides of carbon over divided metals [Sabatier, 1902]. The purpose of the study was to develop catalysts that could be used in the methanation of synthesis gas.

The combustion process, employed for energy production, involves one mole of methane reacting with two moles of oxygen to produce one mole of carbon dioxide and two moles of water:

$$CH_4\,(g) + 2O_2\,(g) \rightarrow CO_2\,(g) + 2H_2O\,(g)$$

Several steps are involved in the mechanism of the combustion of methane. In the first heat-treatment step, it is believed that methane forms a methyl radical ($CH3^{\cdot}$) which then reacts with oxygen to form formaldehyde (HCHO). The formaldehyde gives a formyl radical (HCO), which then forms carbon monoxide (CO). This process is called oxidative pyrolysis [Chen, 1997]:

$$CH_4\,(g) + O_2\,(g) \rightarrow CO\,(g) + H_2\,(g) + H_2O\,(g)$$

Following oxidative pyrolysis, the H_2 oxides to form H_2O.

$$H_2\,(g) + \tfrac{1}{2}O_2\,(g) \rightarrow H_2O\,(g)$$

Finally, the CO oxides and forms CO_2. This is an exothermic reaction.

$$CO\,(g) + \tfrac{1}{2}O_2\,(g) \rightarrow CO_2\,(g)$$

The partial oxidation of methane (POM) and steam reforming method (SRM) are known common petrochemical processes for the production of synthesis gas (CO and H_2) and other hydrocarbons from methane.

As a result of the oxidation of methane that leads to the production of carbon dioxide, it is considered a potent greenhouse gas. It is in fact the largest non-CO_2 contributor to global warming and is about 21 times more powerful a greenhouse gas than CO_2 [http://en.wikipedia.org/wiki/Methane].

At room temperature and standard pressure, methane is a colourless, odourless gas. Large amounts of this gas are trapped in so-called gas pockets inside the earth's crust and because of its high abundance and clean burning process it is a very attractive fuel. In order to use and transport the gas to areas that consume it, it is turned into methanol. The Double Mixed Refrigerant process (DMR) by Shell is a process that turns untreated gas into liquefied natural gas (LNG) [http://www.hydrocarbons-technology.com/].

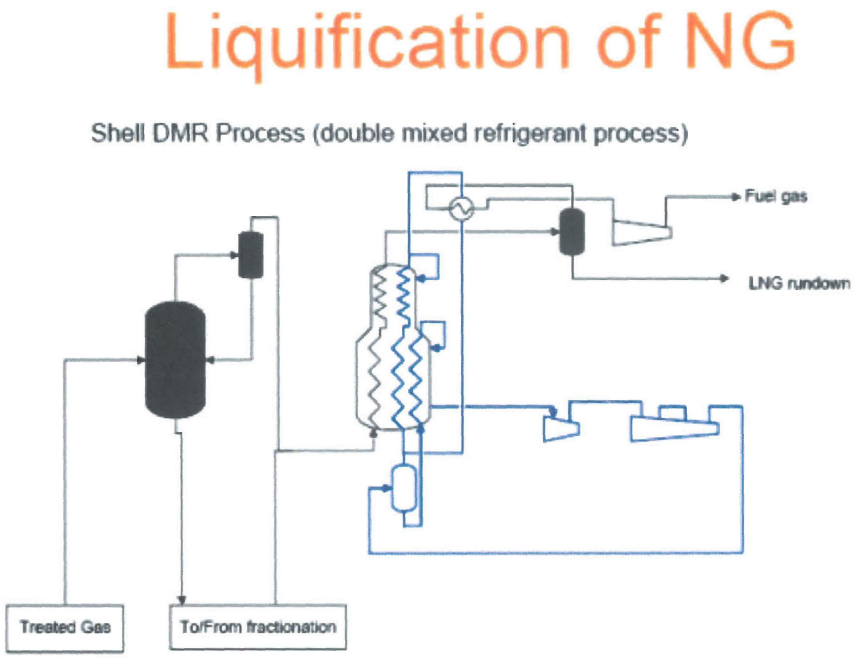

Figure 2.1 The liquefaction of natural gas [http://www.hydrocarbons-technology.com/].

The process configuration is similar to the propane pre-cooled mixed refrigerant (PMR) process, with the pre-cooling conducted by a mixed refrigerant (mainly ethane and propane) rather than pure propane. PMR vapor from the pre-cool exchangers is routed via knock-out vessels to a two stage centrifugal PMR

compressor which is powered by a single gas turbine. The cooling for liquefaction of the natural gas is provided by a second mixed refrigerant cooling cycle (MR cycle). This cycle's refrigerant consists of a mixture of nitrogen, methane, ethane and propane. The liquefaction process uses coil-wound type cryogenic heat exchangers for both the pre-cooling and the main cooling cycle. Inter-cooling and initial de-superheating is achieved by air cooling. The mixed refrigerant vapor and liquid are separated, and further cooled in the main cryogenic heat exchanger [http://www.worldoil.com].

Methane is produced by a number of sources, including coal mining and landfills. The number one worldwide source is however, animal agriculture. This is the cause of between 35 and 50% of the planet's human-induced warming. The process involves large quantities of methane being produced by a process called methanogenesis which is the production of CH_4 and CO_2 through biological processes that are carried out by methanogens. It can be considered as a form of anaerobic respiration [Thauer, 1998].

Other properties of methane include a boiling point of -162 °C at one atmosphere, highly flammable gas in concentrations between 5-15% in the air and it is non-toxic to humans and animals [http://en.wikipedia.org/wiki/Methane].

2.1.1 Structural- and thermodynamic properties

2.1.1.1 Bond dissociation energy

The thermodynic properties of methane are summarized in table 2.1.
Table 2.1 Phase behaviour and gas properties of methane

	Property	Value
Phase behavior		
	Triple point	90.67 K (-182.48 °C), 0.117 bar
	Critical point	190.6 k (-82.6 °C), 46 bar
	Std enthalpy change of fusion	1.1 kJ/mol
	Std enthalpy change of vaporization	8.17 kJ/mol
Gas Properties		
	Std enthalpy change of formation	- 74.87 kJ/mol
	Std molar entropy	188 J/(mol.K)
	Heat capacity	35.69 J/(mol.K)

[http://en.wikipedia.org/wiki/Methane]

Bond dissociation energy is usually expressed in terms of an enthalpy change (ΔH) required to break the bonds of a mole of CH_4–molecules in the gas phase. We can calculate the bond energy of methane by using a step-by-step decomposition method which is the average energy needed to break all bonds.

Decomposition Step		Energy Needed(kJ/mol)
$CH_{4(g)} \rightarrow CH_3^{\cdot} + H^{\cdot}$		435
$CH_3^{\cdot} \rightarrow CH_2^{\cdot} + H^{\cdot}$		453
$CH_2^{\cdot} \rightarrow CH^{\cdot} + H^{\cdot}$		425
$CH^{\cdot} \rightarrow C^{\cdot} + H^{\cdot}$		339
	Total =	1652
	Average =	413

These results tell us that the chemical environment of a bond affects its dissociation energy: breaking the first C–H-bond in methane is easier than breaking the second but more difficult than breaking the third or fourth bonds.

2.1.1.2 Rotational energy

The energy levels of molecules free to rotate are quantized and very little energy is needed to change the state of rotation of a molecule.

Methane is a spherical rotor, a special case of a symmetric rotor, which can be described as a rigid body with three equal moments of inertia. The moment of inertia of a molecule is the mass of each atom multiplied by the square of its distance from the axis of rotation:

$$I = \sum_i m_i r_i^2$$

Methane's energy levels are very simple because when $I_{\parallel} = I_{\perp}$, the rotational constants A and B are equal and

$$E_J = hBJ(J+1)$$

However, the gross selection rule for observing rotational transitions is that the molecule must be polar, therefore methane does not have a rotational spectrum.

2.1.1.3 Vibrational energy

All molecules are capable of vibrating and can be excited by the absorption of electromagnetic radiation. Methods like infrared spectroscopy use infrared light to excite the vibrational states of molecules and give an IR-spectrum that is characteristic of that molecule. However, for a molecule to be infrared active the electric dipole moment must change during the vibration.

Figure 2.2 shows the IR-spectrum of methane as given in the literature [http://en.wikipedia.org/wiki/Methane]

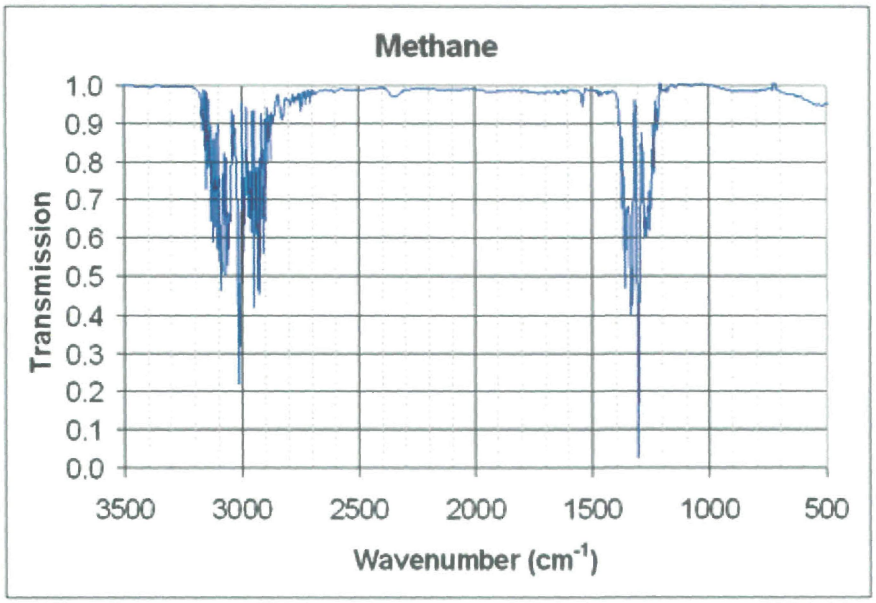

Figure 2.2 Infrared spectrum of methane.

As seen in figure 2.2 there are two characteristic sets of peaks present in the IR-spectrum of methane. The first set of peaks at ~3000 cm^{-1} is due to the C–H stretch vibrations of methane, while the second set of peaks at ~1300 cm^{-1} is due to the C–H bend vibrations.

A full detailed discussion of the IR-spectrum of methane will be given in chapter 6.

2.1.1.4 Molecular- and electronic structure

Methane has a total of four covalent bonds between the carbon and the four hydrogens. The orientation of the hydrogens around the carbon gives methane a tetrahedral shape. This is as the hybridization of the molecular orbitals of methane is sp^3.

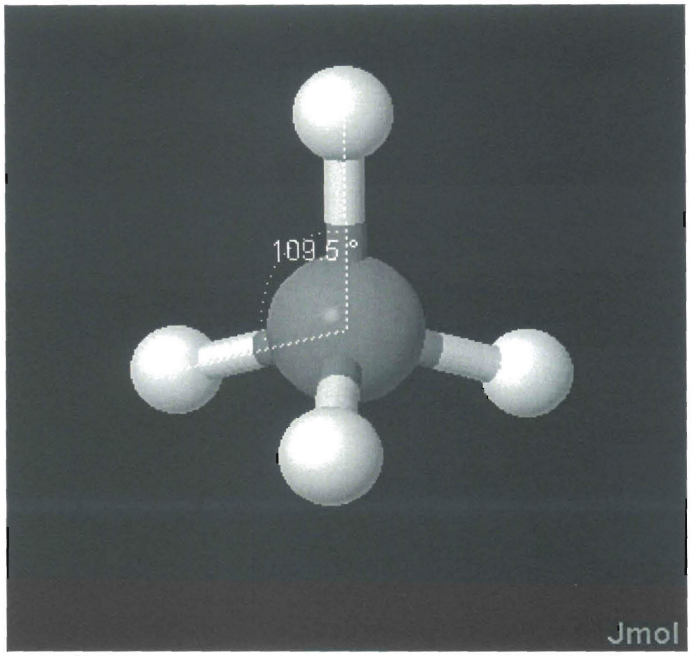

Figure 2.3 Tetrahedral shape of methane
[http://www.chemtube3d.com/vibrationsCH4.htm].

In a previous study [http://csi.chemie.tu-darmstadt] the molecular orbitals of methane were calculated using the DFT method and the B3LYP/6-311++G** basis set. A presentation of the total electron density of methane was created and is illustrated in figure 2.4. The illustration has different colours to represent the probability regions where the electrons would be found. This total electron density gives the molecule its characteristic shape.

The contributions of the atomic orbitals to the molecular orbitals are illustrated in figure 2.5. The illustration shows the formation of the sp^3 hybrid orbitals through the individual contributions of the carbon 2s, $2p_x$, $2p_y$ and $2p_z$ atomic orbitals and

the hydrogen 1s atomic orbital. These orbitals have the highest energy and are called the HOMOs (**h**ighest **o**ccupied **m**olecular **o**rbital). Figure 2.6 shows the calculated electron densities of the atomic orbital interactions with the molecular orbitals [http://csi.chemie.tu-darmstadt].

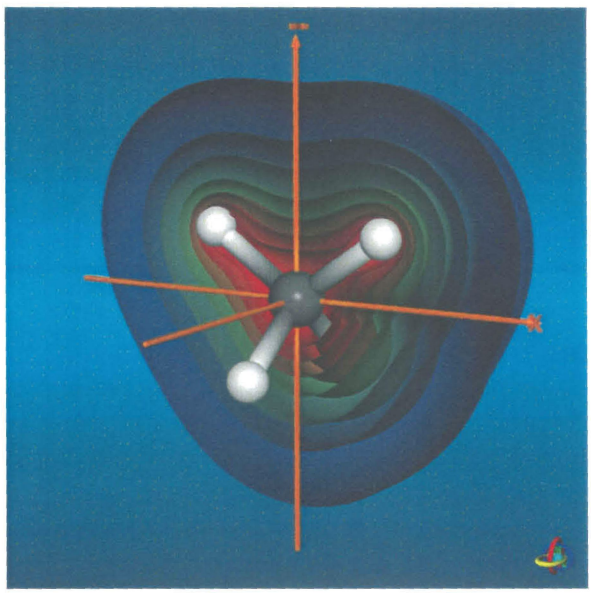

Figure 2.4 The total electron density of methane with a 99-50% probability (red to blue areas) [http://csi.chemie.tu-darmstadt].

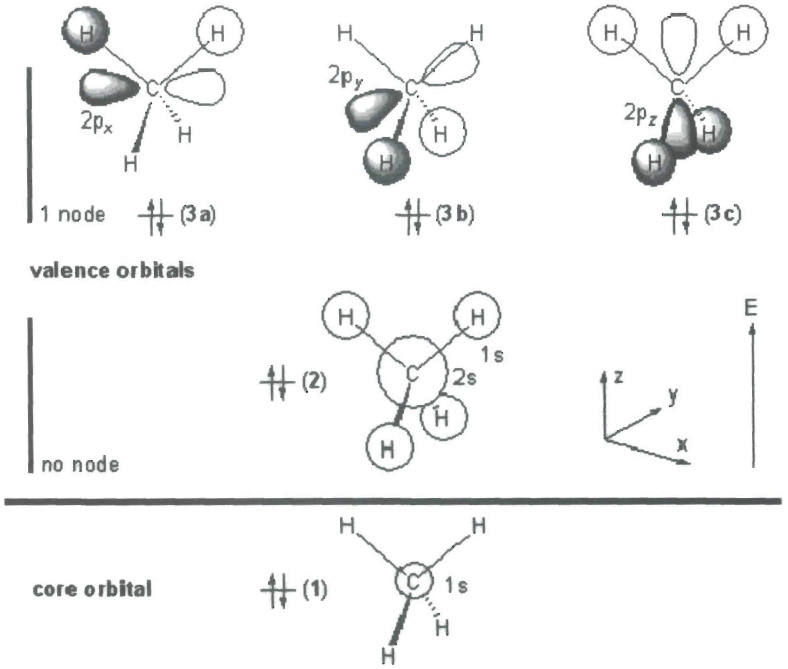

Figure 2.5 The atomic orbital contributions to the molecular orbitals of methane [http://csi.chemie.tu-darmstadt].

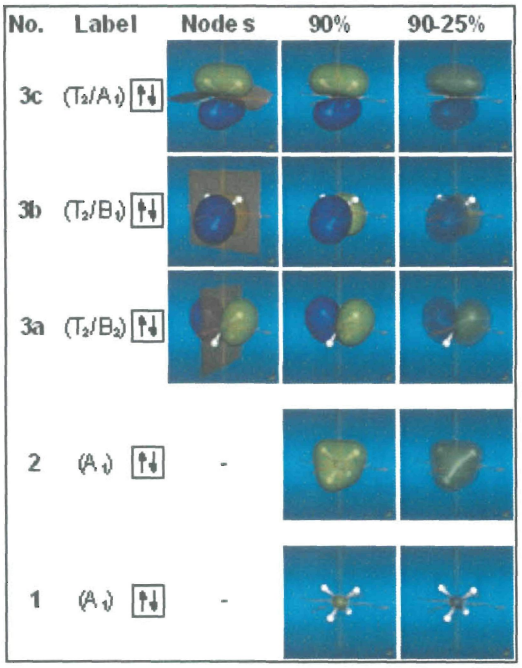

Figure 2.6 Illustrations of the electron densities of the atomic orbital interactions with the molecular orbitals [http://csi.chemie.tu-darmstadt].

The linear combination of a 2s-orbital with three 2p-orbitals ($2p_x$, $2p_y$ and $2p_z$) results in four sp^3 hybrid orbitals of identical shape but with a different orientation in space. Figure 2.7 illustrates how these combined orbitals orient themselves in space to form the basic shape of a tetrahedron. The figure also contains the wavefunctions (LCAO) that describe the hybrid orbitals.

Figure 2.8(a) and (b) show illustrations of the probability contours and the nodal plane of the sp^3-orbital. The different colours indicate the regions of opposite sign in the wavefunction (ψ). In figure 2.8(a) it is clear that the nucleus is located at the origin of the coordinate system as indicated by the orange axes, and thus is embedded not between the lobes on the nodal plane, but within the minor (blue) lobe of the hybrid orbital off the nodal plane.

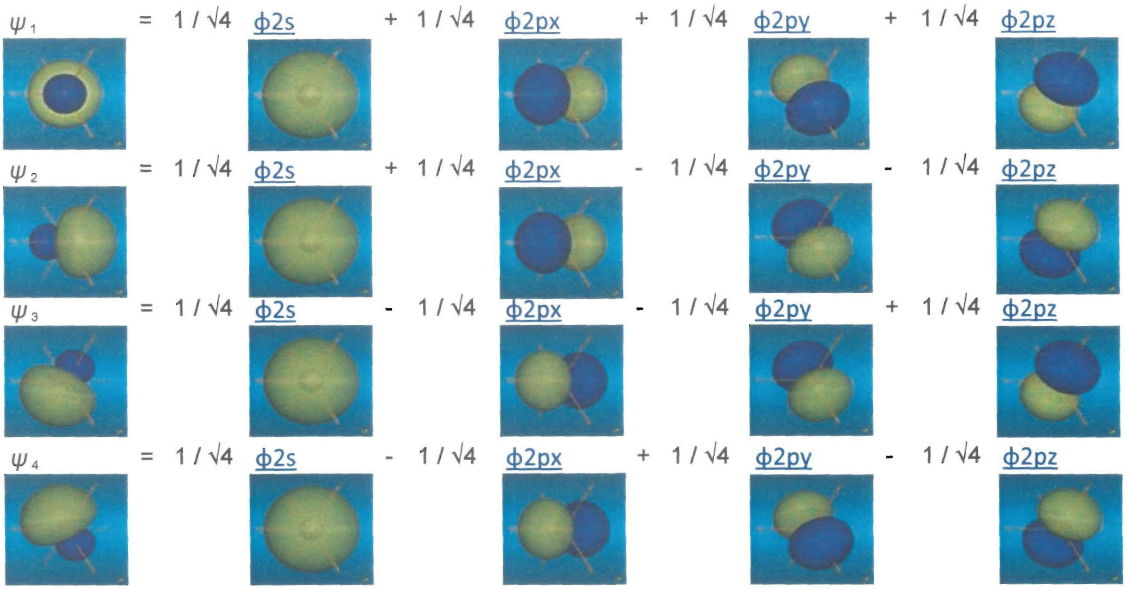

Figure 2.7 Illustration of the LCAOs with the wavefunction that describes their orientation in space [http://csi.chemie.tu-darmstadt].

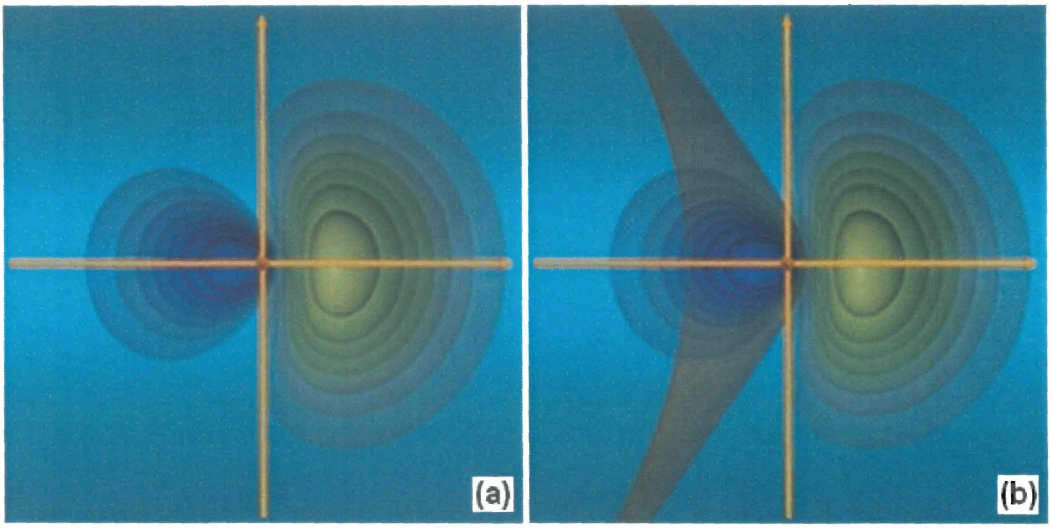

Figure 2.8(a) Illustration of the 90-25% probability contours of the sp^3-hybrid orbital (b) The nodal plane of the sp^3-hybrid orbital ($\psi = 0$) [http://csi.chemie.tu-darmstadt].

From the number of illustrations above it follows that all four of methane's bonds are identical. All of them have the same bond length (1.09Å) and all of them are separated by an angle of about 109,5° [http://www.science.uwaterloo; http://www.kayelaby.npl]. These bonds are very strong (413 kJ/mol) and this is the

reason for the stability of methane. To better understand how these C–H bonds are formed it is important to remember that the hydrogen's electron is in a 1s orbital - a spherically symmetric region of space surrounding the nucleus where there is a high probability (95%) of finding the electron. When a covalent bond is formed, the atomic orbitals (the orbitals in the individual atoms) merge to produce a new molecular orbital which contains the electron pair which creates the bond.

Figure 2.9 shows the molecular orbital diagram of methane and illustrates how the 8 valence electrons of methane are paired in the molecular orbitals. From the diagram it is clear that there is a single molecular orbital, which has a lower energy than the other molecular orbitals, and three molecular orbitals with similar energy (triple degenerate orbitals). Figure 2.10 summarizes the different symmetry species of the hydrogens of methane. This proves that methane has four bonding molecular orbitals, one that is single (A) and three that are triply degenerate (T). The remaining (unoccupied) molecular orbitals shown in figure 2.9 are the anti-bonding molecular orbitals.

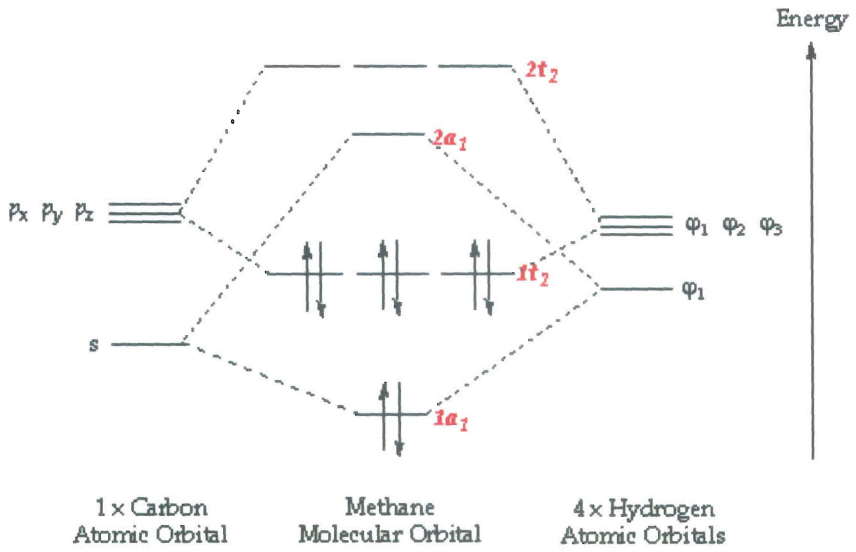

Figure 2.9 The molecular orbital diagram of methane [http://www.ch.ic.ac.uk].

Td	E	8C3	3C2	6S4	6σd
A1	1	1	1	1	1
A2	1	1	1	-1	-1
E	2	-1	2	0	0
T1	3	0	-1	1	-1
T2	3	0	-1	-1	1
χ	4	1	0	0	2

$$a(A_1) = 1/24\ \{(4x1) + 8(1x1) + 3(0x1) + 6(0x1) + 6(2x1)\} = 1$$
$$a(A_2) = 1/24\ \{(4x1) + 8(1x1) + 3(0x1) - 6(0x1) - 6(2x1)\} = 0$$
$$a(E) = 1/24\ \{(4x2) - 8(1x1) + 3(0x2) + 6(0x0) + 6(2x0)\} = 0$$
$$a(T_1) = 1/24\ \{(4x3) + 8(1x0) - 3(0x1) + 6(0x1) - 6(2x1)\} = 0$$
$$a(T_2) = 1/24\ \{(4x3) + 8(1x0) - 3(0x1) - 6(0x1) + 6(2x1)\} = 1$$

Figure 2.10 The symmetry species of the four hydrogen atoms in methane.

2.1.2 Uses

Natural gas is used in many different ways. The two most common uses for natural gas are to produce fuel for electricity, and industrial applications [http://www.naturalgas.org].

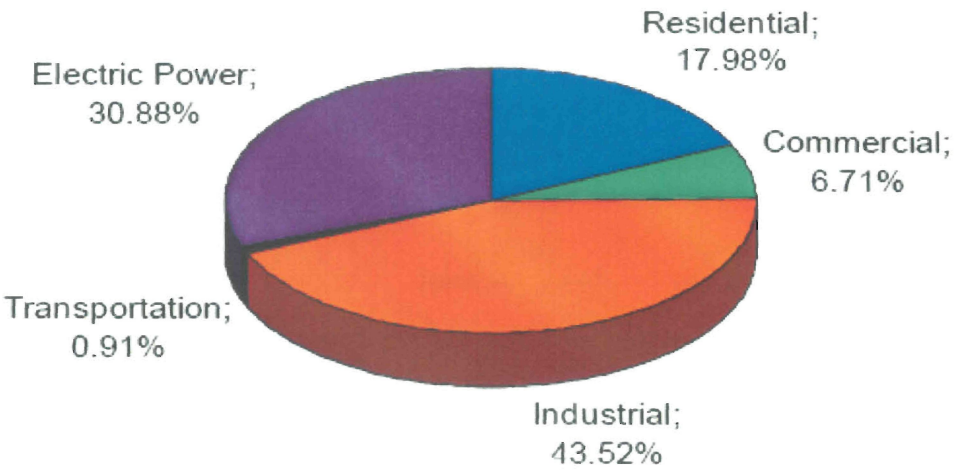

Figure 2.11 Uses of natural gas for USA [http://www.naturalgas.org].

2.1.2.1 Fuel

Methane plays an important role in the process of generating electricity for many different applications. Gas turbines use gas, air and fuel to generate electricity to power aircraft, trains, ships and generators. Comparing the heat of combustion of methane with that of other hydrocarbons reveals that methane produces more heat per unit mass than any other hydrocarbon [Sagadeev, 2004]. It also produces less carbon dioxide than any other hydrocarbon. In terms of greenhouse effects methane is far more environmentally friendly as a vehicle fuel than petrol or diesel [http://en.wikipedia.org/wiki/Methane].

2.1.2.2 Industrial uses

Petrochemical industries use methane as a building block for the production of methanol, hydrogen and other hydrocarbons. The processes first convert the methane into synthesis gas by using metal catalysts. Then the products are extracted and further processed.

In a study done by Ebrahim and Jamshidi, zinc oxide pellets are used in large zinc production industries to decrease methane emissions into the atmosphere. The reduction reaction is as follows:

$$ZnO + CH_4 \rightarrow Zn + CO + 2H_2$$

In the reaction metallic zinc is formed and methane is turned into synthesis gas with a H_2/CO ratio of 2:1. This is ideal for petrochemical processes such as Fischer-Tropsch and methanol production [Ebrahim, 2004].

2.1.3 Sources of methane

2.1.3.1 Natural gas fields

Both natural gas and oil are produced by anaerobic decay of organic matter deep inside the earth's crust. As a consequence, natural gas and oil are often found together. In general, natural gas is formed deeper in the earth's crust due to the

higher temperatures and pressures. Natural gas (NG) drilling companies extract the gas and transport it to the desired locations for processing and use. Figure 2.12 illustrates the formation of natural gas.

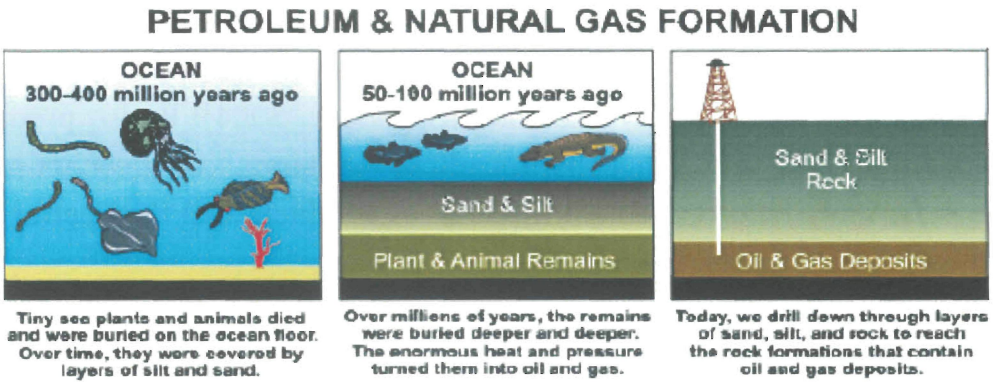

Figure 2.12 Formation of NG [http://www.fml.ethz.ch/].

2.1.3.2 Alternative sources

The process of fermentation of biodegradable organic matter (such as feedstock and wastewater) that occurs under anaerobic conditions is an alternative source of methane. Large quantities of methane hydrate are found on the sea floor. Methane hydrates are clathrate compounds, a structure in which water molecules under certain conditions bond to form an ice-like cage that encapsulates a gas molecule [Science News, 2005]. The gas hydrate is a crystalline structure which forms at large depths along geological faults as streaming gas comes in contact with the cold water. Methane hydrate is more stable at higher temperatures than liquefied natural gas (-20 and -162 °C). As a result, the process of rather transporting methane hydrate compared to liquefied natural gas seems to be a more feasible approach.

2.2 Activation of methane

Since the discovery of methane in 1902, considerable research has been done to investigate the use of methane as a fuel. These processes include reactions that produce hydrogen as well as larger hydrocarbon compounds. Many of these reactions occur through the use of metal catalysts or by photoexcitation. The following section will therefore discuss some details on previous studies performed on processes which involve the activation of methane through the use of metal catalysts (section 2.2.1) and irradiation (section 2.2.2).

2.2.1 Activation via metal catalysts

The chemical conversion processes, in which methane is converted into larger molecules in systems where metal catalysts are used, follow a specific route. These reactions make use of carbon dioxide or water to form H_2–CO mixtures over the catalysts. In the reactions the carbon dioxide or water serves as a co-reactant that reacts with the methane to form synthesis gas. The synthesis gas can then be further processed or separated. The hydrogen is of particular importance in refining, fuel cells and petrochemical processes.

Due to the stability of the molecule and the endothermic nature of reforming reactions, these reactions require stable catalysts at high temperatures [Wei, 2004, 108, 4094; Jachimowski, 1997; Seets, 1997]. However as discussed in chapter 1, the use of high temperatures pose the problem of deactivating the surface of the metal catalyst due to carbon formation. A solution for this is the use of metal clusters which influence the selectivity of the catalyst. Studies on iridium-clusters have shown that no carbon formation took place for CO_2–CH_4 reactions in contrast to the use of Group VIII metals [Mark, 1996; Rostrup-Nielsen, 1993; Ashcroft, 1991], except Pt [Wei, 2004, 108, 4094].

Studies on modelled surfaces of methane have suggested that the C-H bond activation is sensitive to surface structure [Boudart, 1969; Burghgraef, 1993] and requires unsaturated sites [McMaster, 1993; Klier, 1997].

The conversion rates of methane on many metal clusters are controlled by the C–H bond dissociation [Wei, 2004, 108, 4094; Jachimowski, 1997; Seets, 1997]. These clusters can be used as a precursor to supported metal catalysts by influencing the selectivity of the catalysts. In methane reactions with iridium-clusters, the rate is limited to the C-H bond dissociation on the iridium surface that remains uncovered during catalysis. The turnover rates are not dependant on the concentrations or identity of the co-reactants but rather the iridium dispersion [Wei, 2004, 43]. This is also true for Pt [Wei, 2004, 108, 4094], Ru [Wei, 2004, 108, 2253] and Rh [Wei, 2004, 225] clusters.

Industrial reforming makes use of metal catalysts to activate methane for producing liquid hydrocarbons (Fischer-Tropsch) and other products such as gasoline (MTG Process). Two such processes are the Steam Reforming Method (SRM) and the Partial Oxidation of Methane (POM). SRM is the most common method of producing commercial bulk hydrogen as well as the hydrogen used in the industrial synthesis of ammonia. At high temperatures (1200K) and in the presence of a metal-based catalyst (Al_2O_3), steam reacts with methane to form carbon monoxide and hydrogen.

$$CH_{4\,(g)} + H_2O_{\,(g)} \rightarrow CO_{\,(g)} + 3H_{2\,(g)}$$

Additional hydrogen can be recovered by a lower temperature gas-shift reaction with the carbon monoxide produced.

$$CO_{\,(g)} + H_2O_{\,(g)} \rightarrow CO_{2\,(g)} + H_{2\,(g)}$$

In the second part of the SRM process carbon monoxide and hydrogen react at a much lower temperature (520K) in the presence of a Cu/ZnO metal catalyst to form methanol.

$$CO_{\,(g)} + 2H_{2\,(g)} \leftrightarrow CH_3OH_{\,(l)}$$

The second industrial process which will be discussed is the POM process. Here methane oxidizes to form water and either carbon monoxide (low oxygen environment) or carbon dioxide (high oxygen environment).

$$CH_{4\,(g)} + 1.5\ O_{2\,(g)} \rightarrow CO_{(g)} + 2\ H_2O_{(g)}$$
$$CH_{4\,(g)} + 2\ O_{2\,(g)} \rightarrow CO_{2\,(g)} + 2\ H_2O_{(g)}$$

The process also takes place at high temperatures (1100˚C) in the presence of a metal-based catalyst (Pt) and it is faster than the SRM process. The carbon monoxide is extracted and then left to react with hydrogen at 520 to 570 K in the presence of a Cu/ZnO metal catalyst to form methanol.

$$CO_{(g)} + 2H_{2\,(g)} \leftrightarrow CH_3OH_{(l)}$$

Carbon monoxide can also react with hydrogen to form other hydrocarbons depending on the metal catalyst that is used as well as the ratio between the mole carbon monoxide and hydrogen used.

$$n\ CO_{(g)} + (2n+1)\ H_{2\,(g)} \rightarrow C_nH_{2n+2\,(g)} + n\ H_2O_{(l)}$$

This process is known as the Fischer-Tropsch process and its principal purpose is to produce a synthetic petroleum substitute, typically from coal or natural gas, for use as synthetic lubrication oil or as synthetic fuel. SASOL in South Africa uses coal and natural gas as a feedstock to produce such a variety of synthetic petroleum products [http://en.wikipedia.org/wiki/Fischer-Tropsch].

Other companies such as Shell have also commercialized their Fischer-Tropsch technology in order to produce low-sulphur diesel fuels and wax [http://en.wikipedia.org/wiki/Fischer-Tropsch].

Table 2.2 lists a summary of studies, other than those that have been discussed, that have been performed on catalytic reforming of methane.

Table 2.2 Summary of studies on catalytic reforming of methane

Reaction	Catalyst	Remarks	Reference
$CH_4 + CO_2 \rightarrow 2CO + 2H_2$	Cu/CdS-TiO_2/SiO_2	Photocatalyst	Shi, 2004
	Pt/ZrO_2	Also used for POM and SRM	Ross, 2005
	Mo_2C; WC	Carbon deposition on catalyst	Ross, 2005
	Mo_2C-Al_2O_3	Al_2O_3 support does not increase stability of catalyst	Ross, 2005
	Mo_2C-ZrO_2	ZrO_2 support dramatically increases stability of catalyst	Ross, 2005
	Mo_2C-SiO_2	SiO_2 support increase stability of catalyst	Ross, 2005
	Ni	Fischer-Tropsch reaction with carbon deposition on catalyst	Fischer, 1928
	Ni-Al-La	Al-La support decrease carbon deposition on catalyst	Mok, 1983; Gelsthorpe 1984
	Ir-AlO_2	Alumina support decrease carbon deposition on noble metals	Ashcroft, 1991
	Pt-AlO_2	Alumina support still have high carbon deposition	Ashcroft, 1991

	$Pt\text{-}TiO_2$	Titania support have improved activity of catalyst	Van Keulen, 1997
	Ga_2O_3	Photocatalyst	Yuliati, 2008
$2CH_4 \rightarrow C_2H_6 + H_2$	Ga_2O_3	Photocatalyst	Yuliati, 2008
	Silica-based	Photocatalyst	Yuliati, 2006, 961; Yuliati 2007; Kato 1998; Yoshida, 2002; Yuliati, 2005, 195
	Zeolites	Photocatalyst	Kato, 2002
	Mesoporous silica	Photocatalyst	Yuliati, 2006, 214
	Ceria-based	Photocatalyst	Yuliati, 2005, 4824

These studies on the dry reforming of methane proved that by adding a support to the catalyst, the carbon deposition on the catalyst can be minimized to improve the stability of the catalyst. Some supports, e.g. the zirconia, improved the stability of the catalysts better than others (alumina), especially for the carbides and Pt. Photocatalysts showed better efficiency compared to the normal metal catalysts due to the improved activation of the catalyst under irradiation.

It's safe to say that the use of metal-based catalysts has made a great impact in the industry and a lot of research was done to improve these processes. However, breaking of the C-H bond still seem to be both the rate determining step during the reactions of CH_4 and the step that increases the cost due to the needed expensive catalysts.

2.2.2 Photoexcitation of methane

In the upper atmosphere, photodissociation by solar radiation represents a significant loss in CH_4 [Levine, 1985]. For methane, absorption only begins in the vacuum-ultraviolet region due to the absence of lone-pair electrons. Absorption occurs from about 145 nm to its maximum at 94 nm [Robin, 1974]. Hertzberg showed that below 77 nm all absorption results in photoionization, while above 94.6 nm absorption causes dissociation of the molecule [Hertzberg, 1966].

Photochemical studies by Mahan and Mandal suggest that CH_2 and H_2 are the major dissociation products after photoexcitation at 123.6 nm [Mahan, 1962].

The spin-allowed dissociation pathways of excitation at the Lyman-α (121.6 nm) wavelength are given below.

$$CH_4 + \hbar\omega_{L\alpha} \rightarrow H + CH_3,\ E_{kin} \leq 545.2\ \text{kJ/mol} \quad (1a)$$

$$CH_4 + \hbar\omega_{L\alpha} \rightarrow H_2 + CH_2,\ E_{kin} \leq 479.1\ \text{kJ/mol} \quad (1b)$$

$$CH_4 + \hbar\omega_{L\alpha} \rightarrow H + H + CH_2,\ E_{kin} \leq 43.1\ \text{kJ/mol} \quad (1c)$$

$$CH_4 + \hbar\omega_{L\alpha} \rightarrow H + H_2 + CH,\ E_{kin} \leq 94.9\ \text{kJ/mol} \quad (1d)$$

where E_{kin} is the kinetic energy of the system. The amount of energy needed for the different reaction paths was calculated using the enthalpies of formation at 298 K [Atkinson, 1992].

Brownsword and co-workers investigated the dissociation of methane at the Lyman-α wavelength and found that the two-body dissociation reaction paths (1a and 1b) dominate the primary methane photochemistry in the Lyman-α wavelength region while the three-body paths (1c and 1d) play a less important role [Brownsword, 1997]. Earlier studies by Zare, Chandler and co-workers [Heck, 1996] revealed that after Lyman-α excitation, C-H bond dissociation via reaction (1a) was an important primary dissociation process. This corresponds with predictions made by Karplus and Bersohn [Karplus, 1969].

The optical absorption cross section of methane at the Lyman-α wavelength, was found to be $2.0 \pm 0.1 \times 10^{-17}$ cm^2 at room temperature [Brownsword, 1997]. This is important to determine the H atom quantum yield with the following equation:

$$\Phi_H = \{S_H(CH_4)\, \varphi_H(H_2O)\, \sigma_{H2O}\rho_{H2O}\}/\{S_H(H_2O)\, \sigma_{CH4}\rho_{CH4}\}$$

Brownsword and co-workers [Brownsword, 1997] determined the absolute quantum yield for H formation, $\Phi_H = 0.47 \pm 0.11$, by means of a photolytic calibration method where the Lyman-α photolysis of H_2O was used as a reference source of well-defined H atom concentrations.

Chapter 3

Computational chemistry methods

3.1 Introduction and history

Molecular modelling followed from theoretical chemistry that originated from the original tetrahedral carbon model of Le Bel and Van't Hoff [Van't Hoff, 1875; Le Bel, 1874]. This approximation, together with the development of quantum mechanical theories in the start of the 20th century, helped to qualitatively explain the bonds in organic chemistry [Pauling, 1940]. Theories that made a great impact in organic chemistry were that of de Broglie (1924 – wave particle duality), Schrödinger (1926) and the Hartree-Fock equations (1930) [Accelrys Inc., Quantum Chemistry, from Schrodinger to QCPE and on; www.mathhub.com/history/quantum.html]. Many reasons can be given for the slow development during and after this time period, however the main problem was the inability to test the theories [Accelrys Inc., A Short History of Early Computing, www.mathub.com/history/compchem.html].

Theoretical chemistry calculations had developed further and the Hückel-method was used for π-bonding calculations in the 1930's which later became the precursor to computational chemistry [Van Leeuwen, 1995]. The expanded Hückel calculation was developed in the 1950's to also incorporate σ-bonds. From this, discussions of electronic structure and chemical reactivity of organic molecules followed, with the Woodward-Hoffmann rules and concepts like "forbidden" and "allowed" transitions. Matrix versions of the Hartree-Fock equations were published in 1951 by Roothan and in 1957 Hartree introduced the self consistent field method (SCF). Quantitative calculations were made possible by the invention of the computer and improvements thereof as shown in table 3.1 [Accelrys Inc., Quantum Chemistry, from Schrodinger to QCPE and on; www.mathhub.com/history/quantum.html].

Table 3.1 The origin of the different quantum-codes

Code	Year	Developers
EXTHUC	1960's	Roald Hoffmann
DFT	1964	Hohenberg
GAUSSIAN 70	1970	WJ Hehre *et al.*
GAMESS	1977-1981	National Resources for Computations in Chemistry

In the decade between 1970 and 1980 three types of calculation possibilities made their appearance almost simultaneously, namely Ab Initio, Semi-Empirical and Forcefield calculations. The respective approximations have their individual

successes thanks to the respective research groups that developed it [Van Leeuwen, 1995].

3.2 Development of models

The purpose of a model is to make informed predictions by means of observed and measured properties of a similar known system. The following flow diagram in Fig. 3.1 shows the route to follow when a model is to be created [Cornils, 1996].

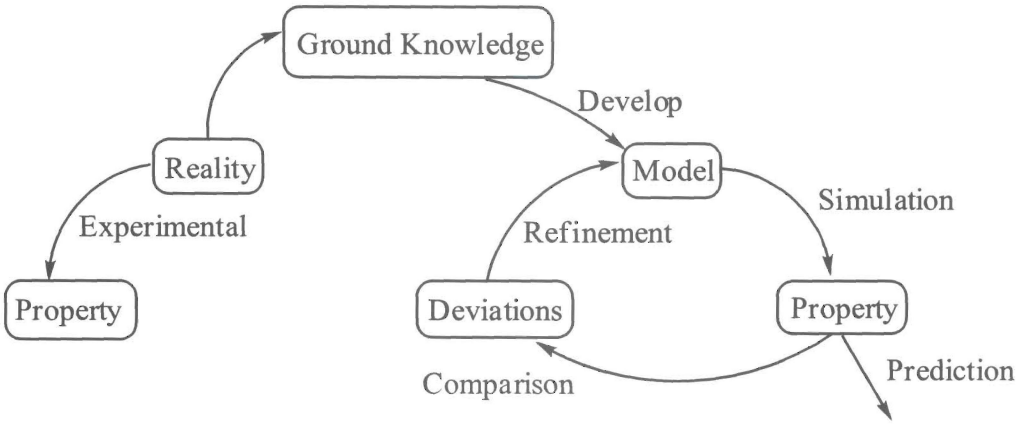

Figure 3.1 Presentation of a model [Cornils, 1996].

Because a model is only a representation of the reality, it can only describe some of the properties. In a good or ideal model, only the properties that are necessary for the specific study are given. This must be kept in mind when using the model in a different situation so that no incorrect assumptions are made. A good model is thus a reliable version of an object in a given situation. The model must first be tested to see whether it satisfies all the requirements. For this, experimental data can be used and any deviations can be investigated. The model is then rejected or accepted after the needed changes have been made. If the model gives acceptable results it can be used to calculate non-observable properties or it can be used to make predictions on similar systems where the data is unknown or immeasurable.

3.3 Molecular mechanics

3.3.1 Basic theory

Small objects such as atoms and molecules do not follow the laws that are described by the classical laws of Newton. Quantum mechanical descriptions as presented by Schrödinger, Bohr, Heisenberg and de Broglie must be used to obtain a better (more suiting) description of the model. It is however, mathematically impossible to solve Schrödinger-equations that describe the spatial distribution of electrons and nuclei in molecules. Non-quantum mechanical strategies like mathematical equations derived from classical mechanics and electrostatic laws are then used. In these equations empirical parameters (constants) are used to give the best correlation with experimental data [Jensen, 1999].

The molecular mechanics energy expression consists of a simple algebraic equation for the energy of a compound. It does not use a wavefunction or total electron density. The constants in this equation are obtained from spectroscopic data. A set of equations with their associated constants is called a force field [Clark, 1985]. The assumption of the molecular mechanics method is the transferability of the parameters. This means, for example, that the energy associated with a particular molecular motion, say the stretching of a carbon–carbon single bond, will be the same from one molecule to the next. This gives a very simple calculation that can be applied to very large molecular systems.

In order for the transferability of parameters to be a good description of the molecule, force fields use atom types [Clark, 1985]. This means that a sp^3 carbon will be described by different parameters than a sp^2 carbon, and so on.

The energy expression consists of the sum of simple classical equations [Grant, 1995]. These equations describe various aspects of the molecule, such as bond stretching, bond bending, torsions, electrostatic interactions, van der Waals forces, and hydrogen bonding. Electrons are not explicitly included; therefore electronic processes cannot be modelled. Table 3.2 gives the mathematical forms of energy terms often used in force fields.

Table 3.2 Common Force Field Terms

Name	Use	Energy Term
Harmonic	Bond stretch	$k(l - l_0)^2$
Harmonic	Angle bend	$k(\theta - \theta_0)^2$
Cosine	Torsion	$k[1 + \cos(n\theta)]$

l-bond length
θ-bond angle

The energy computed by molecular mechanics is meant to be an energy that will reliably predict the difference in energy from one conformation to the next and includes the effect of strained bond lengths or angles. This is not the same as the total energies obtained from ab initio or the heat of formation from semi-empirical models [Grant, 1995]. Molecular mechanics methods are therefore not generally applicable to structures very far from equilibrium, such as transition structures. These calculations use an energy expression fitted to an ab initio potential energy surface for the specific reaction, rather than using the same parameters for every molecule [Grant, 1995].

3.3.2 Force field models

The following are some commonly used molecular mechanics force field models with a short description of their uses. A number of these have been implemented in more than one software package.

- **AMBER**

Assisted model building with energy refinement (AMBER) is a force field model that was specifically parameterized for proteins and nucleic acids [Roterman, 1989].

- **MMFF**

The Merck molecular force field (MMFF) model is a general-purpose method, particularly popular for organic molecules. Although it was originally intended for molecular dynamics simulations it has been used for geometry optimization [Corness, 1996].

- **MOMEC**

MOMEC is a force field model for describing transition metal coordination compounds. It also works reasonably well for octahedrally coordinated compounds. The metal-ligand interactions consist of a bond-stretch term which is most often described by a harmonic oscillator equation [Corness, 1996].

3.4 Quantum mechanical models

3.4.1 Basic theory

The principle of quantum mechanics is that it mathematically describes the behaviour of electrons. In theory, it can predict any property of an individual atom or molecule. However, the quantum mechanical equations have only been solved exactly for one electron systems [House, 1998]. For this reason, methods have been developed to approximate the solution for multiple electron systems. These approximations will be discussed in section 3.4.2.

The difference between molecular mechanics and quantum mechanical models is that the Schrödinger equation (Equation 3.1) [Cornils, 1996] is approached differently. In quantum mechanical models the equation is solved more exact even though there are still simplifications [Van Leeuwen, 1995].

$$H\Psi = E\Psi \qquad (3.1)$$

In equation (3.1) H is the Hamiltonian operator, Ψ a wave function, and E the energy. An equation of this form is called an eigen equation. Ψ is called the eigenfunction and E the eigenvalue. The wavefunction Ψ is a function that describes the probability of electrons being in certain locations.

3.4.2 Ab initio approximations

The term *ab initio* is Latin for "from the beginning". These types of computations are derived directly from theoretical principles without the use of experimental data. The approximations made are usually mathematical approximations, such as

using a simpler function form for a function or finding an approximate solution to a differential equation [Jensen, 1999].

Ab initio calculations give very good qualitative results and can yield increasingly accurate quantitative results for smaller molecules. The advantage of ab initio methods is that they converge to the exact solution once all the approximations are made sufficiently small in magnitude [Jensen, 1999]. The disadvantage of ab initio methods is that they are time-consuming [Jensen, 1999].

The following are some approximations that form part of ab initio methods:

- **Born-Oppenheimer approximation**

This approximation makes the assumption that the atom nucleus moves so slow in comparison to the electrons that the movement of the nucleus does not have to be described quantum mechanically.

- **Hartree-Fock approximation**

The Hartree-Fock approximation is one of the best known ab initio methods [Cornils, 1996; Bray, 1996]. This approximation assumes that every electron moves independently from the movement of the other electrons in the potential field [Davidson, 1998]. The approximation makes a "guess" what the electron density because of the all electrons is, except for the one which the Schrödinger-equation is solved [Davidson, 1998]. Now the problem has simplified to a one electron system that can be solved. This procedure will then be iterated for all the electrons until a stationary phase has been obtained. This is called a self-consistent field (SCF) and is equal to the minimum energy of the system [http://xbeams.chem].

- **Møller-Plesset perturbation theory**

In Hartree-Fock models there is assumed that every electron moves independently of the other. This means that the electrons are on average closer together than they are supposed to be [Davidson, 1998]. Møller-Plesset models take a slightly

different approach. When one electron approaches the other, it will move away so that there is minimal repulsion. This is mathematically accomplished by placing electrons in non-filled high energy orbitals [Jensen, 1999]. This disruption of the Hamiltonian is written in a mathematical series form whereby a Møller-Plesset model of the second order is called a MP2 model. As the order increases, so does the accuracy as well as the computational time [Jensen, 1999].

3.5 Semi-Empirical methods

3.5.1 Basic theory

Semi-Empirical calculations are set up with the same general structure as Hartree-Fock calculations in that they have a Hamiltonian and a wave function. Hartree-Fock calculations account for all the electrons in the system, whereas semi-empirical calculations only use the valence electrons [Jensen, 1999]. In order to correct for the errors introduced by omitting the core electrons, the method is parameterized. Parameters to estimate the omitted values are obtained by fitting the results to experimental data or ab initio calculations [Jensen, 1999].

Semi-Empirical methods are generally good for predicting molecular geometry and energies. They can also be used for predicting vibrational modes and transition structures a lot faster that ab initio methods, but do so less reliably.

A simplified presentation of the computation complexity against the parameterization of the theoretic models is illustrated in Figure 3.2. The fewer parameters, the more computation complexity and vice versa.

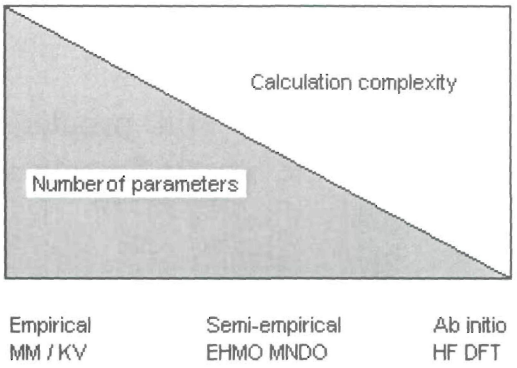

Figure 3.2 Computation complexity against parameterization of theoretical models [Cornils, 1996].

3.5.2 Various semi-empirical methods

- **Extended Hückel**

An extended Hückel calculation is a simple means for modelling the valence orbitals based on the orbital overlaps and experimental electron affinities and ionization potentials. Extended Hückel made a valuable contribution to the parameterization of the transition metals and is therefore a valuable method, because it is general enough to use for all the elements in the periodic table [Cornils, 1996]. This is primarily the reason why it is still used today.

- **MNDO**

The modified neglect of diatomic overlap (MNDO) method has been found to give reasonable qualitative results for many organic systems [Lewis, 1986].
A variation on MNDO is MNDO/d that is an equivalent formulation except that the method includes the d- orbitals. This method is sometimes used for modelling transition metal systems, but its accuracy is highly dependent on the individual system being studied [Lewis, 1986].

2.2AM1

The Austin Model 1 (AM1) method is still popular for modelling organic compounds. AM1 generally depicts the heat of formation (ΔH_f) more accurately than MNDO [Holder, 1998].

There are some improvements and limitations in the results obtained by this method, for example: the calculation of activation energies have been improved, while it is also known that rotational barriers have been predicted to be one-third of the actual barrier [Holder, 1998].

- **PM3**

Parameterization method 3 (PM3) uses nearly the same equations as the AM1 method along with an improved set of parameters. It is extremely popular for organic systems due to the availability of algorithms for including solvation effects in these calculations [Stewart, 1998].

Some of its advantages include that it is more accurate than AM1 for hydrogen bond angles and overall heats of formation. A disadvantage is that AM1 is more accurate for hydrogen bond energies [Stewart, 1998].

- **Gaussian theory**

The Gaussian methods (G1, G2 and G3) arose from the observation that certain ab initio methods tended to show an error for predicting the energies of the ground states of organic molecules [Curtiss, 1998]. This resulted in a correction equation that uses the energies from several different ab initio calculations to obtain a very accurate result. Although only ab initio calculations are used, the equation that combines the different calculations is an empirically defined equation that is parameterized to reproduce results from a test set of molecules as accurately as possible [Curtiss, 1998].

Since it is a semi-empirical method, it shows the same strengths and weaknesses as other semi-empirical methods. The accuracy can be extremely good for systems similar to those for which they are parameterized such as the ground state of organic molecules. For other systems, such as transition structures, these methods are less accurate than ab initio methods [Curtiss, 1998].

3.6 Density functional theory

3.6.1 Basic theory

In the Hartree-Fock model the energy of a molecule is calculated through the use of wavefunctions. From the theory of Hohenberg and Kohn [Jensen, 1999], the energy of the ground state of a system can also be calculated from the electron density. This is the premise behind density functional theory (DFT).

$$E(\rho) = E_{KE}(\rho) + E_C(\rho) + E_H(\rho) + E_{XC}(\rho)$$

where $E(\rho)$ is the total energy, $E_{KE}(\rho)$ is the kinetic energy, $E_C(\rho)$ is the electrostatic energy, $E_H(\rho)$ is the electron-electron Coulomb-energy and $E_{XC}(\rho)$ is the correlation- and exchange energy.

In this formulation, the electron density is expressed as a linear combination of basis functions similar in mathematical form to Hartree-Fock orbitals. A density functional is then used to obtain the energy for the electron density. A functional is a function of a function, in this case, the electron density. The exact electron density is not known. Therefore, there is a list of different functionals that may have advantages or disadvantages. Some of these were developed from fundamental quantum mechanics and some by parameterizing functions to best reproduce experimental results [Jensen, 1999]. Thus, DFT has ab initio and semi-empirical properties to it.

Mathematically, it is easier to calculate the energy through minimizing the electron density. DFT methods also make provision for exchange- and correlation energy [van Sittert, 2006]. This makes DFT methods more appropriate for energy

calculations where there is for example, bond breaking. It should however be noted that the choice of basis set influence the accuracy of the results [Jensen, 1999].

3.6.2 Common basis sets

The following is a short description of the basis sets that are commonly used for DFT calculations.

- **6-31G*, 6-31G** and 6-311G***

These basis sets are known as polarization basis sets and is denoted by a "*". In an unsymmetrical environment the electron distribution will be polarized and the centre of the electron distribution will no longer correspond to the centre of the nucleus. An unsymmetrical orbital is obtained when for example a p-orbital is combined with a d-orbital. Polarization basis sets can be obtained by adding polarization functions to split-valence basis sets [van Sittert, 2006].

Chapter 4

Background on photochemistry

4.1 The nature of light

Light is a form of energy or electromagnetic radiation of certain wavelengths and exhibits both wave-like and particle-like properties. This is known as wave-particle duality [http://en.wikipedia.org/wiki/Wave-particle_duality]. The wave-like properties arise from the transverse oscillation of electric and magnetic fields in planes perpendicular to each other and to the direction of propagation of the light (Fig.4.1). It is the wavelength or frequency of these oscillations that defines the characteristic colour of the light.

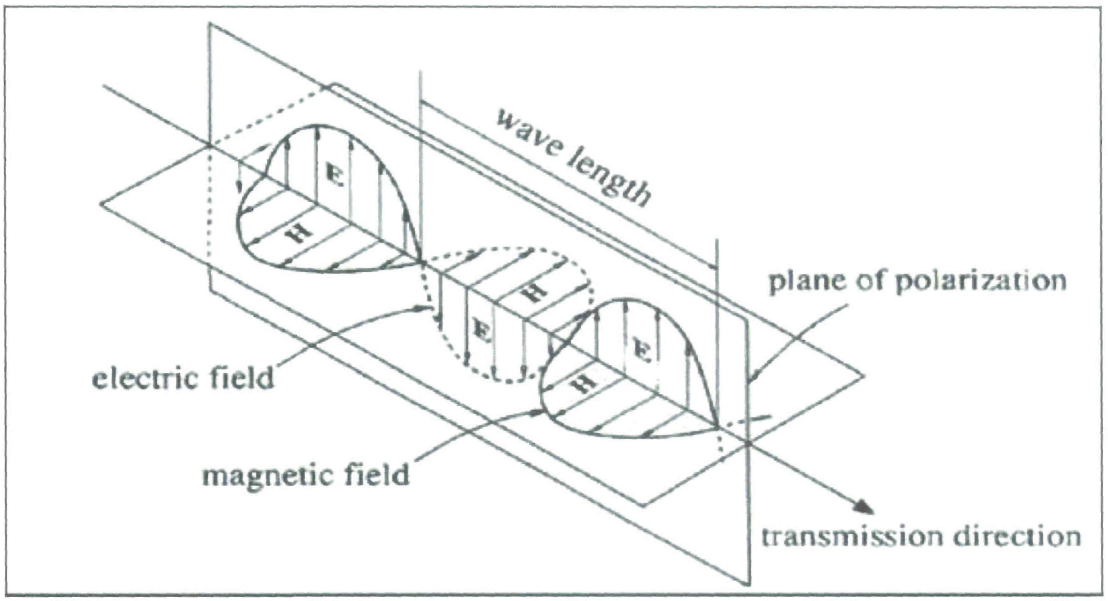

Figure 4.1 Oscillation of electric and magnetic fields in the propagation of light [http://www.mike-willis.com/Tutorial/PF_files/Picture12.jpg].

The particle-like properties arise from Einstein's work on the photoelectric effect. When light strikes a metal surface, electrons are ejected from the surface causing an electric current. The energy of these ejected electrons is proportional to the frequency of the light. This demonstrated that radiation also behaved as though it consists of a stream of particles called photons. Each of these photons has a fixed energy that depends on the frequency of radiation. This formed the basis for wave-particle duality and much of quantum mechanics.

4.2 Absorption and emission of radiation

For a species to be excited, it needs to absorb energy. This energy needs to be quantized since the energy levels in matter are quantized. This means that the species can only exist in certain defined, discrete energy states. Thus for each individual species only specific energies, and therefore frequencies of radiation can be absorbed or emitted.

A species possesses different forms of internal energy, each of which is quantized. These include rotational energy, vibrational energy and electronic energy. Vibrational energy arises from the oscillation of atoms in a molecule while electronic energy depends on the distance of the electron from the nucleus and the type of orbital that it occupies.

When a species absorbs a quantum of radiation it is dependent on the wavelength of the radiation on how the species will assimilate the energy. The longer the wavelength of the electromagnetic radiation is, the lower the photon energy. Absorption in the infrared (low energy) region leads to transitions between the vibrational states of species. If radiation in the visible to ultraviolet (high energy) region is absorbed, transitions between the electronic energy levels will occur which will lead to electronic excitation.

The energy required to produce an excited state is obtained by inspection of the absorption or emission spectrum of the molecule in question, together with the application of Eq. (1.1)

$$\Delta E = E_2 - E_1 = h\nu \qquad (1.1)$$

where h is Planck's constant, ν is the frequency at which absorption occurs, and E_1 and E_2 are the energies of a single molecule in the initial and final states.

The converse of absorption is emission which constitutes the transition from a higher energy state m to a lower energy state l. There are two types of emission namely, stimulated emission and spontaneous emission. Spontaneous emission is the process where an excited species undergoes a spontaneous decay (transition) to

a lower energy level and emits a photon. The loss of energy takes place in the absence of a radiation field as can be seen in figure 4.2.

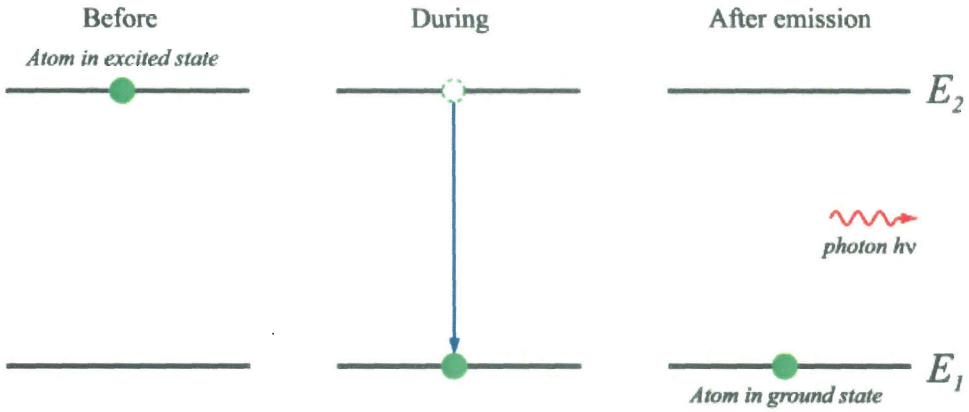

Figure 4.2 Spontaneous emission [http://content.answers.com/main/content/].

Stimulated emission is the process by which, when perturbed by a photon, matter may lose energy resulting in the creation of another photon (Fig 4.3). This means that the interaction between the excited species and the electromagnetic radiation causes the energy-rich species to give up its energy to the incident radiation. The perturbing photon is not destroyed in the process, and the second photon is created with the same phase, frequency, polarization, and direction of travel as the original.

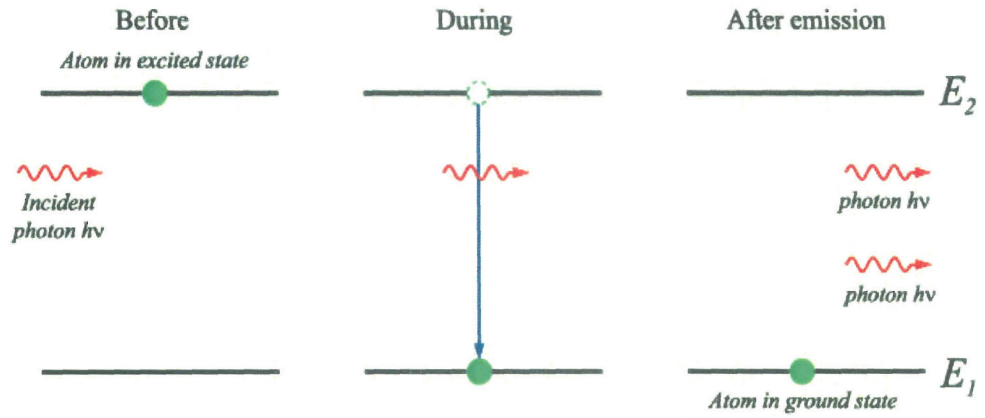

Figure 4.3 Stimulated emission
[http://physics.schooltool.nl/quantumoptics/images/].

Stimulated emission can be referred to as an amplification of the electromagnetic radiation and forms the basis of lasers.

4.3 Electronic excitation

When energy is absorbed by a species, the species becomes excited. This excited state has an altered reactivity from the ground state. This enables the species to undergo reactions that under normal conditions could not have taken place because of the new electronic arrangement.

The energies involved in electronic excitation are of the same magnitude as bond energies, which mean that the electronic excitation has an effect on the bonds in the species. The energies also correspond well with typical activation energies for reactions, and can aid a species to partially or completely overcome an activation barrier.

The energy of an excited species is not the only factor that affects its reactivity. On excitation, an electron is frequently promoted to a different type of orbital. This new orbital can have a different shape or symmetry than the previous orbital and can therefore fundamentally define the reactions the species can and cannot undergo. Thus this change in spatial distribution of electrons can have a major effect on reactivity. For example, if one of the electrons in the bonding π-molecular orbital of a C=C compound absorbs radiation in the UV-region, the electron can be promoted to the antibonding π*-molecular orbital, which will lead to a decrease in stability of the compound [http://www.cem.msu.edu].

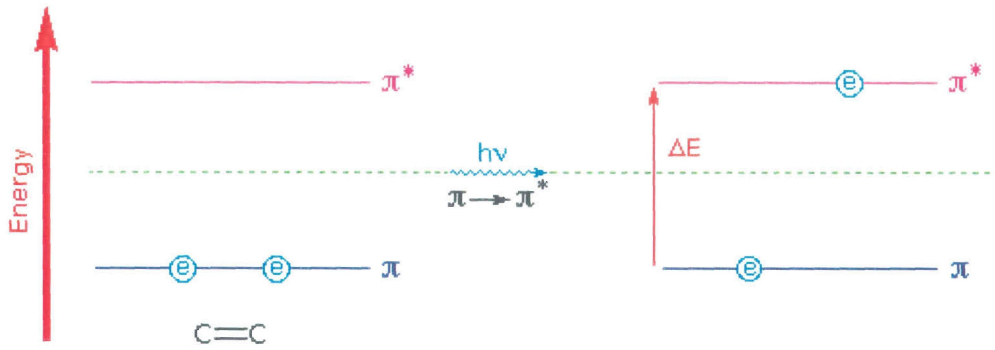

Figure 4.4 Example of π→π* excitation in a C=C compound [http://www.cem.msu.edu].

4.4 Wave mechanics and quantum numbers

Wave mechanics is a complex mathematical theory that gives rise to quantum numbers that define the electronic state of a species.

Electrons possess both spin angular momentum and orbital angular momentum. These momenta are vector quantities that are essential in determining the structure of atoms.

The spin moment of a single electron, s, is equal to ½ and the vector summation of spin moments of each individual electron in a species is the overall spin S and is extremely important in defining the electronic state of a species. It is common practice to specify a state by the spin multiplicity, $2S + 1$, rather than by the spin itself. This is because $2S + 1$ shows the maximum number of different states of the total angular momentum, J, for a given (L, S) combination (if $L>S$) [http://en.wikipedia.org/wiki/Term_symbol]. To demonstrate spin multiplicity for a species in which all the electrons are paired, $S = 0$, $2S + 1 = 1$ then the species is a singlet. If two electrons are unpaired with parallel spins, $S = 1$, $2S + 1 = 3$ then the species is in a triplet state. This is commonly the excited state of a species with a singlet ground state. For species such as free radicals that only have one unpaired electron it will have a doublet state since, $S = ½$ and $2S + 1 = 2$. Spin is of particular significance because, according to quantum mechanics, it cannot change

during an electronic transition [http://en.wikipedia.org/wiki/Selection_rule]. This can be rewritten as $\Delta S = 0$. This is a so-called selection rule and gives an indication of the feasibility of a transition from one state to another in terms of the quantum numbers [http://en.wikipedia.org/wiki/Selection_rule].

4.5 Fates of excited species

When a species absorbs radiation it will, depending on the wavelength of the radiation, become either electronically- or vibrationally- or rotationally excited and will therefore possess new properties that are different from that of the ground state species. A change in chemistry of the species will result in a change in reactivity. Figure 4.4 gives a representation of the most important routes that a species can undergo after electronic excitation has taken place. The figure shows a molecule AB that comprises of two individual atoms, A and B, which is electronically excited due to photon absorption.

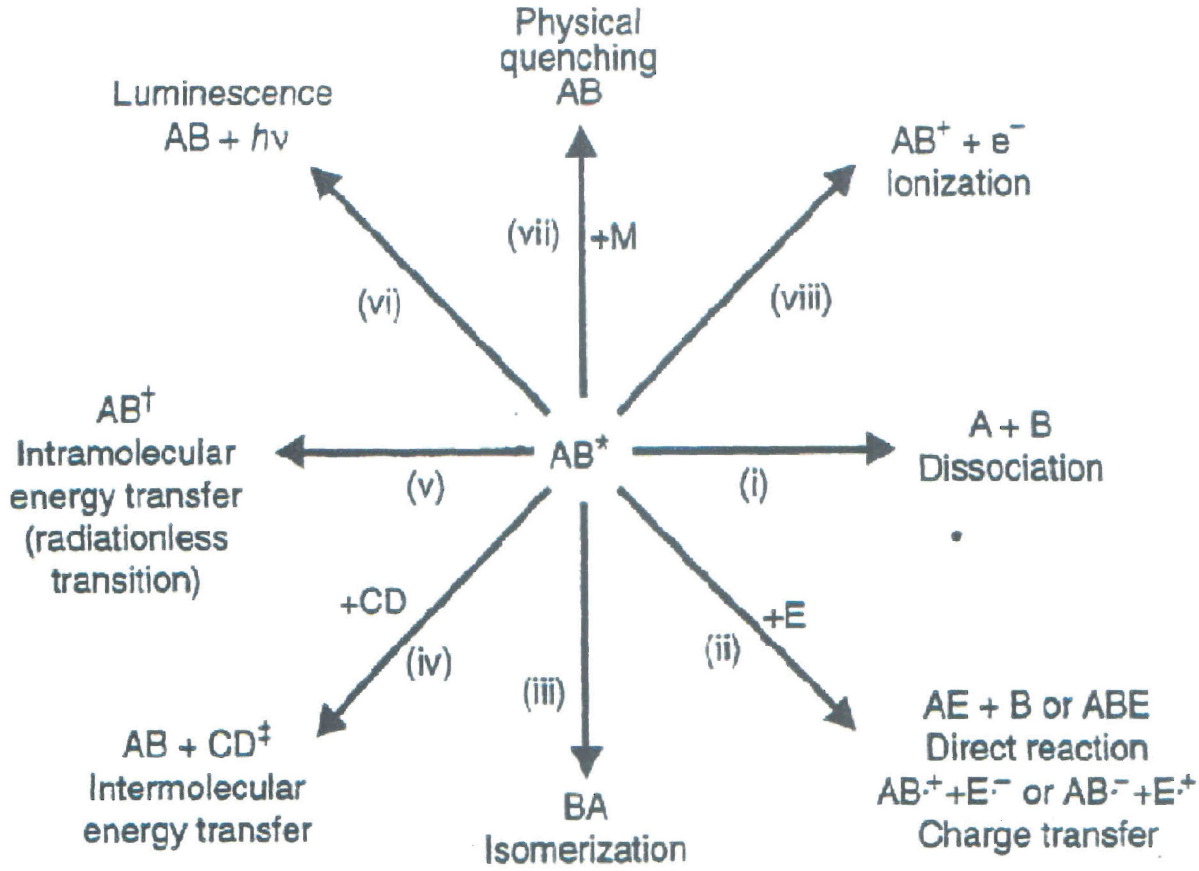

Figure 4.4 Routes to loss of electronic excitation [Wayne, 1996].

4.6 Multiphoton photochemistry

In multiphoton photochemistry, a single species or particle absorbs more than one photon. Such absorption only occurs at sufficiently high intensities, and it has taken the development of lasers to provide a suitable light source to study these reactions [Wayne, 1996].

In order to achieve multiphoton excitation, two mechanisms may be considered [Wayne, 1996]. The first of which is called, sequential excitation or otherwise known as resonant two-photon excitation, which involves the population of an intermediate state. The first photon populates that state which acts as the starting point for the absorption of the second photon. This can be illustrated by Figure 4.5(a). The second mechanism is known as non-resonant two-photon excitation,

which, as the name states, involves no resonant intermediate state (Figure 4.5(b)). Rather, a virtual state is created by the first photon's interaction with the ground state. Only if the second photon arrives within the duration of the first interaction, can it be absorbed. This process is therefore often referred to as simultaneous biphotonic absorption.

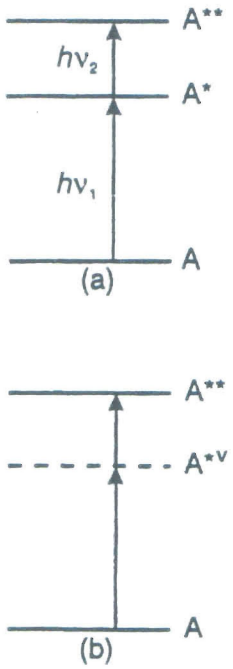

Figure 4.5(a) Resonant and (b) non-resonant two-photon absorption [Wayne, 1996].

The reason for the high intensities needed to achieve two-photon excitation, now becomes apparent. In the resonant process, it is necessary that the second excitation step occurs before loss processes, such as intramolecular relaxation or emission, depopulate the intermediate state, while with the non-resonant process the two photons must reach the absorber simultaneously.

The advantage of multiphoton excitation is that excited states that are normally not accessible can be populated. This means for example, through using multiphoton excitation, one can avoid conducting high-energy vacuum ultraviolet-experiments, requiring wavelengths shorter than 190 nm, by just working in the normal ultraviolet region.

4.7 Lasers

The acronym laser stands for Light Amplification by Stimulated Emission of Radiation. As the name suggests, the operation of a laser depends upon the net production of stimulated emission (the difference between stimulated emission and absorption). Stimulated emission is the opposite of absorption and both take place in systems in which transitions between the electronic levels occur. The basis of light amplification lies in a situation described as population inversion [Wayne, 1996].

In order to achieve population inversion, needed for laser action, various approaches may be adopted. In a two level system, a population inversion is difficult to achieve due to the fact that there are no energy levels that can act as reservoirs. Only if additional levels are available can there be an accumulation of population that will lead to population inversion. For a three-level system, it is required that the decay rate from level 3 into level 2 must dominate over the decay rate from level 3 to level 1 (ground state). The spontaneous decay rate from level 2 to level 1 must also be low. This causes a parameter $\beta = A_{32}/A_{21}$, where β is the Einstein coefficient and A_{32} and A_{21} is respectively, the decay rate from level 3 to level 2 and decay rate from level 2 to level 1, to be as large as possible. This parameter β will determine how efficient the generation of laser action will be for the specific system. These processes are illustrated by figure 4.6.

Four level laser systems are potentially more efficient laser systems than three level systems. This is because population inversion occurs as soon as the third level is populated (Figure 4.6(c)). Nd:YAG, dye and gas-phase lasers are common four level laser systems. Dye lasers are a bit different than the other four level systems and this is because there are only two electronic levels involved. The other two levels that are used come from the vibrational sub-levels. Dye lasers are very useful since they are tuneable as a result of using systems that exhibit broad-band absorption and emission characteristics from which the desired frequency may be selected through using a diffraction grating.

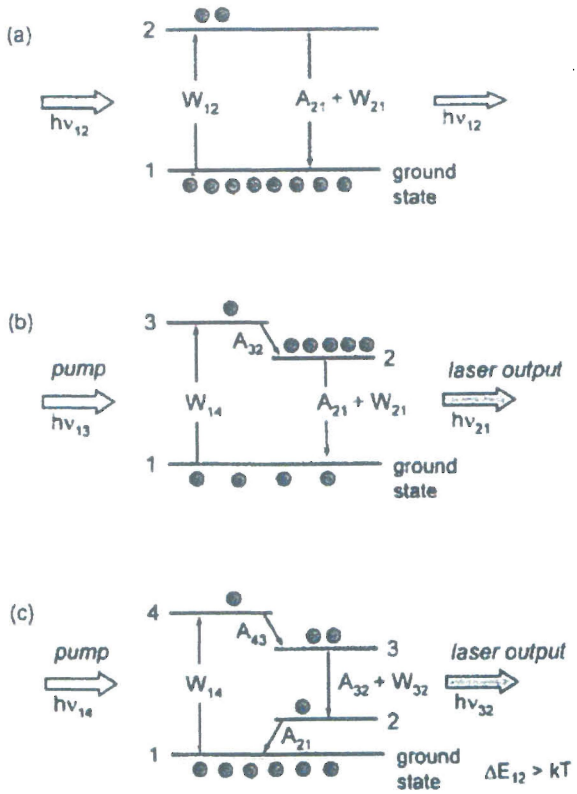

Figure 4.6 Illustration of the population in a (a) two-level (b) three-level and (c) four-level system for the absorption and emission processes [Telle, 2007].

Gas-phase lasers such as CO_2 and nitrogen lasers, often use an electrical discharge to excite the gas which leads to a population inversion. The excitation is due to the collisions between the species and the high energy electrons from the discharge.

Laser radiation has a variety of applications due to the special properties that the emitted light possesses. Some of the uses include laser welding, reading CDs, microsurgery, military weapon guidance and research (photochemistry). Lasers can provide the desired light source for highly selective excitation of specific energy levels and in conjunction with modern techniques be used for probing the excited states. This can be a useful tool to investigate intermediate species or fragments produced in photochemical reactions. Some of these techniques form part of a newly developed field in chemistry called femtochemistry, which is the science that studies reactions on extremely short timescales.

4.8 Femtochemistry

4.8.1 Introduction

In the late 1980's, A.H. Zewail performed a series of experiments that led to the development of a research area called femtochemistry [Zewail, 1988]. This involved the use of a high speed "camera" to capture and map the movements of molecules as they react and orient themselves in reactions. The "camera" was based upon a pump-probe technique in which the reactants were activated or pumped by a laser light pulse, closely followed (few femtoseconds) by a second laser pulse (probe), that captured the effects of the excitation of the first laser pulse. While the time scale needed for a vibration between two molecules to complete (approximately 10-100 fs) was in the same order as the pump-probe, it meant that it could be possible to observe in real-time the intermediates formed during a reaction. It actually became possible to observe how atoms rearrange themselves within molecules to form new molecules. Through a better understanding of these molecular dynamics, one may be able to control chemical reactions.

The name femtochemistry is taken from the term femtosecond, which is 10^{-15} seconds. This means that a femtosecond is a millionth of a billionth of a second. In Layman's terms, a femtosecond is to a second as a second is to 32 million years. In order to study molecular motion (~ 1 km/s) over a distance of 1 Å requires 100 fs. This act forms the focus area of femtochemistry.

Molecules can undergo different reactions which depend mainly under what conditions the system is in. Photochemical reactions are influenced by the frequency or wavelength of the radiating light and can therefore lead to different photochemical pathways. However there is another factor which is known as the potential energy surface (PES) (Figure 4.7) of a molecule that limits our ability to control reactions through changing the frequency of the radiation [Telle, 2007]. In order to obtain a better control over the photochemical pathways, it is necessary to be able to manipulate the wave-packet dynamics on the PESs of the excited molecules. This powerful method of control is called coherent control.

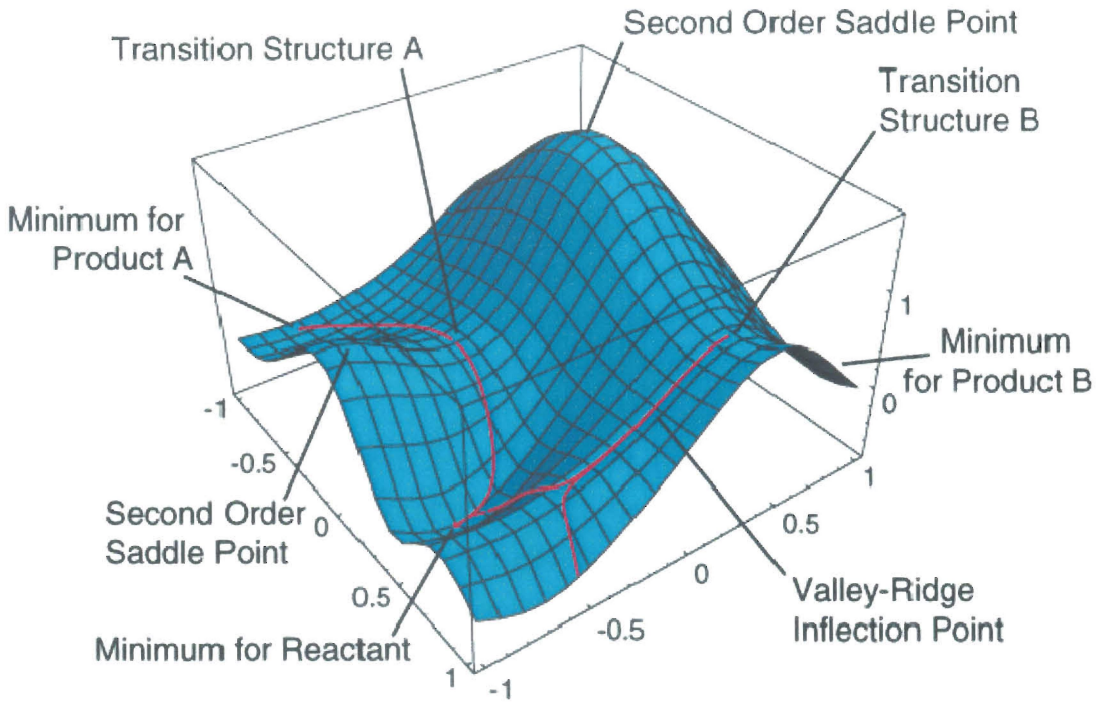

Figure 4.7 Potential energy surface
[http://www.chem.wayne.edu/~hbs/chm6440/PES.gif].

4.8.2 Coherent Control

Coherent control can experimentally be achieved by altering the pulse shape, duration, phase or polarization or even by using a sequence of pulses [Telle, 2007]. For a reaction with multiple reaction paths/outcomes, the optimum yield of a desired product can be tailored by changing both the pulse shape and the sequence of frequencies. An adaptive learning algorithm is used to control and manage these changes. The algorithm can thus be seen as a software tool that computes the next step towards producing the optimum amount of a specific product and then tailors the laser pulse in the appropriate way. This procedure is also called adaptive closed-loop control [Telle, 2007]. This is performed by first specifying the product to be optimized, then with the use of a suitable detector, feed information back into the computer, which then compares the actual product yield with the desired, after each laser pulse.

The details of the sequence of events for adaptive closed-loop control are as follows:

1. The information on the product to be optimized is stored in the computer.
2. The target molecule is pumped (excited) by the laser pulse after which the excited species is then probed or measured. The detector sends the output data to the computer where it is compared to the user defined objectives.
3. The computer software then sends a signal to the pulse shaper in order to modify the laser pulse.
4. The results of the altered laser pulse is then compared to the results of the previous pulse and if there is an improvement in the yield of the desired product, then further similar change to the pulse is made. If the yield goes down, a change in the opposite sense is made.
5. The loop is repeated until the yield for the desired product is optimized.
6. For future use, the computer then stores the details of the optimum pulse.

Figure 4.8 shows a diagram of the adaptive closed-loop control. It should be noted that collisions or spontaneous emission do not interfere with the process that is being coherently controlled due to their longer time-scale at which they occur.

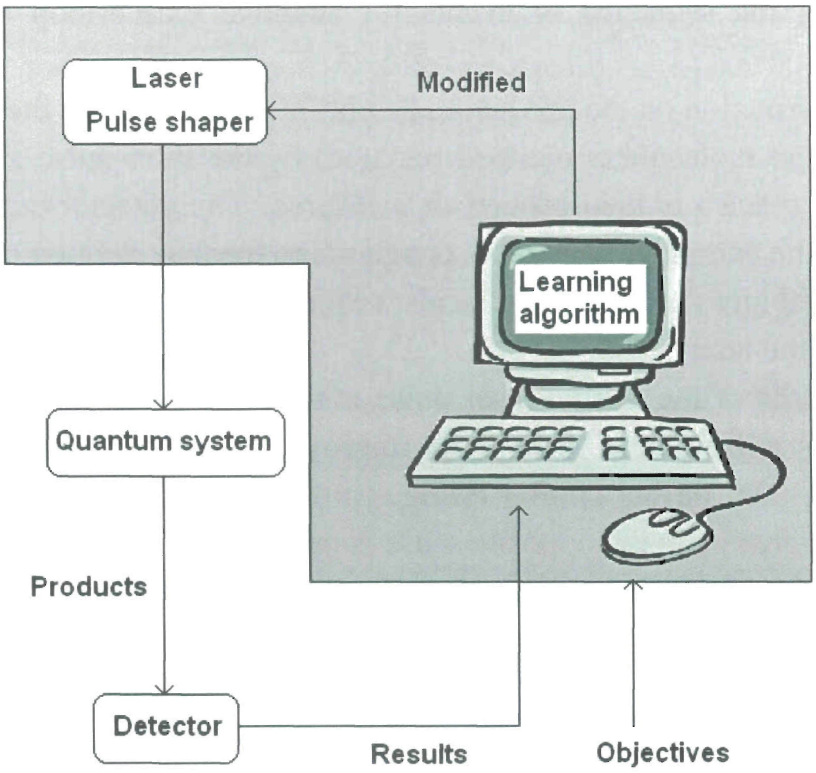

Figure 4.8 Closed-loop learning control.

4.8.3 Mode-locking

Mode-locking is a technique that is used to generate ultra-short laser pulses with high peak intensities [Telle, 2007]. However it seems contradictory that it is possible to generate these ultra-short pulses due to the frequency selection imposed by the laser cavity. This is because the emitted radiation originating from the laser cavity only allows oscillation in a few discrete resonance frequencies or modes that is defined by the cavity length [Rulliere, 2003]. These frequencies or modes are separated by $v_q = qc/2L$ where c is the speed of light and L the cavity length and q an integer.

Under normal conditions, a laser oscillates over all the resonance frequencies of the cavity for which the unsaturated gain is greater than the cavity loss, and then forms a set of longitudinal modes. The number of the longitudinal modes that can oscillate in the cavity is limited by the bandwidth over which optical gain is

provided [Rulliere, 2003]. So, in order to generate short pulses, these modes must be locked in phase. Figure 4.9 shows that the longitudinal modes keep going back and forth inside the cavity. This is because only a part of its energy is transmitted into the output beam, while the rest of the energy is reflected every time the packet is reflected off the output mirror [Rulliere, 2003].

There are two main mode-locking techniques called active mode-locking and passive mode-locking. In active mode-locking the radiation in the cavity is modulated at a rate which is matched to the cavity round-trip time. In passive mode-locking the laser radiation itself generates a modulation by a non-linear process [Rulliere, 2003]. An example of such a passive (or self) mode-locking, can be traced back to the early 90's when Scottish scientists accidentally bumped against the table on which the laser was mounted and noticed that the laser went into a pulse regime [Keller, 1991]. This is called an optical Kerr lens effect and shows that somehow a pulsed regime must be favoured over a continuous regime. This effect can be seen as a simple method to introduce non-linear absorption.

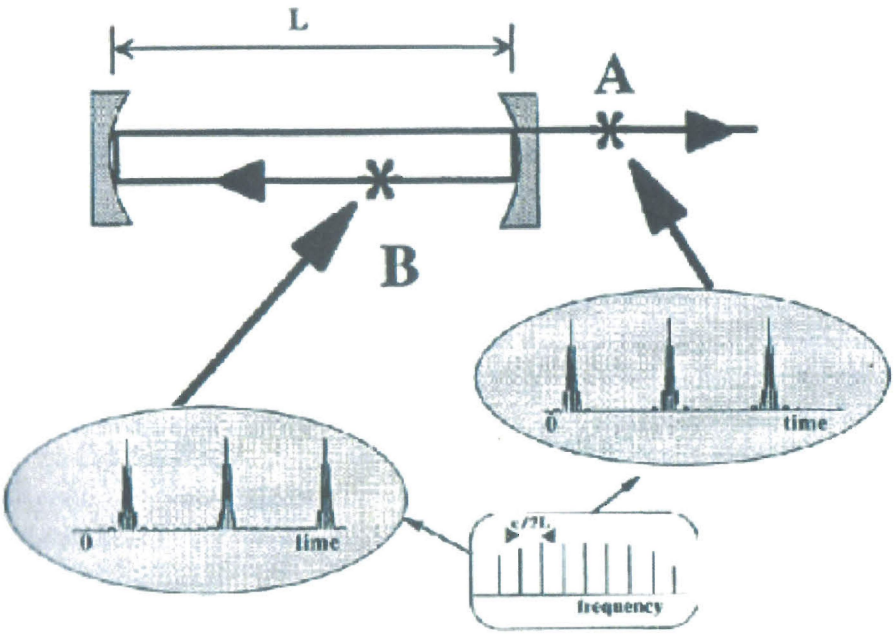

Figure 4.9 Illustration of pulse building up in a linear cavity [Rulliere, 2003].

Because the refractive index of a laser medium depends on the intensity of the light, it can cause a cylindrical laser crystal with plane front ends to act as a lens

for a TEM_{00} laser mode. This is because the intense centre of the mode propagates with a different speed as the weak wings of the laser mode (figure 4.10). As a result, the energy within a given resonator, which is determined by the pump energy, is more pronounced for the high intracavity intensity of pulsed operation than for the low intensity constant wave (cw) operation. By mounting a simple mechanical aperture at an appropriate position within the resonator, large losses for the cw mode and low losses for the focussed pulsed operation can be introduced (figure 4.10), resulting in the development of a situation where in only one short laser pulse will propagate back and forth in the resonator. To ensure that a net dispersion of the spectrally broad laser pulse is achieved, a combination of prisms can be used (figure 4.11). This technique is used in Kerr-lens modelocked Ti:Sapphire lasers that can produce pulse durations down to 10 fs.

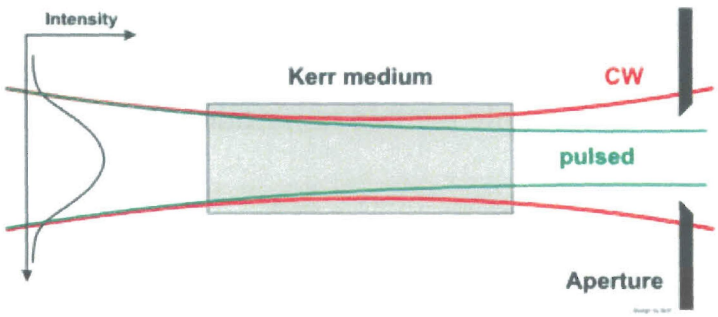

Figure 4.10 Kerr lens effect through nonlinear refractive index of a laser medium [http://upload.wikimedia.org/wikipedia].

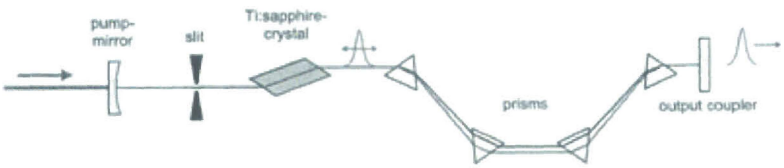

Figure 4.11 Kerr-lens modelocked oscillator with prism sequence to compensate for dispersion within the cavity.

4.8.4 Pump-probe technique

This is a simple yet very important technique for ultra-short laser pulse experiments. The technique uses at least two ultra-short light pulses to do an

analysis. The first pulse, also called the pump, is a high energy pulse that is used to excite a species into a higher energy state (electronic or vibrational) and notes the start of the experiment at t = 0. The second pulse, or the probe, is a lower energy pulse that is used to analyze or record the changes in the species due to the pump pulse [Rulliere, 2003]. The probe is delayed by a time $\Delta t = 2\Delta L/c$ where ΔL is the delay length of the beam pathway, and c is the speed of light. The probe can also be used to "further" excite an excited species and has significant experimental value due to the short time delay between the consecutive pulses. The advantage of this is that it makes it possible to excite a specific electronic- or vibrational state without the disadvantage of internal energy distribution or relaxation [Rulliere, 2003].

Some characteristics of the probe are that the probe can have a broad spectrum or it can be quasi-monochromatic. To generate pulses that have a narrow spectral range, dye lasers or optical parametric oscillators (OPO's) are used [Rulliere, 2003]. It is however important that the wavelength at which the species absorbs should fall in the wavelength domain of the pulse, otherwise the species will not absorb the transmitted pulse. If the spectral domain of the species is not known then it is best to use a pulse with a broad spectrum. This can be done by using a continuum or by broadband laser emission [Rulliere, 2003].

The first can be generated by focusing a high-peak-power light pulse through a medium such as H_2O or quartz glass. The second is to generate amplified spontaneous emission (ASE) in a dye laser system [Rulliere, 2003]. This technique however gives a less broad spectrum than the continuum but usually has a higher intensity.

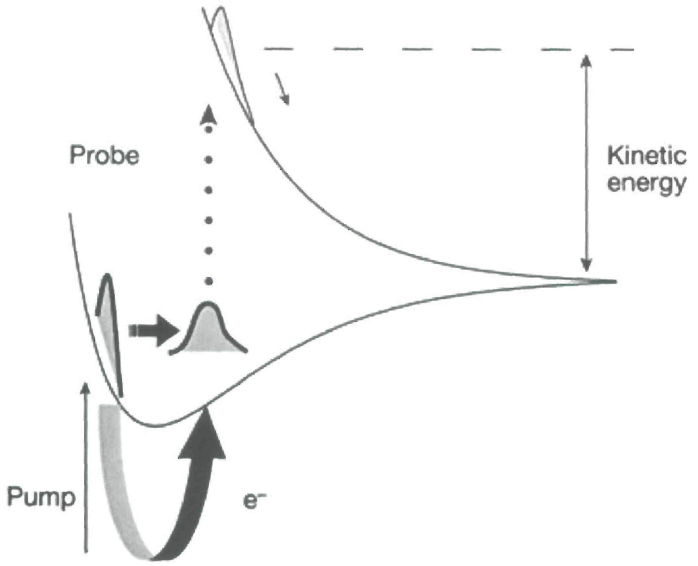

Figure 4.12 Illustration of a general PES activated by pump-probe [http://www.nature.comnaturejournalv421n6925imagesnature01430-f1.2.jpg].

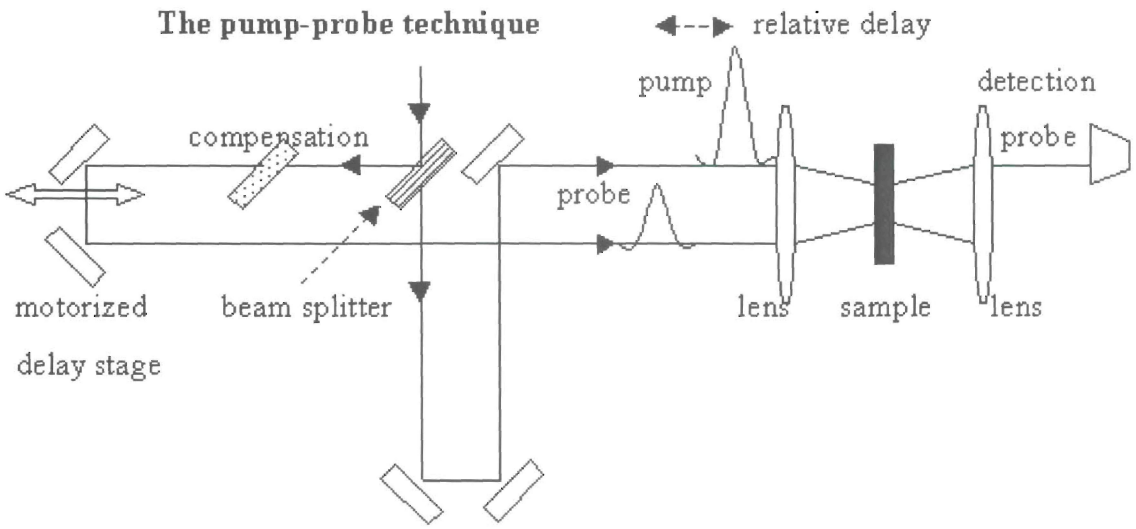

Figure 4.13 Typical scheme of a pump-probe experiment [http://www.mrnuke.com/wsupics/work/pump-probe.jpg].

The pump-probe technique is a very powerful tool and can be used in many different applications.

Part 3

Experimental

Chapter 5

Experimental methods and procedures

5.1 Molecular modelling

5.1.1 Hardware

Two types of hardware were used for the molecular modelling: a desktop personal computer with one central processing unit (CPU) and a dual core desktop personal computer with two CPUs. The dual core personal computer was also used for processing of the data. The dual core personal computer had the following specifications:

Operating system : Microsoft Windows© XP Professional Service Pack 2
Processor : Intel (R) Core™ 2 CPU 6400 @ 2.13 GHz
Memory : 2 GB

The single CPU computer had the following specifications:

Operating system : Microsoft Windows© XP Professional Service Pack 2
Processor : Intel (R) Pentium™ 4 CPU 3.4 @ 3.40 GHz
Memory : 2 GB

5.1.2 Software

The software packages used for the molecular modelling calculations were Wavefunction Inc. Spartan'06 Version 1.1.1 [http://www.wavefun.com] and Accelrys Materials Studio® 4.3.4 [Delley, 1990, 1996, 2000; http://www.accelrys.com]. For each calculation performed with Spartan the molecule was first geometrically optimized with the Molecular Mechanics method and MMFF basis set. Thereafter energy- and other quantum calculations were done using a number of methods and basis sets. These methods and basis sets were chosen to give as accurate results as possible with regard to the particular molecules. These methods and basis sets for Spartan are summarized in table 5.1.

Table 5.1 Summary of the methods and basis sets used for the Spartan calculations

Mathematical approach	Method	Basis set				
		STO-3G	3-21G	6-31G*	AM1	MP3
DFT	B3LYP			•		
Moller Plesset	MP2			•		
Hartree-Fock	RHF	•	•	•		
Semi-Empirical	RHF				•	•

The calculation parameters for Materials Studio's DMol^3 calculations are summarized in table 5.2. These parameters where used for all the DMol^3 calculations.

Table 5.2 Materials Studio Setup

DMol^3

	Parameter	Set Value
Setup:		
	Task	Geometry Optimization
	Quality	Medium
	Functional	LDA
	Use Symmetry	Selected
	Charge	0
Electronic:		
	Integration Accuracy	Medium
	SCF Tolerance	Medium
	Core Treatment	All electron
	Basis Set	DND
	Orbital cutoff quality	Medium
Properties:		
	Frequency	Selected
	Orbitals	Selected

5.2 Excitation reactions

This section will give the details of all the reagents and equipment used in the concerned excitation reactions. This will also include the details of preliminary calculations needed for the setup of the laser systems.

The excitation reactions that will be studied with their respective excitation wavelengths can be seen in table 5.3.

Table 5.3 Summary of the signal and idler wavelengths for the studied reactions

Reaction	Signal (nm)	Idler (nm)	Overtone Excited
$CH_4^* + CH_4^*$	450	1600	$2\nu_3$
$CH_4^* + CO_2$	450	1600	$2\nu_3$

* excited molecule

The first reaction studied was the conversion of methane into ethane, in which the gas cell was filled with methane and irradiated at 1.6 μm for the chosen time duration. The second reaction was the dry reforming of methane, in which a methane and carbon dioxide mixture was similarly excited. The reactions were categorized into two different sections. The first section comprised the use of a neodymium-doped yttrium aluminium garnet (Nd:YAG) nanosecond laser system and the second the use of a titanium sapphire (Ti:Sapphire) femtosecond laser system.

5.2.1 Reagents

Gas: Methane (99.5 – 100%)
Supplier: Afrox
Impurities: Nitrogen <= 3000 ppm
Oxygen <= 100 ppm
Ethane <= 2000 ppm
Ethylene <= 100 ppm
Other hydrocarbons <= 500 ppm

Carbon dioxide <= 100 ppm
Gas Mixture: Carbon dioxide and methane
Supplier: Afrox
Mixture ratio: 1/1 CH_4/CO_2 (50% mixture)
Impurities: None

5.2.2 Nanosecond excitation reactions

5.2.2.1 Equipment

Name: Neodymium-doped yttrium aluminium garnet (Nd:YAG) laser
Brand: Continuum
Model: Powerlite 9010
Information and Specifications: Table 5.4 gives the properties of a Nd:YAG laser and table 5.5 gives the specifications of the Continuum Powerlite 9010.

Table 5.4 Properties of Nd:YAG = neodymium-doped yttrium aluminium garnet [Geusic, 1964].

Property	Value
Chemical formula	$Nd^{3+}:Y_3Al_5O_{12}$
Crystal structure	cubic
Mass density	4.56 g/cm^3
Moh hardness	8–8.5
Young's modulus	280 GPa
Tensile strength	200 MPa
Melting point	1970 °C
Thermal conductivity	10–14 W/(mK)
Thermal expansion coefficient	7–8 × 10^{-6}/K
Thermal shock resistance parameter	790 W/m
Birefringence	none (only thermally induced)
Refractive index at 1064 nm	1.82
Temperature dependence of refractive index	7–10 × 10^{-6}/K
Nd density for 1 at. % doping	1.36 × 10^{20} cm^{-3}
Fluorescence lifetime	230 µs
Absorption cross section at 808 nm	7.7 × 10^{-20} cm^2

Emission cross section at 1064 nm	28×10^{-20} cm^2
Gain bandwidth	0.6 nm

The most common Nd:YAG emission wavelength is 1064 nm. Starting with that wavelength, outputs at 532, 355 and 266 nm can be generated by frequency doubling, -tripling and -quadrupling, respectively. The output wavelength used for the Nd:YAG laser in this study is the frequency tripled 355 nm.

Table 5.5 Specifications of the Continuum Powerlite 9010

Repetition Rate (Hz)	10
Energy (mJ)	
1064 nm	2000
532 nm	1000
355 nm	550
266 nm	160
Pulsewidth (ns)	
1064 nm	5-9
532 nm	4-8
355 nm	3-7
266 nm	3-6
Energy stability (±%)	
1064 nm	2.5
532 nm	3.5
355 nm	4
266 nm	8
Power drift (±%)	
1064 nm	3
532 nm	6
355 nm	6
Beam Spatial Profile (fit to Gaussian)	
Near Field (<1 m)	0.7
Far Field (∞)	0.95
Max. deviation from fitted Gaussian (±%)	
Near Field (<1 m)	40

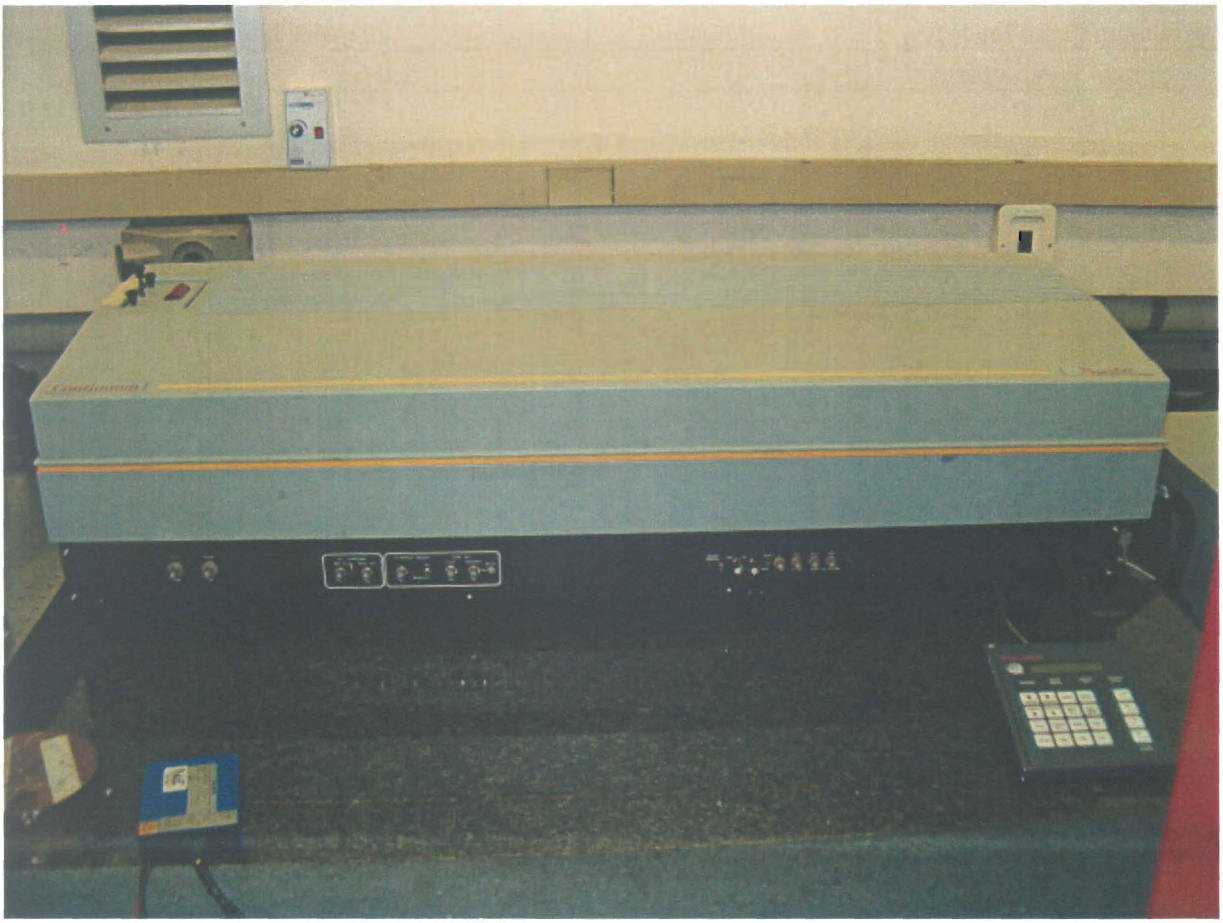

Figure 5.1 Picture taken of the Nd:YAG laser at the CSIR.

Equipment: Optical Parametric Power Oscillator
Brand: Lambda Physik
Model: SCANMATE
Product Specifications:

Table 5.6 Product specifications of the Lambda Physik SCANMATE OPPO

Property	Value
Bandwidth	0.15 cm^{-1}
Tuning Range	420 nm - 2200 nm
Conversion Efficiency:	
signal+idler wave	17%
signal wave at 500 nm	14%
Wavelength Accuracy	0.05 nm
Wavelength Resetabilty	0.6 pm

Minimum Pump Energy	80 mJ at 355
Maximum Pump Energy	500 mJ at 355 nm

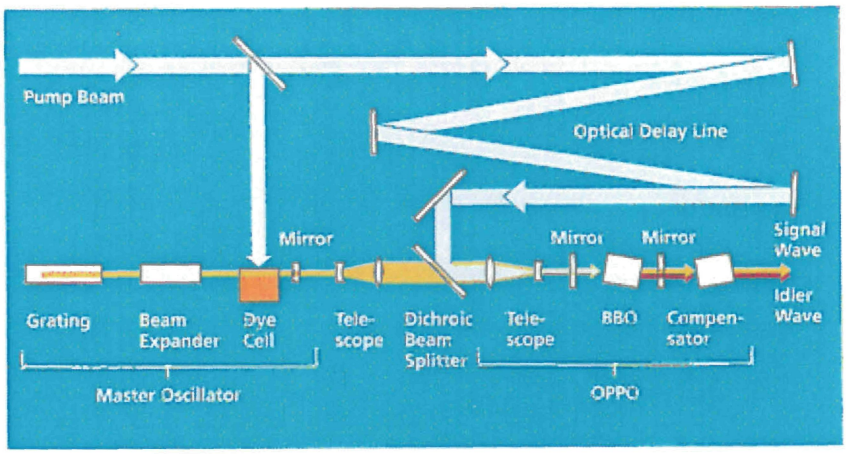

Figure 5.2 Optical scheme of SCANMATE OPPO.

The OPPO is coupled to the seeded Nd:YAG pump laser and used to generate a signal- and idler pulse of higher wavelength, from the 355 nm pump-pulse. For an idler wavelength of 1.67 μm, the signal wavelength was calculated through using equation (1) (5.2.2.2) to be 450 nm.



Figure 5.3 Picture of the SCANMATE OPPO at the CSIR.

Other technical equipment used in the experimental setup includes a Laser Precision Corp RJ-7610 energy radiometer, an Ocean Optics Inc. HR 4000 high-resolution spectrometer and a high pressure gas cell, made from stainless steel. The gas cell was used in all the experiments to act as a reaction chamber. Figure 5.4 gives a picture of the gas cell with the pressure gauge. The windows of the gas cell are made of CaF_2 and are 45 mm in diameter and 3 mm in thickness. These windows were designed by the manufacturers not to absorb light in the near infrared region (NIR).

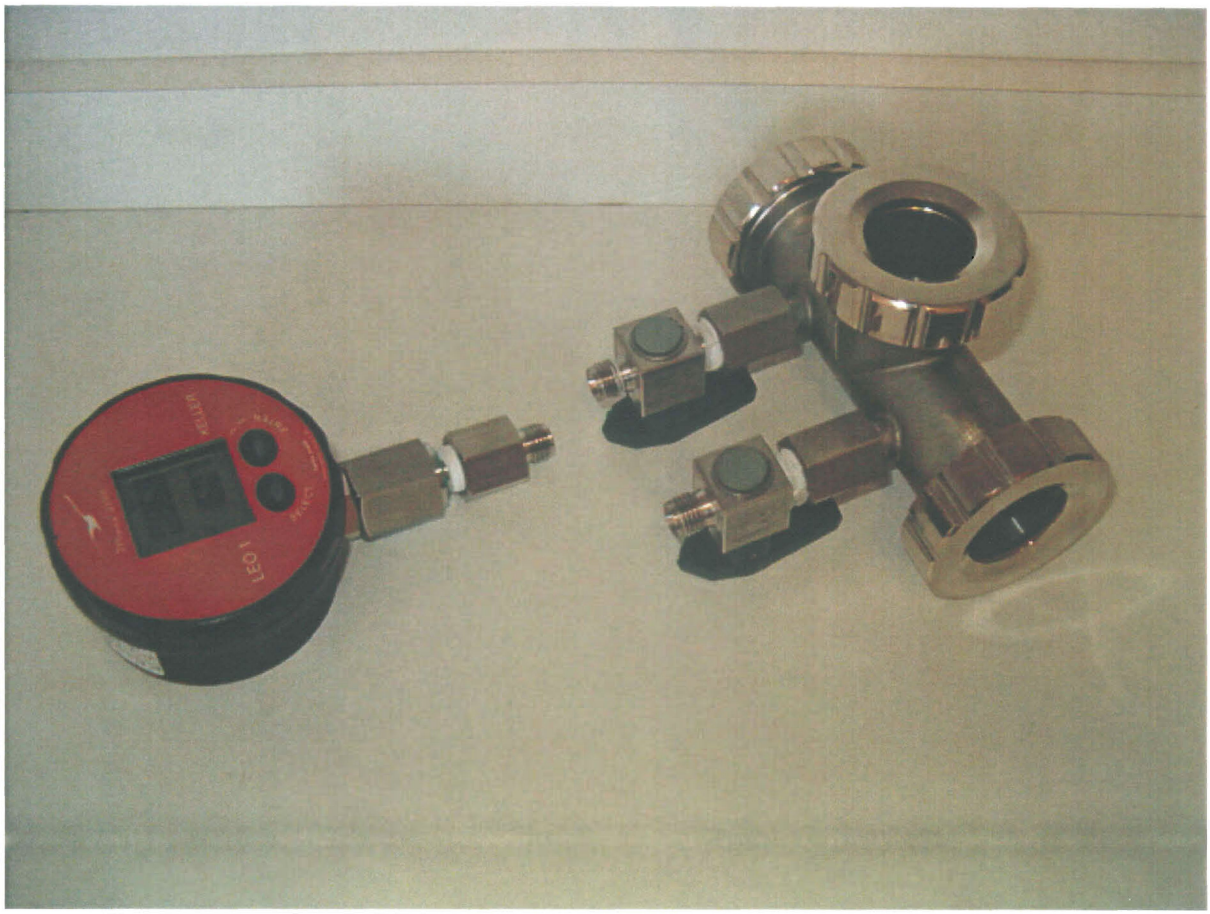

Figure 5.4 High pressure gas cell with pressure gauge used for the experiments.

5.2.2.2 Important calculations and specifications

Calculating the Idler:

When a laser source, of frequency ω_p, provides the pump wave to a nonlinear optical crystal, the optical distortion in the crystal can be thought of as splitting one incident pump photon into two photons of lower energy which are emitted from the crystal. By convention, the emitted higher-frequency photon is termed the "signal" with frequency ω_s and the lower-frequency photon is termed the "idler" with frequency ω_i.

The signal and idler frequencies obey the law of energy conservation

$$\omega_p = \omega_s + \omega_i$$

or in terms of wavelengths

$$1/\lambda_p = 1/\lambda_s + 1/\lambda_i \qquad (1)$$

For a fixed pump wavelength these equations can be fulfilled by an infinite number of signal and idler wavelengths. However, a specific phase relationship of all three waves must also be maintained within the crystal expressed as

$$n_p\omega_p = n_s\omega_s + n_i\omega_i$$

with $n_{p/s/i}$ as the refractive indices at pump, signal and idler frequency, respectively [http://en.wikipedia.org/wiki/Nonlinear_optics; Telle, 2007; http://en.wikipedia.org/wiki/Optical_parametric_oscillator]. The angular dependence of the birefringence (double refraction) in typical nonlinear crystals leads to the selection of three frequencies which meet both conditions. Wavelength tuning is then achieved by simply tilting the crystal (figure 5.5).

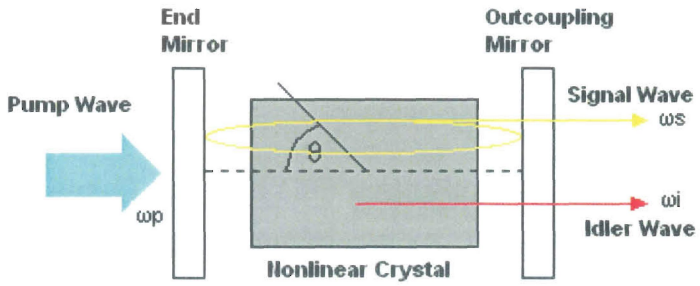

Figure 5.5 Scheme of an optical parametric oscillator with a tilting angle of θ.

For a pump wave of 355 nm, the signal wavelength range is between 420 nm and 710 nm with the idler wavelength range between 710 nm and 2200 nm. Because the OPPO is a broadband tuning device, filters can be used to eliminate the high-frequency signal wave so that only the lower-frequency idler wave is emitted.

Optimization of the Q-switch delay:

In order for the Nd:YAG to perform at peak power, the Q-switch delay must be optimized. This is done by varying the Q-switch delay and measuring the corresponding power output. Table 5.7 gives the measured power outputs with the Q-switch delay.

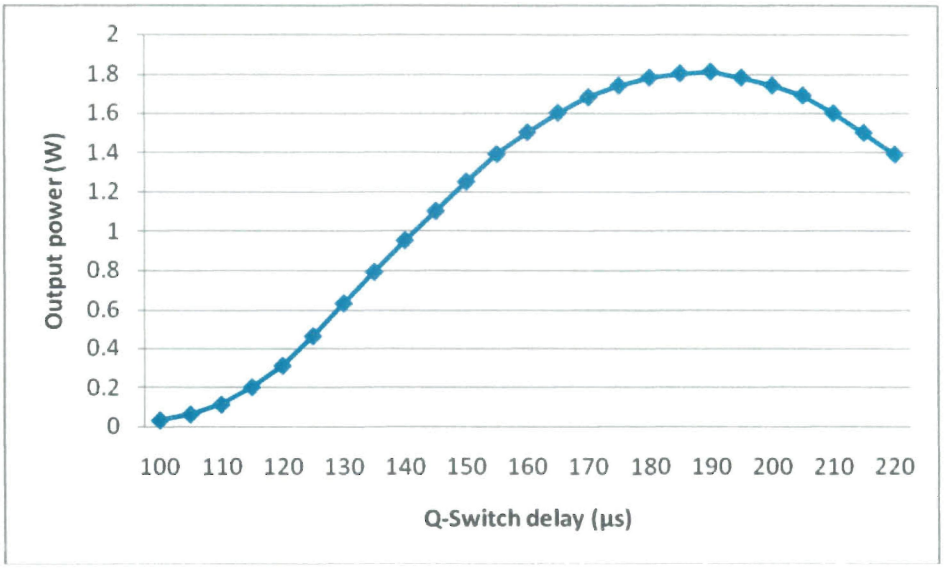

Figure 5.6 Measured power outputs for the Q-switch optimization of the Nd:YAG laser system.

From the curve in figure 5.6 the optimum delay for the Q-switch for the Nd:YAG laser system is at 190 µs. This corresponds to a power output of 1.81 W.

5.2.2.3 Experimental setup and procedures

The objectives of the experiments are to use a nanosecond laser system to radiate a gas or gas mixture inside a closed-windowed reaction chamber for a specified period of time, and then to analyse the products by means of FTIR Spectroscopy. The procedure makes use of an power meter to continuously record the energy introduced into the system. The total energy introduced into the system is then calculated for each experiment and a ratio of the total energy and products formed can then be determined and compared to the results of the femtosecond experiments.

All apparatus of the nanosecond experiments, except for the gas cell, is installed and properly aligned as illustrated in figure 5.7. The Q-switch delay of the seeded Nd:YAG laser system is set to 190 μs for optimum energy output at 355 nm. The Ocean Optics spectrometer and a white sheet of paper, which serves as a scattering material, is used to set the appropriate signal wavelength (see table 5.3) required for the particular reaction. Filters inside the OPPO are set in place to ensure that only the idler wavelength is emitted.

The high pressure gas cell is filled with the appropriate gas or gas mixture at 150 kPa and placed between the OPPO and energy meter as illustrated. Due to the dangers that methane impose in case of a leak, it's important to ensure that a pressure gauge is connected to the gas cell at all times.

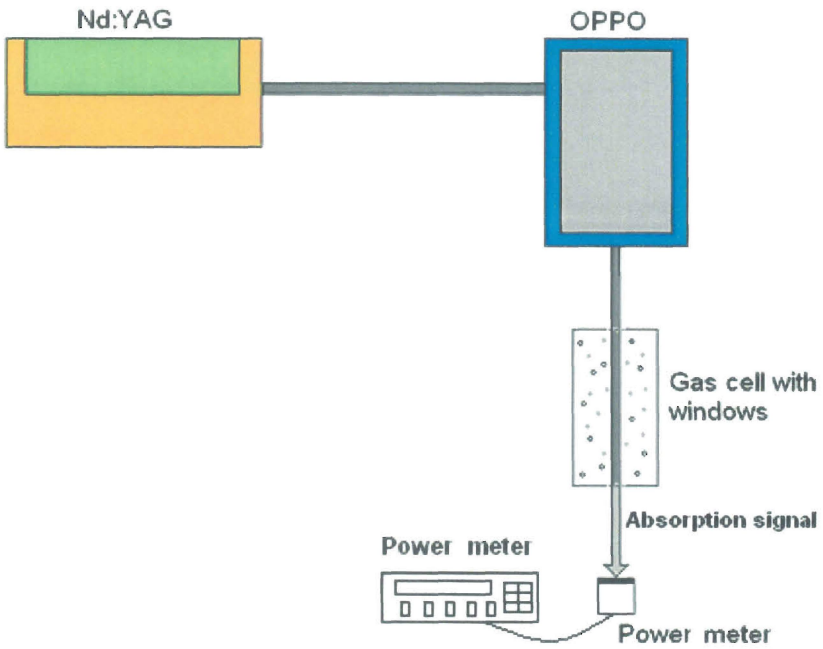

Figure 5.7 Experimental setup for the nanosecond experiments.

Experiments were started by opening the Q-switch of the seeded Nd:YAG pump laser. To ensure that the energy of the laser system remains relatively stable, the system had to be continuously optimized.

After completion of the excitation experiment, the sample is analyzed with the FTIR-spectrometer and safely evacuated.

5.2.3 Femtosecond excitation reactions

5.2.3.1 Equipment

Name: Modelocked solid state Ti:Sapphire oscillator
Brand: Coherent Inc.
Model: Mira 900
Product Specifications:

Table 5.7 System specifications of Mira 900

Parameter	
Output power	
Verdi™- V5 pump	0.65 W
Verdi-V8	1.0 W
Verdi-V10	1.3 W
Innova® 310 8 W	0.8 W
Sabre® 14 W	1.4 W
Tuning Range4	700 to 980 nm
Autocorrelation	<200 fs
Repetition Rate	76 MHz, nominal
Noise	<0.1%
Stability	<3%
Beam Diameter	0.8 mm
Beam Divergence	1.7 mrad
Spatial Mode	TEM_{00}
Polarization	Horizontal
Physical Dimensions	111.1 x 38.1 x 19.7 cm



Figure 5.8 Coherent Inc. Mira 900 modelocked Ti:Sapphire oscillator.

Equipment: Neodymium-doped Yttrium Vanadate laser ($Nd:YVO_4$)
Brand: Coherent Inc.
Model: Verdi-V5
Product Specifications:

Table 5.8 System specifications of Verdi-V5

Parameter	
Output power	>5W
Wavelength	532 nm
Linewidth	<5 MHz
Beam Diameter	2.25 mm ±10%
Beam Divergence	<0.5 mrad
M^2	<1.1
Pointing Stability	<2 μrad/°C
Power Stability	±1%
Noise	<0.03% rms
Polarization	vertical, >100:1



Figure 5.9 Coherent Inc. Verdi-V5 constant wave Nd:YVO_4 pump laser.

Equipment: Solid state Ti:Sapphire regenerative amplifier
Brand: Coherent Inc.
Model: Legend
Product Specifications:

Table 5.9 System specifications of Legend

Parameter	
CenterWavelength (nm)(nominal)	800
Tunability (nm)	770 to 845
Repetition Rate (kHz)	1
Pulse Duration (fs)	<130
Energy/Pulse (mJ)	>3.5 at 1 kHz
Contrast Ratio	>1000:1 pre-pulse >100:1 post-pulse
Energy Stability (rms)(8 hours)	<0.75%
Beam Diameter @ 1/e2 (mm)(typical)	8.5
Spatial Mode	TEM_{00},M^2 <1.35
Polarization	linear,horizontal

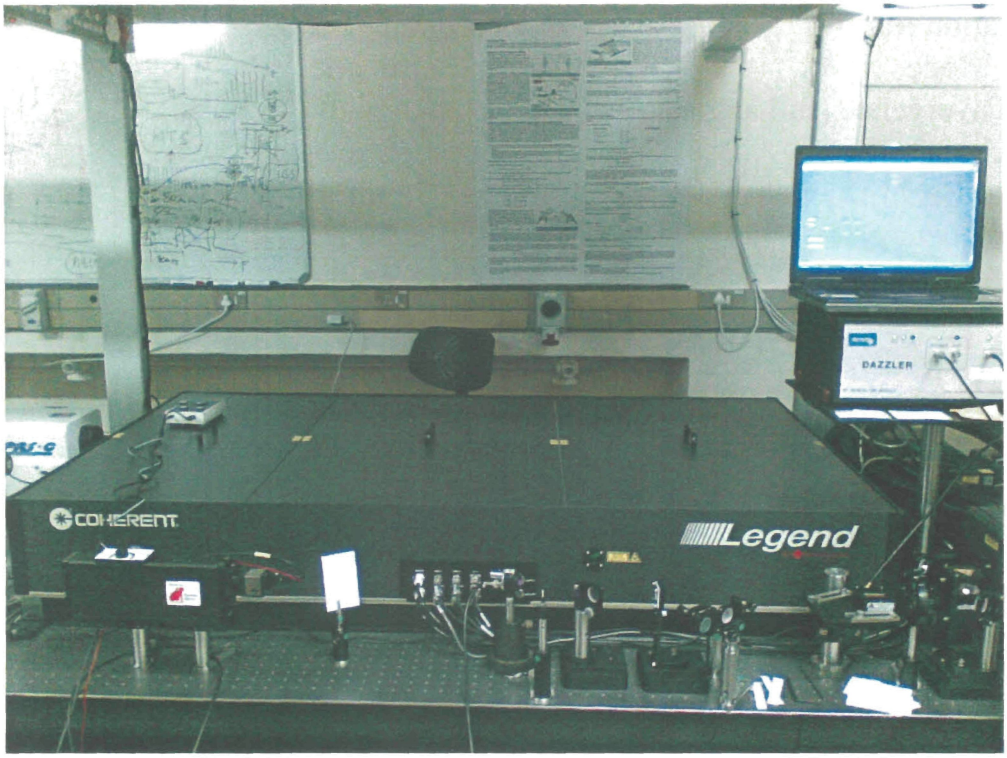

Figure 5.10 Coherent Inc. Ti:Sapphire regenerative amplifier.

Equipment: Solid state diode-pumped Q-switched laser
Brand: Coherent Inc.
Model: Evolution-30
Product Specifications:

Table 5.10 System specifications of Evolution-30

Parameter	
Wavelength	527
Pulse Repetition Rate	1 to 10 kHz
Average Output Power	20W at 1 kHz
	30W at 5 kHz
	30W at 10 kHz
Energy-Per-Pulse	20 mJ at 1 kHz
	6 mJ at 5 kHz
	3 mJ at 10 kHz
Typical Pulse Width (FWHM)	<250 nsec at 1 kHz

Pulse-to-Pulse Energy Stability	<1% RMS
Polarization Ratio	Horizontal, >100:1
Spatial Mode	Multimode
Beam Divergence (full angle)	<10 mrad
Beam Circularity	>80%
Nominal Beam Diameter	3 mm
Line Frequency	50 to 60 Hz



Figure 5.11 Coherent Inc. diode-pumped Q-switched Evolution pump laser.

Other technical equipment used in the experimental setup includes a Coherent 3sigma energy meter, and an Ocean Optics Inc. HR 4000 high-resolution spectrometer. The same high-pressure gas cell, used in the nanosecond experiments, was used for the femtosecond experiments. A Coherent Inc. TOPAS (optical parametric amplifier) was used to generate the 1.6 μm wavelength that was used in the experiments.

5.2.3.2 Experimental setup and procedures

The entire femtosecond laser system used for the excitation experiments is from Coherent Inc. The system consists of a modelocked Ti:Sapphire seed laser (Mira), generating pulses of ~120 fs at a repetition rate of 76 MHz, that is pumped by a 5 W single frequency, continuous wave Nd:YVO_4 pump laser (Verdi). The seed laser is coupled to an amplifier which consists of a pulse stretcher, regenerative amplifier cavity and a pulse compressor. The pulses from the seed are first stretched from ~120 fs to ~200 ps, then amplified in a Ti:Sapphire crystal which is pumped by a Q-switched diode-pumped solid state laser (Evolution), and then coupled out by the Pockels cells. The Evolution pump laser emits high energy (10 mJ) pulses of ~250 ns at a repetition rate of 1 kHz to amplify the seed-pulses. The amplified pulses (1 mJ) are then compressed to ~120 fs at a repetition rate of 1 kHz at 795 nm. The wavelength of the amplified pulses is then converted to 1.6 μm with the TOPAS.

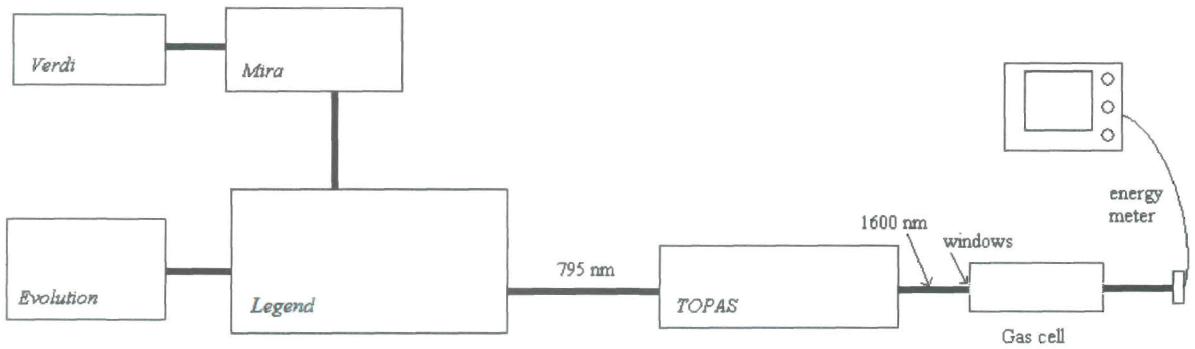

Figure 5.12 Experimental setup for femtosecond experiments.

The filled gas cell (section 5.2.2.3) must be placed behind the TOPAS as indicated in figure 6.12. When all apparatus are correctly installed and the wavelength is changed to 1.6 μm, the gas cell is put in place. As a result of the stability of this laser system, it does not need to be optimized continuously.

After completion of the excitation experiment, the sample is analyzed with the FTIR-spectrometer.

Part 4

Discussion and Conclusion

Chapter 6

Results and discussion

6.1 Molecular modelling

Because molecular modelling is only a tool that can be used to give predictions on certain calculable parameters or –values, it is necessary to compare the values of the calculations with experimental results. However molecular modelling enables us to study systems or factors that cannot be studied under normal conditions. So whatever the circumstance, molecular modelling can most often help to better understand and interpret experimental results.

Many molecular modelling software packages are commercially available to choose from and Spartan and Material Studios are popular choices. These software packages are user-friendly and deliver accurate results for both organic- and inorganic related calculations. As mentioned earlier in chapter 5, for this study both Spartan and Material Studios where used to perform the calculations and with both packages it was necessary to compare the results of the calculations with experimental and known values obtained from literature.

6.1.1 Geometry optimization calculations for methane

A thorough study of the geometry of methane was performed using molecular modelling. This study included a variety of well defined calculations that differed in method and basis set used. This was done to compare the values of the different basis sets with the values recorded in literature. Table 6.1 gives an overview of some of the geometric values calculated with Spartan and their respective literature values.

Table 6.1 Bond properties of methane

	DFT	Moller Plesset	Hartree-Fock			Semi-Empirical			
	B3LYP	MP2	RHF			RHF		MMFF94	
Parameters	6-31G*	6-31G*	STO-3G	3-21G	6-31G*	AM1	MP3	MMFF	Literature*
C-H Bond length (Å)	1.093	1.09	1.083	1.083	1.084	1.112	1.087	1.092	1.093

Total volume ($Å^3$)	33.18	33.12	33.02	33.02	33.03	33.46	33.08	33.16	
Average C-H bond energy(kJ/mol)	413	413	413	413	413	413	413	413	413
H-C-H Bond angle (°)	109.47	109.47	109.47	109.47	109.47	109.47	109.47	109.47	109.5
Heat of formation (kJ/mol)	-74.87	-74.87	-74.87	-74.87	-74.87	-74.87	-74.87	-74.87	-74.87
Molecular weight (g/mol)	16.043	16.043	16.043	16.043	16.043	16.043	16.043	16.043	16.043

*[http://www.science.uwaterloo; http://www.kayelaby.npl]

The data from table 6.1 clearly suggest that the calculated values correspond well with the values obtained from literature. In each calculation the molecule was first geometrically optimized with the Molecular Mechanics method using the MMFF basis set and then optimized using the desired method. Each calculation was done at room temperature (298 K) and in the ground state.

The first parameter to be discussed is the C–H bond length. Literature shows that the bond length of a single C–H bond in the ground state is 1.093 Å. The values for the calculated C–H bond lengths for the corresponding methods and basis sets appear very close to each other and give an average C–H bond length of 1.091 Å. This small difference could be a result of the number of geometry optimization iterations that the calculation used. To reduce the errors of the calculations it can be repeated until satisfactory results have been obtained. This is because calculations will take the results from a previous calculation as the starting point and then use the algorithm to calculate a new set of values for the lowest total energy or optimised state. A calculation with a different method and basis set as the previous calculation will also use this technique and can therefore be combined to give improved results.

The calculated values obtained for the total volume relate to the volume that the methane molecule occupies in space. Theoretically this value will change when the

molecule is excited as a result of the increase in vibrations between the atoms. This case will be discussed in section 6.1.3.

The next set of parameters as in table 6.1, all agree with the values from literature however, it is important to note that the unit for the values obtained for the average bond energy is in kJ/mol. The energy required to break a single C–H bond in a mole of methane is 435 kJ and 1652 kJ for all the bonds thus, on average it gives a bond energy of 413 kJ for all the bonds. However, the aim of this study is not to break a large amount of C–H bonds (number of moles), but rather just a small number so that traces of other species and for instance C–C bond forming can be recorded. For this reason it is necessary to calculate the average energy needed to break one C–H bond. This is done by taking the average dissociation energy for one mole of C–H bonds and dividing it with Avogadro's constant.

$$E_{Avg} = {}^{E_{Dissociation}}/_{N_A}$$
$$= {}^{435000\,J/mol}/_{6.022 \times 10^{23}}$$
$$= 7.224 \times 10^{-19}\,J$$

Considering the amount of energy introduced into the system, one can calculate how many C–H bonds were broken during the excitation experiments. There are however factors, that compromise the effectiveness of the excitation process. These factors include absorption efficiency, internal relaxation and energy transfer, which play a larger role in the nanosecond experiments than in the femtosecond experiments due to the time scales in which these experiments were performed. The influences of these factors will be discussed later in this chapter.

Other calculated parameters, such as the total energy and the room temperature entropy of methane are listed in table 6.2. Only the semi-empirical calculation with the AM1 basis set could not be used to calculate the vibrational zero-point energy and the entropy as only these methods support vibrational- and thermodynamic calculations.

Table 6.2 Theoretical calculations of the total energy, zero point vibrational energy and entropy of methane with the different methods and basis sets.

	DFT	Moller Plesset	Hartree-Fock			Semi-Empirical	
	B3LYP	MP2	RHF			RHF	
Parameters	6-31G*	6-31G*	STO-3G	3-21G	6-31G*	AM1	MP3
Total energy (au)	-40.5184276	-40.3325525	-39.7268637	-39.9768776	-40.1951719	-36.724	-54.4538
Zero-point energy (kJ/mol)	118.898	117.7837	141.864	126.0023	125.4282		119.1925
Entropy (J/mol.K)							
Total	186.0788	186.0702	185.6179	185.6981	185.7416		186.0046
Translational	143.3487	143.3487	143.3487	143.3487	143.3487		143.3487
Rotational	42.4153	42.3384	42.1821	42.1786	42.196		42.2715
Vibrational	0.3148	0.3831	0.087	0.1708	0.1969		0.3843

Table 6.2 shows that methane has an average total energy of ~ -41.70396 au, an average zero-point energy of ~124.8615 kJ/mol and average total entropy of ~185.86853 J/mol.K. The value for the total entropy taken from literature (as in table 2.1) is ~ 188 J/mol.K and therefore correlates well with the calculated value presented in table 6.2. The calculated zero-point energy appears very close for the 6-31G* and MP3 basis sets and change slightly for the lower order basis sets. This is also true for the calculated total entropy.

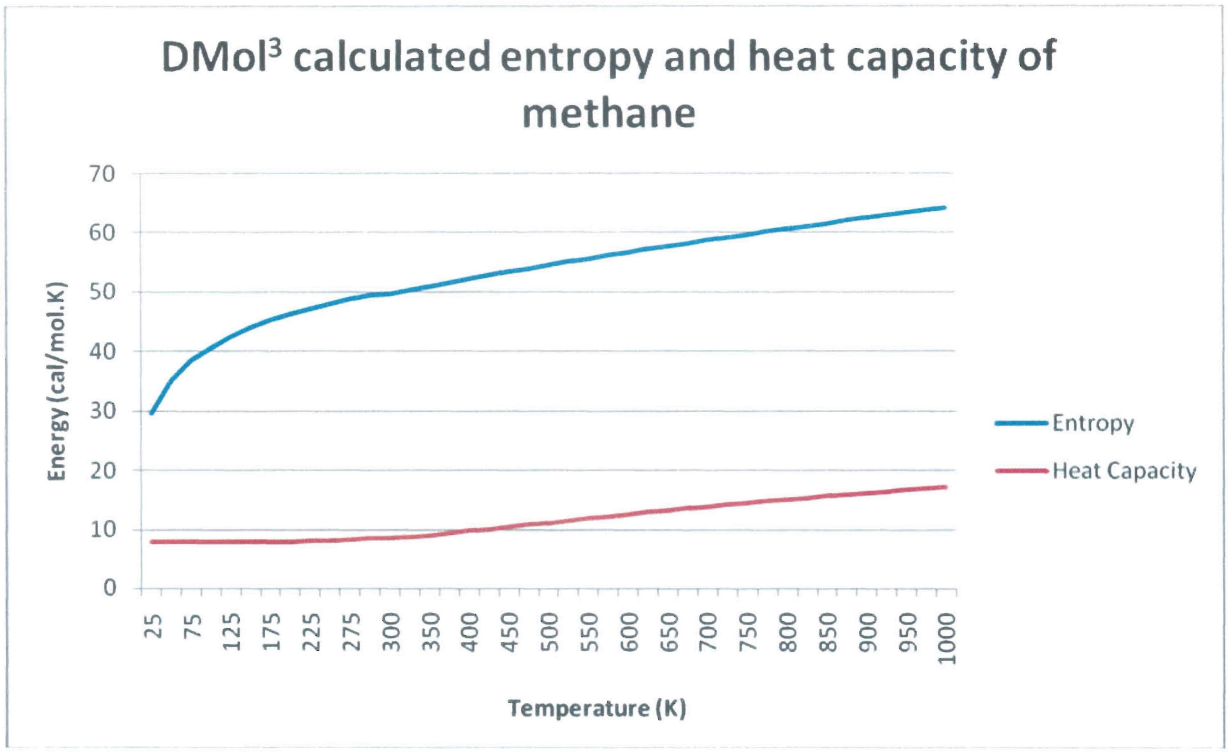

Figure 6.1 DMol³ calculated entropy and heat capacity at different temperature values for methane.

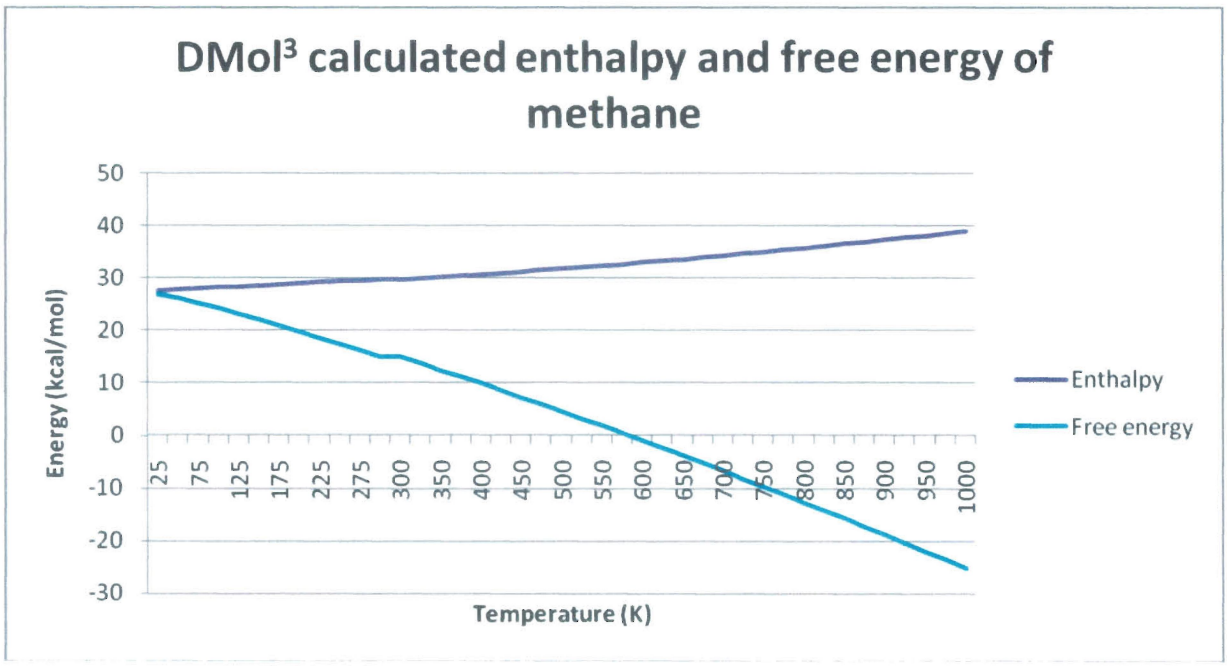

Figure 6.2 DMol³ calculated enthalpy and free energy at different temperature values for methane

6.1.2 Electronic state calculations for methane

It is important to investigate the electronic structure of methane to better understand how the molecule interacts with other molecules in reactions. A simple way to study the electronic structure of a molecule is to analyze a vacuum ultra-violet absorption spectrum of the molecule. From the data obtained from the spectrum, the electronic structure can be determined. The spectrum may also be calculated by using molecular modelling. When using this approach the molecular orbitals of the molecule are calculated and used to draw a molecular orbital diagram.

Table 6.4 shows the calculated energies of the molecular orbitals of methane for each method and basis set used. The blue and orange coloured orbitals indicate the HOMO and LUMO of methane, respectively. All of the methods except for the semi-empirical calculations calculated the energy of the $1a_1$ molecular orbital. This is because the semi-empirical calculations only used the 8 valence electrons of methane to calculate the molecular orbitals while the other methods used all the electrons (altogether 10) to do the calculation. The use of the 10 electrons to calculate the molecular orbital energies do not influence the accuracy of the bonding molecular orbitals since the extra 2 electrons do not take part in bonding.

Table 6.3 Calculated molecular orbital energies (eV) of methane.

	DFT	Hartree-Fock			Semi-Empirical	
	B3LYP	RHF			RHF	
Molecular Orbital	6-31G*	STO-3G	3-21G	6-31G*	AM1	MP3
1a1	-276.65709	-300.13341	-303.25701	-304.90343		
2a1	-18.78406	-24.81795	-25.73814	-25.70257	-28.88355	-29.87947
1t2z	-10.58704	-14.16231	-14.8254	-14.86185	-13.30845	-13.64238
1t2x	-10.58704	-14.16231	-14.8254	-14.86185	-13.30845	-13.64238
1t2y	-10.58704	-14.16231	-14.8254	-14.86185	-13.30845	-13.64238
2t2z	4.8032	19.56858	9.59357	8.91977	4.6605	4.59417
2t2x	4.8032	19.56858	9.59357	8.91977	4.6605	4.59417
2t2y	4.8032	19.56858	9.59357	8.91977	4.6605	4.59417
3a1	3.20845	20.7053	8.07262	6.99498	5.18312	4.24466

The data from table 6.3 suggests that the HOMO of methane, which is a triple degenerate molecular orbital, will have an average energy of -13.56457 eV, where the negative sign (-) indicates a bonding molecular orbital. However, from the calculated data the LUMO of methane can either be a single anti-bonding molecular orbital or a triple degenerate anti-bonding molecular orbital with an average energy of about 5.43626 eV. This difference in degeneracy of the LUMO as obtained by the respective methods is expected since they are all numerical approximations that do not follow the exact same approach. The calculations however suggest that the energy difference between the LUMO and the next unoccupied molecular orbital is very small. Thus, although the degeneracy of the LUMO and the next anti-bonding molecular orbital (as suggested by the calculations) is vague, there is not a large energy difference between them. Therefore using the calculated information, figure 6.3 gives a good representation of how a molecular orbital diagram of methane would look like.

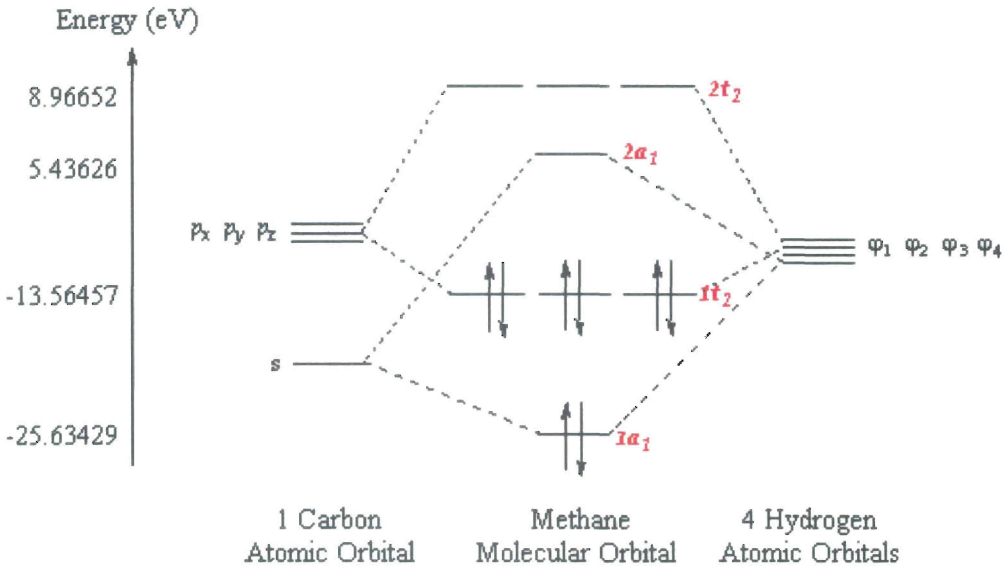

Figure 6.3 The calculated molecular orbital diagram of methane with average molecular orbital energies.

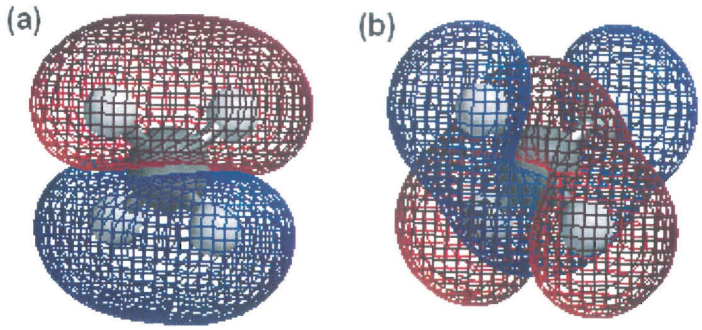

Figure 6.4(a) The HOMO- (b) the LUMO of methane calculated using the Hartree-Fock model and 3-21G basis set.

6.1.3 Excited state calculations for methane

When a molecule is excited, there are a number of changes that take place in the molecule's electronic structure. These changes include orientation, total energy, reactivity, etc. Spartan offers the possibility to calculate some of these properties by using DFT's (B3LYP) method and 6-31G* basis set. Spartan unfortunately does not give a highly detailed output for these types of calculations and therefore only the properties that could be calculated are given in this section. Table 6.5 gives a comparison for some of these properties calculated with DFT's B3LYP method and 6-31G* basis set for both the ground- and first electronic excited state.

Table 6.5 Calculated parameters of ground- and first electronic excited state

Parameter	Ground state	First electronic excited state
Total energy (au)	-40.518476	-40.5184276
Dipole moment (debye)	0	2.7
Total volume ($Å^3$)	33.18	39.41
C-H bond length (Å)	1.093	3.707
H*-C-H Bond angle (°)	n/a	90
H-C-H Bond angle (°)	109.5	120

The calculated data from table 6.4 suggest that there is a very small calculated total energy increase for the first electronic excited state. The reason for this small energy difference is due to the change in symmetry from T_d to D_1. This change is

as a result of the bond between the carbon and the hydrogen that is weakened and then causes the other hydrogens to orient themselves around the carbon in such a manner to minimize the energy. An illustration of this weakened bond between the carbon and the hydrogen is given in figure 6.5.

The calculated dipole moment shows that there is a change from 0 debye to 2.7 debye. The change in calculated total volume is caused by the change in bond length due to the weakening (increase in bond length) of the bond. The elongated bond (figure 6.5) represents the increased inter-nuclear distance between the carbon and the hydrogen.

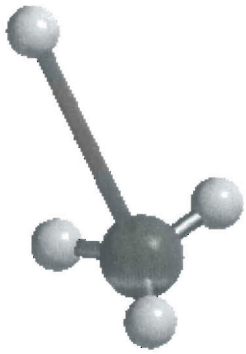

Figure 6.5 Illustration of methane with D_1-symmetry in the excited state, calculated by DFT's B3LYP method and 6-31G basis set.*

The vibration of the carbon and hydrogen atoms can best be described by an anharmonic oscillator. Here the bond between the two atoms acts as an elastic spring where the net force (potential energy) of the spring is least when at rest. This force increases exponentially as the spring is contracted but when stretched increases until the spring deforms or breaks. This principle can best be described by drawing a potential energy curve that shows the potential energy of the spring as a function of distance.

The calculated potential energy curve of methane (figure 6.6) shows the change in bond energy as a function of inter-nuclear distance between the carbon and hydrogen.

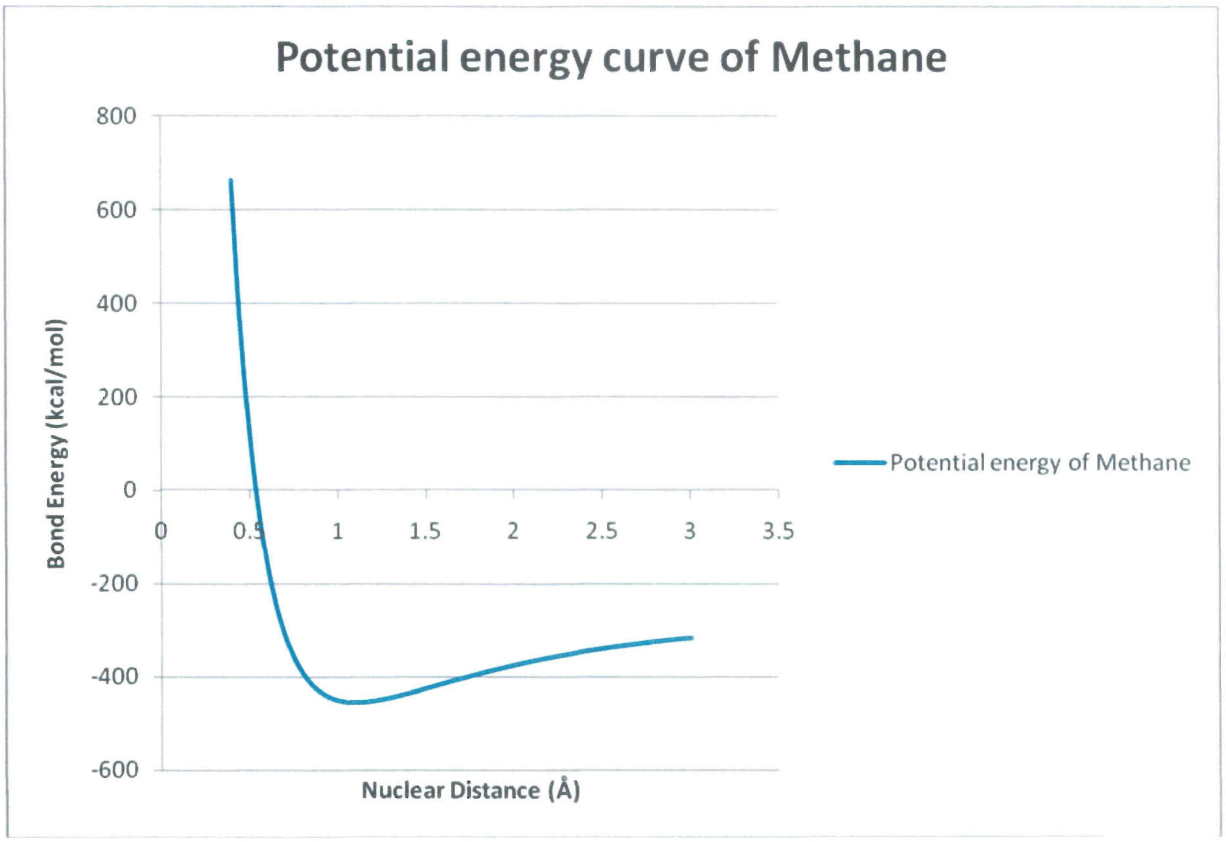

Figure 6.6 Potential energy curve of methane calculated using Material Studios' DMol^3 method and DND basis set.

As already shown, the C–H bond length is 1.093 Å when in the ground state. This means that the potential- or bond energy of the bond is least at that length. As clearly follows from figure 6.6, if the distance between the two atoms is reduced then, the bond energy will increase dramatically (increase in energy represents a decrease in stability) as this inter-nuclear distance or bond length decreases. This is due to the repulsion force that the two atoms exert on each other. On the other hand when the distance between the two atoms is increased, a slower increase in energy occurs. The rate at which the energy will increase will start to decrease until it reaches a critical point, the point of breaking. This happens when the molecule is

excited and the bond energy increases until the distance between the two atoms reaches the point that the bond breaks.

From the calculated data in table 6.4 the length of the C–H bond will be about 3.7 Å when it is excited into the first excited state. This corresponds to a bond energy of about -310 kcal/mol. This means that if the molecule is excited from the ground state there should be an increase in bond energy of ~146.5 kcal/mol (600 kJ/mol). This gives a reasonable correlation to the known dissociation energy, of 435 kJ/mol (see chapter 2), for breaking the first C–H bond in methane.

6.1.4 Vibrational state calculations for methane

The prediction of vibrational spectra is of considerable use in assigning the normal modes in a molecule. Computational methods can be used to calculate and assign these vibrational modes and determine the contributions of each of the different modes. The vibrational spectrum of methane has been extensively studied and determined in gas phase by a series of calculations.

As discussed in chapter 2, methane has four fundamental vibrations. The contributions of each of these fundamentals have been calculated and listed in table 6.5.

Table 6.5 Calculated fundamental vibrations of methane with peak intensities

Wavelength (cm^{-1})									
	DFT	Moller Plesset	Hartree-Fock			Semi-Empirical			
	B3LYP	MP2		RHF		MMFF94	RHF	DMol[3]	
Fundamental mode	6-31G*	6-31G*	STO-3G	3-21G	6-31G*	MMFF	MP3	DND	Literature*
v_4	1375.74	1312.68	1675.98	1520.41	1488.05	1304.99	1363.12	1292.7	1304
v_2	1597.54	1624.66	1903.79	1739.80	1702.63	1471.24	1451.25	1525	1520
v_1	3054.40	3112.39	3525.07	3186.28	3196.78	2839.89	3208.03	2981	2950

v_3	3167.16	3130.70	3785.72	3279.59	3301.25	2981.97	3311.44	3096.7	3030
Intensities Fundamental mode									
v_4	15.46	13.07	6.63	21.26	10.28	≈0	0.86	25.89	
v_2	≈0	≈0	≈0	≈0	≈0	≈0	≈0	≈0	
v_1	≈0	≈0	≈0	≈0	≈0	≈0	0.01	≈0	
v_3	26.38	23.02	0.47	30.09	39.84	≈0	≈0	7.59	

*[Hess, 1980].

The downside of using calculation methods in Spartan and Material Studios to predict the vibrational spectrum of a molecule is that the spectrum will only contain the fundamental vibrations and not overtone vibrations. In order to study the overtone vibrations as well, it has to be determined experimentally.

The calculated data in table 6.5 suggests that the v_3 vibrational band is the strongest infrared active fundamental of methane. This furthermore suggests that, due to the limitations of the laser systems that were used in the excitation experiments, the first overtone ($2v_3$) was chosen as the excitation wavelength. This is because the wavelength of the $2v_3$ overtone is in the 1.6 μm range which is more easily accessible than the 3.3 μm range. The v_4 fundamental is also strongly infrared active and is the most infrared active bend vibration of methane. The calculated v_1 and v_2 fundamentals' intensities are extremely small when compared to the larger v_3 and v_4 intensities.

Through inspection, the calculated data suggests that DMol^3 delivers the closest results to the literature values for all four fundamentals compared to the other computational methods. The Hartree-Fock calculations delivered poor accuracy even for the 6-31G* basis set, while DFT's B3LYP- and Moller Plesset's MP2 methods delivered reasonable results. The semi-empirical calculation only delivered good results for the v_4 and v_2 fundamentals. By using the calculated data a theoretical infrared spectrum, that only contains the four fundamentals, can be drawn. Figure 6.7 gives the calculated theoretical IR-spectrum of methane with

Material Studios' DMol[3]. This IR-spectrum will serve as reference for the experimental FTIR-spectra (section 6.2) to identify the fundamental modes of methane in gas mixtures.

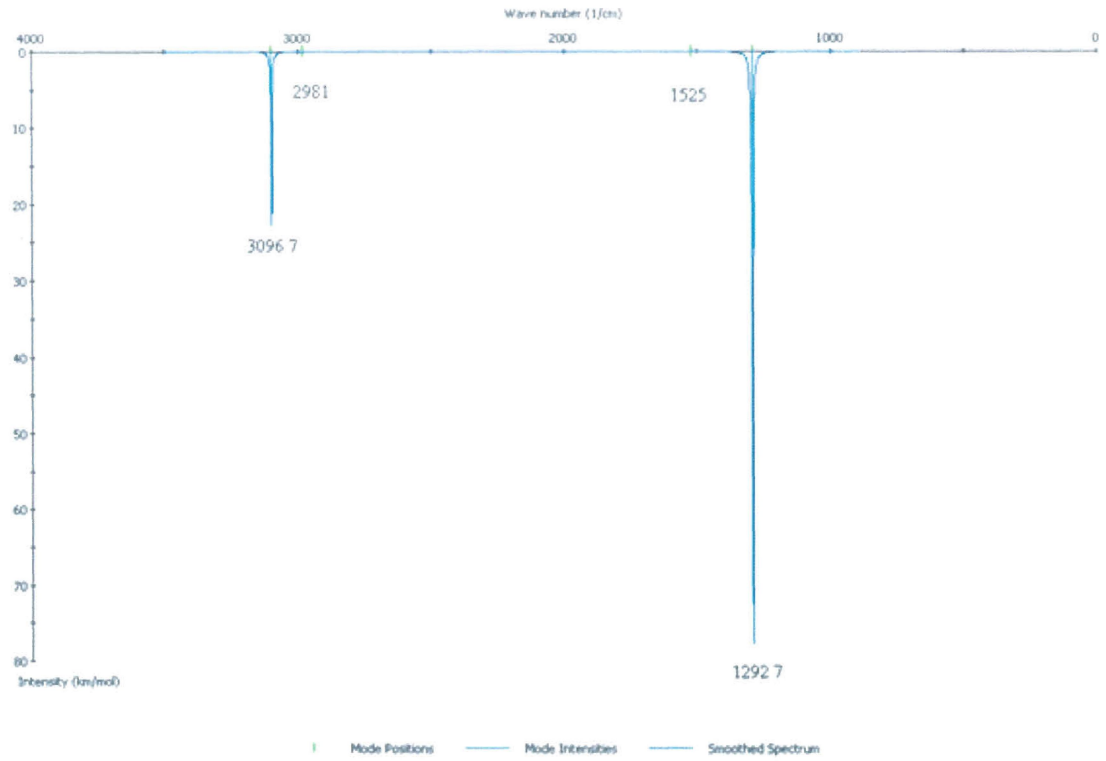

Figure 6.7 DMol[3] calculated IR-spectrum of methane in the gas phase.

The v_2 and v_1 fundamental intensities are not shown as peaks in the spectrum but can be seen by their green markers. The v_1 and v_3 vibrational modes are respectively known as symmetrical- and asymmetrical stretch vibrations and are commonly located in the 3000 cm^{-1} region. The v_2 and v_4 vibrational modes are on the other hand respectively known as symmetrical- and asymmetrical bend vibrations found in the 1200-1500 cm^{-1} region. Figure 6.8(a), (b), (c) and (d) give illustrations of the v_3, v_1, v_2 and v_4 vibrational modes of methane. The arrows in the figures are strategically placed to simulate the movements of the vibrations.

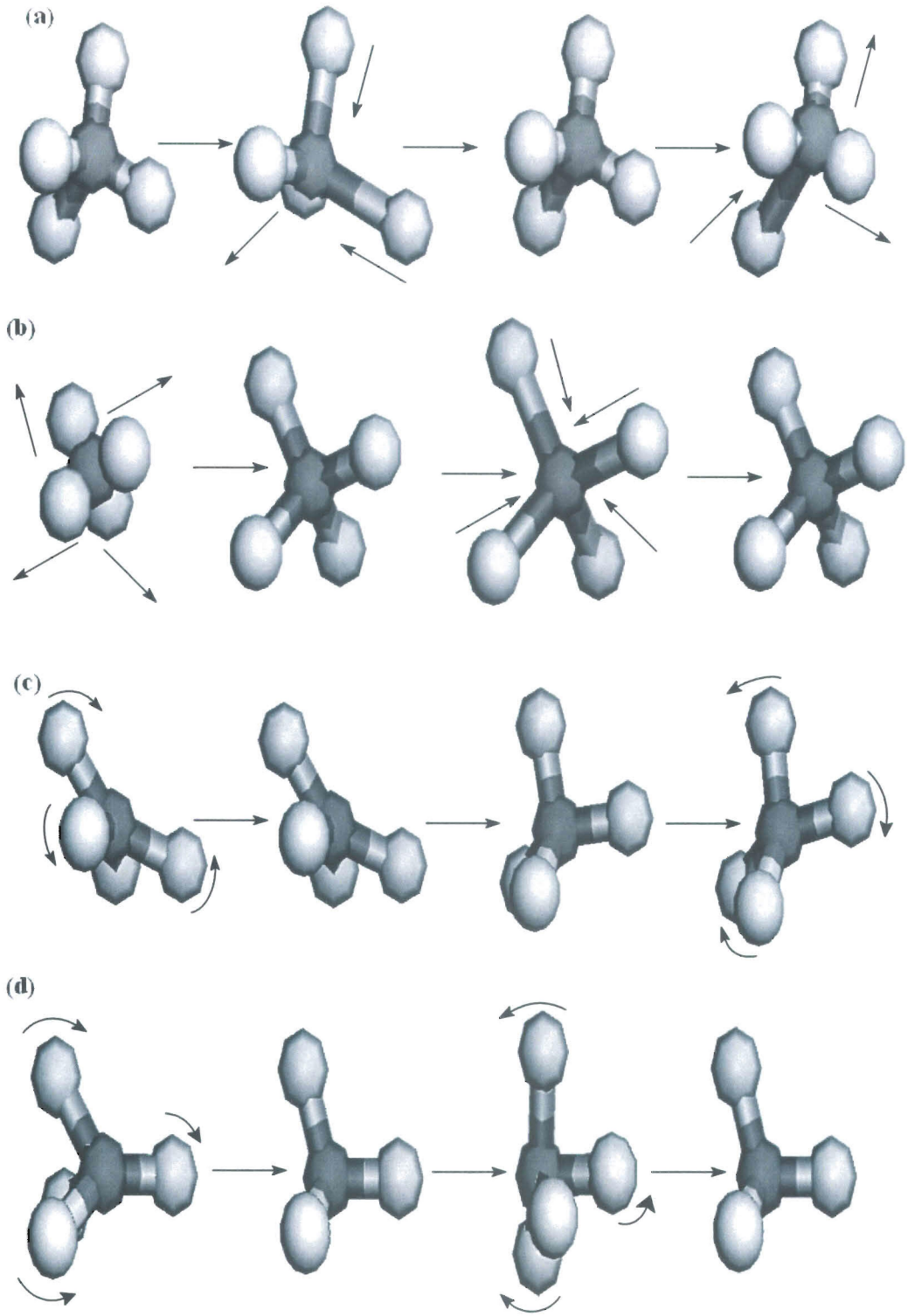

Figure 6.8 Illustrations of the (a) v_3 (b) v_1 (c) v_2 (d) v_4 fundamental vibrations of methane calculated with DMol[3].

6.1.5 Calculations for reactions of methane

This section will discuss calculations regarding the reactions of methane with itself and methane reacting with carbon dioxide. The reactions are studied to identify if laser excitation in the infrared region can indeed be used as a method to initiate reactions with methane without the use of metal catalysts. Section 6.1.5.1 will discuss the calculations affiliated with the reaction of methane with itself and section 6.1.5.2 will discuss the calculations for the reaction of methane with carbon dioxide.

6.1.5.1 Methane reacting with itself

Theoretically the reaction of methane with itself will produce ethane. This reaction occurs in the atmosphere when ultraviolet rays from the sun dissociate methane to form ethane and hydrogen. The ultraviolet photons normally have a wavelength shorter than 160 nm (62500 cm^{-1}) and are therefore in the vacuum ultraviolet region of the electromagnetic spectrum, which suggests that electronic excitation takes place [http://en.wikipedia.org/wiki/Ethane]. The reaction can be summarized as follows: first the ultraviolet photons dissociate the methane molecule into a methyl radical and hydrogen.

$$CH_4 \rightarrow CH_3\bullet + H\bullet$$

Then, two methyl radicals recombine and form ethane.

$$CH_3\bullet + CH_3\bullet \rightarrow C_2H_6$$

The balanced equation then follows as:

$$2\ CH_4 \rightarrow C_2H_6 + H_2 \qquad (1)$$

For this study the use of ultraviolet excitation to dissociate methane will not be employed, but instead the use of photons in the near infrared region will be used (1.6 μm).

A calculation of the thermodynamic- and vibrational properties of ethane has been performed in order to better understand and identify the vibrational modes in the

IR-spectrum. Table 6.6 gives the calculated infrared- and Raman active fundamentals of ethane with their respective contributions.

Table 6.6 Calculated fundamental vibrations of ethane with peak intensities

	DFT B3LYP 6-31G*		DMol[3] DND		Literature*	
Fundamental mode	Wavelength (cm^{-1})	Intensity	Wavelength (cm^{-1})	Intensity	Wavelength (cm^{-1})	Activity
v_1	3199.633	0	2960	0	2954	Raman
v_2	1571.09	0	1371.2	0	1397	Raman
v_3	1003.131	0	1026.1	0	994.11	Raman
v_4	314.832	0	356.2	0	289.32	inactive
v_5	3195.452	53.39	2958.1	45.37	2895.67	IR
v_6	1579.546	6.51	1371	7.95	1379.16	IR
v_7	3267.095	70.28	3054	23.88	2985.39	IR
v_8	1677.925	10.59	1464.6	16.82	1472.03	IR
v_9	921.746	6.74	931.3	7.9	821.72	IR
v_{10}	3240.259	0	3032.7	0	2968.69	Raman
v_{11}	1676.96	0	1453.6	0	1468.1	Raman
v_{12}	1351.561	0	1141.6	0	1195.3	Raman

*[Hepp, 1999]

The calculated data from table 6.6 correspond well with the values found in literature. The literature indicated that only the v_5 to v_9 fundamental modes are infrared-active while the rest of the fundamentals, except for v_4, are Raman-active. This is confirmed by the calculated data that show that only the v_5 to v_9 fundamentals have peak intensities that would suggest that they are infrared active. Therefore, theoretically the calculated IR-spectrum of ethane will only contain 5 fundamental modes. The illustrations of the v_5 to v_8 vibrational modes are given in figure 6.9. This data is to assist with the analysis of the irradiation experiments to potentially identify the fundamentals of ethane that is expected in the methane-only experiments.

Figure 6.10 shows the calculated theoretical IR-spectrum of ethane with DMol^3. The spectrum shows the peaks of the infrared-active fundamentals as well as the locations of the Raman-active fundamentals (green markers).

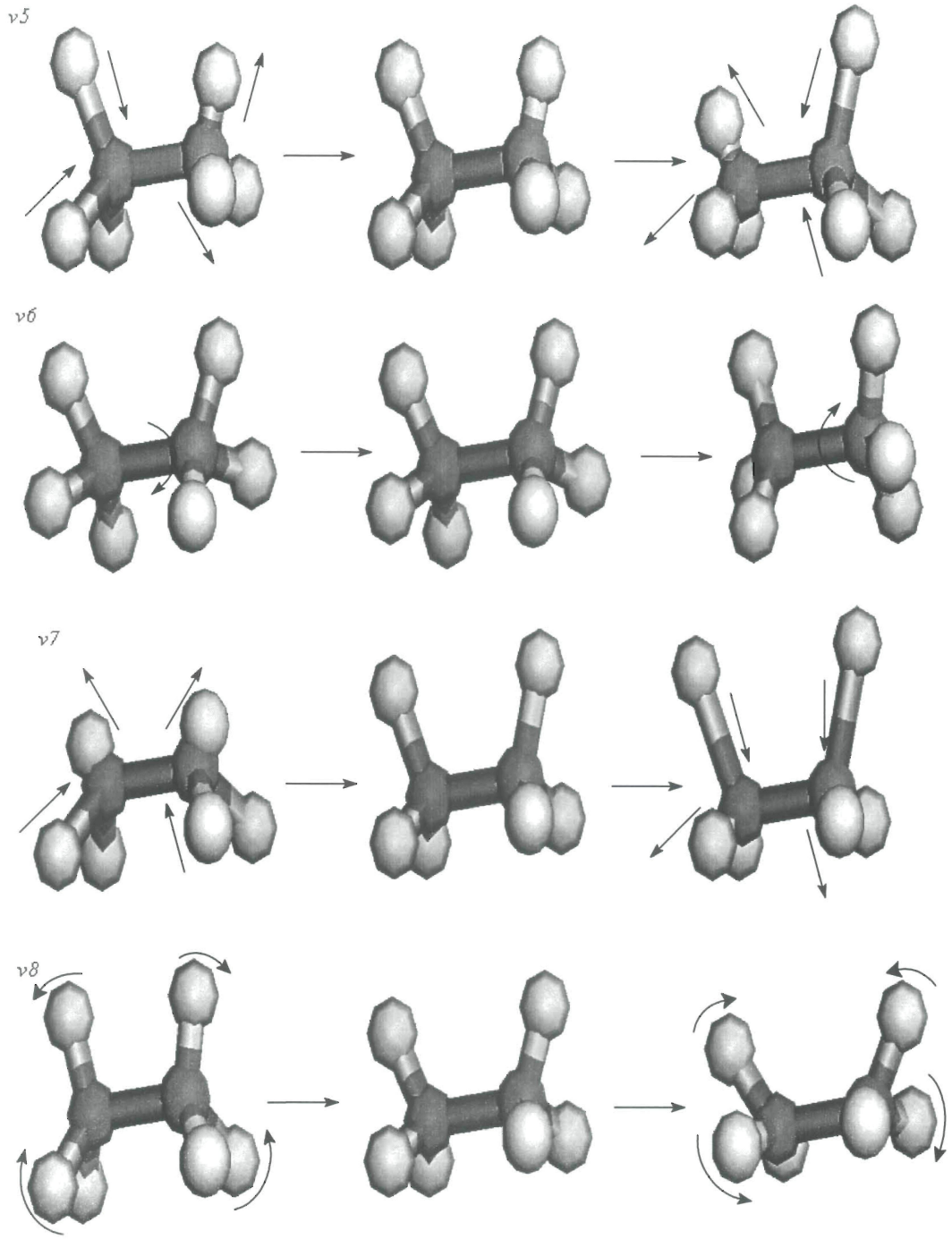

Figure 6.9 Illustrations of the calculated v_5, v_6, v_7 and v_8 fundamental modes of ethane with DMol^3.

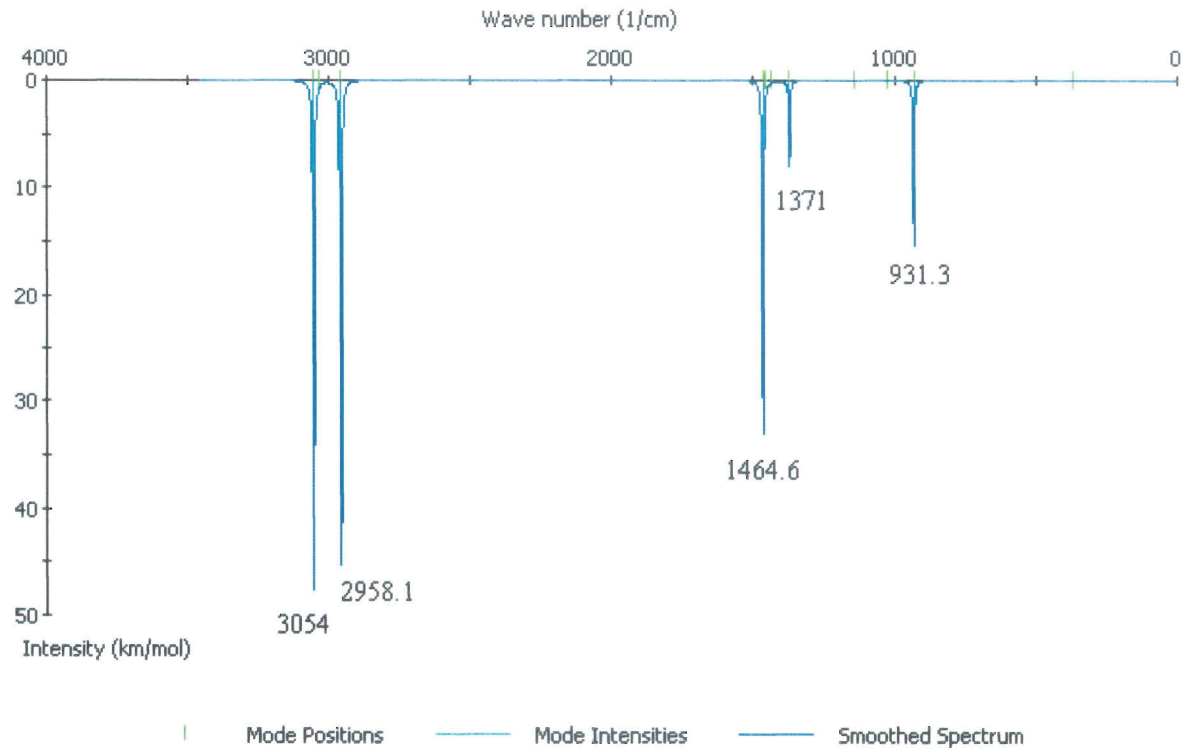

Figure 6.10 DMol[3] calculated IR-spectrum of ethane in the gas phase.

6.1.5.2 Methane reacting with carbon dioxide

The reaction of methane with carbon dioxide is of great importance for the petrochemical industry. These molecules play a dominant role in global warming and are seen as the predecessors to the building blocks for the production of other hydrocarbons and fuels (chapter 2). Most of these processes involved reactions where the molecules were in the presence of a metal catalyst. This study will however investigate the excitation of the molecules with tuneable infrared laser systems.

The balanced theoretical equation of the reaction of methane and carbon dioxide is as follows:

$$CH_4 + CO_2 \rightarrow 2CO + 2H_2$$

In the endothermic reaction, one mole of methane and carbon dioxide react to produce two moles of carbon monoxide and hydrogen, giving a H_2/CO ratio of 1.

This section will discuss the calculated vibrational properties of carbon dioxide in order to get a better understanding of the vibrational modes that could play a role in the reaction with methane. Table 6.7 gives the calculated fundamental vibrational modes of carbon dioxide with their corresponding contributions. The calculations were performed by DFT's B3LYP method and 6-31G* basis set as well as Material Studios' DMol^3 and DND basis set.

Table 6.7 Calculated fundamental vibrations of carbon dioxide with relative peak intensities

	DFT B3LYP 6-31G*		DMol^3 DND		Literature*
Fundamental mode	Wavelength (cm^{-1})	Intensity	Wavelength (cm^{-1})	Intensity	Wavelength (cm^{-1})
ν_2	659.045	65.36	648.4	30.03	641.49
ν_1	1427.566	0	1355.3	0	1373.01
ν_3	2463.39	729.63	2428.1	540.12	2348.1

*[http://www.chemtube3d.com/vibrationsCO2.htm]

The calculated data in table 6.7 suggest that there are only three fundamental vibrations for carbon dioxide. The ν_2–mode, which is the only fundamental bend vibration of carbon dioxide is known as the scissoring bend vibration and found at 641.49 cm^{-1}. The calculation for DMol^3 showed the best accuracy for the calculation of this mode, while DFT's B3LYP-method gave a reasonable result. The remaining two fundamental vibrations of carbon dioxide are known as the ν_1 symmetrical stretch- and ν_3 asymmetrical stretch vibrations and are respectively found at 1373 cm^{-1} and 2348.1 cm^{-1}. The calculated data show that DMol^3 is also more accurate for calculating the ν_1 and ν_3 fundamental mode wavelengths than DFT's B3LYP-method. The calculated intensity of the ν_3 fundamental suggests that it is the strongest infrared active mode of carbon dioxide. This also suggests that its first overtone, $2\nu_3$ can be used for the excitation experiments. This is because it is an easier accessible wavelength (~2 μm) for the available laser systems. Figure 6.11 illustrates the fundamental vibrations of carbon dioxide.

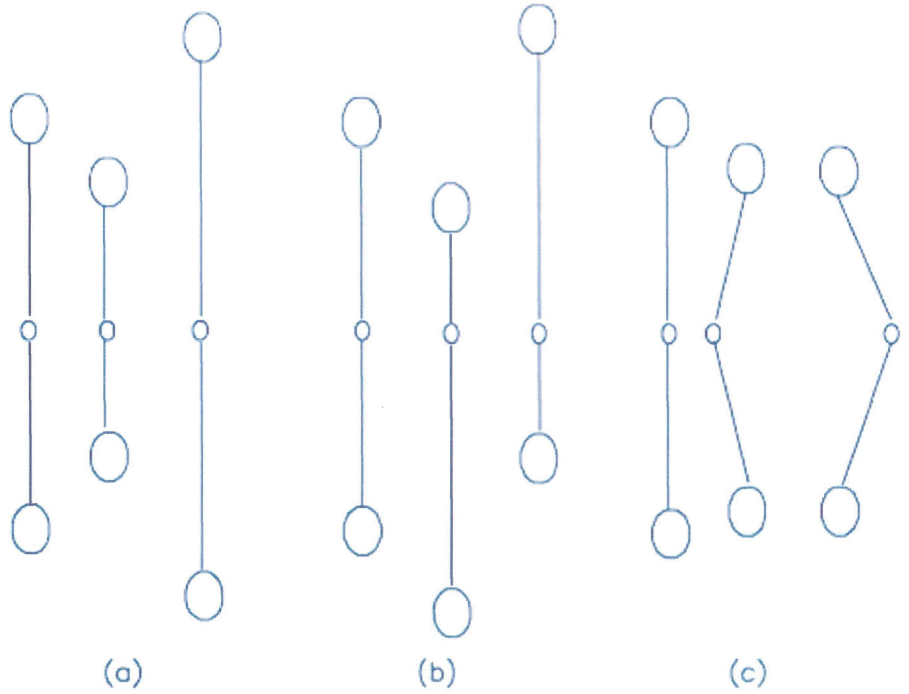

Figure 6.11 Illustrations of the vibrational modes of the (a) v_1-symmetrical *stretch- (b)* v_3*-asymmetrical stretch-, and (c)* v_2*-bend vibrations of carbon dioxide* [http://www.midac.com/apnotes/Tn-100.PDF].

The calculated infrared spectrum of carbon dioxide is shown in figure 6.12. The spectrum only shows the peaks of the v_3 and v_2 fundamentals because the calculated intensity of the v_1 fundamental is too small.

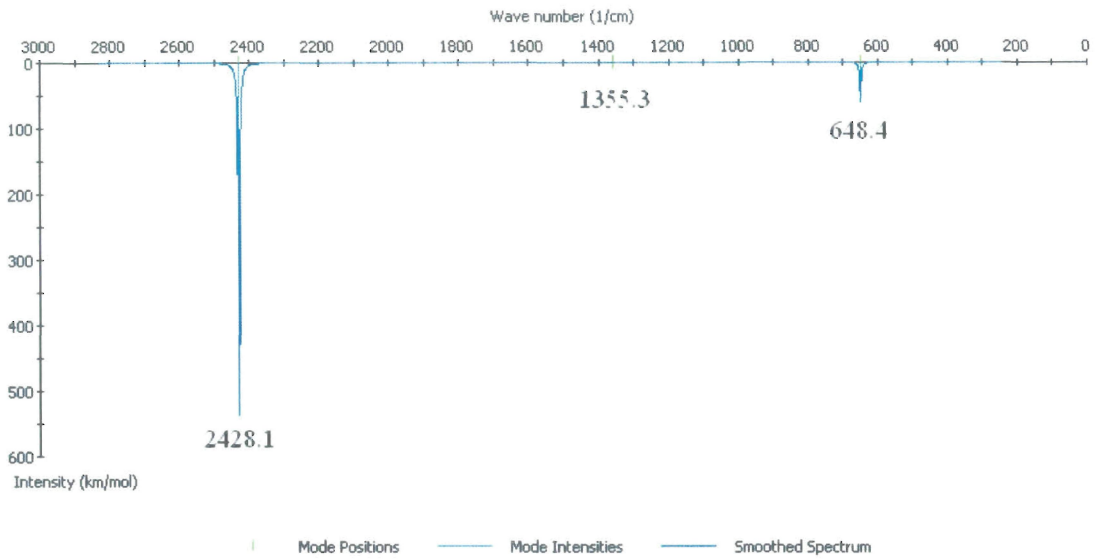

Figure 6.12 DMol³ calculated IR-spectrum of carbon dioxide in the gas phase.

The calculated thermodynamic quantities of carbon dioxide with DMol³ and the DND basis set from 25 K to 1000 K are given in figure 6.13 and figure 6.14.

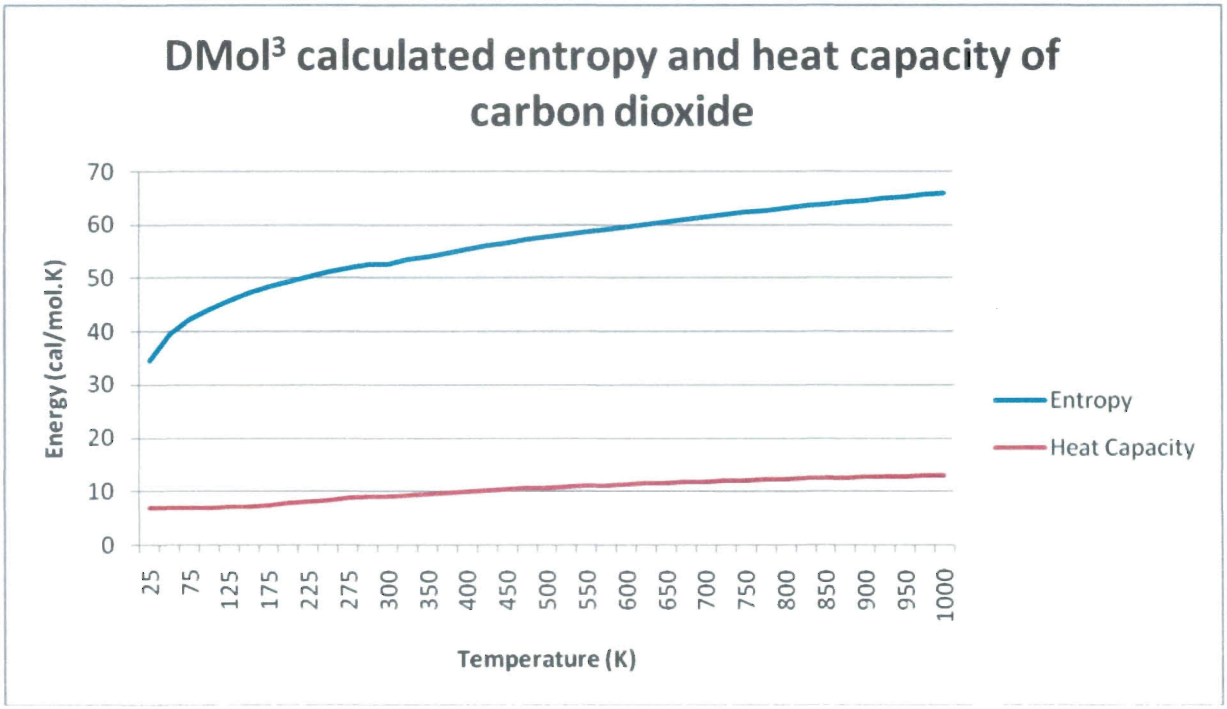

Figure 6.13 DMol³ calculated entropy and heat capacity at different temperature values for carbon dioxide.

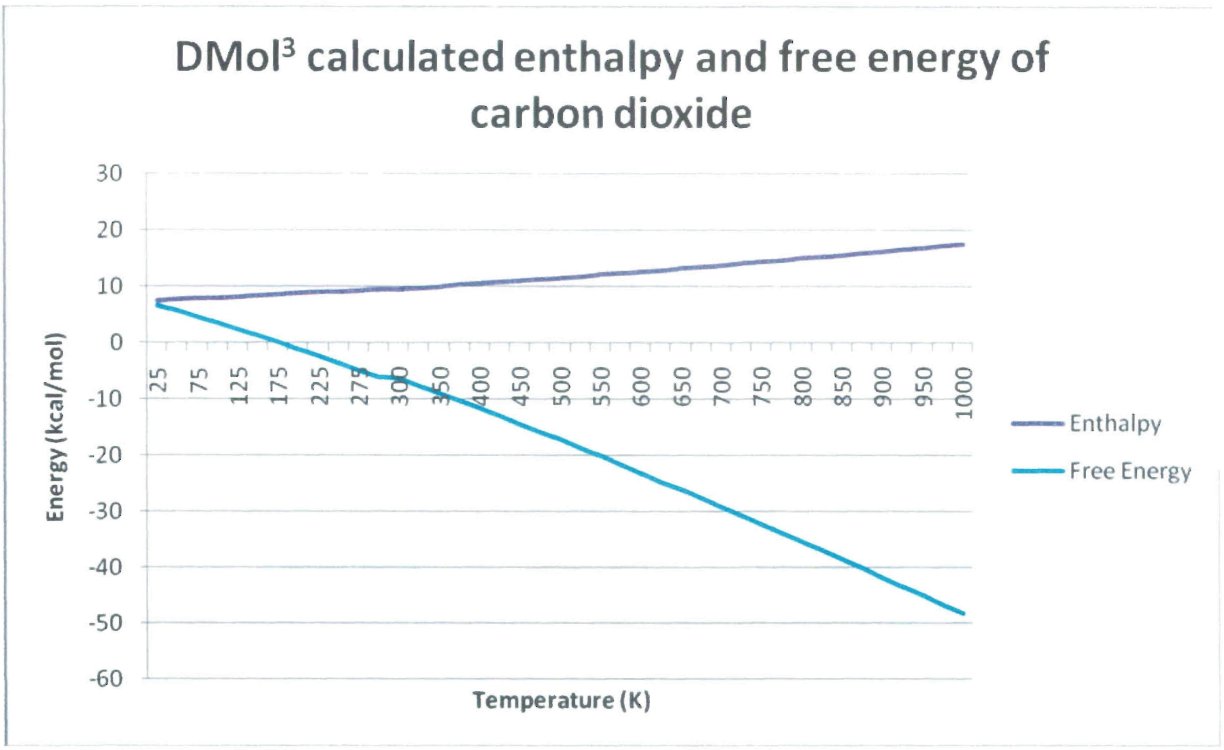

Figure 6.14 DMol³ calculated enthalpy and free energy at different temperature values for carbon dioxide.

6.2 Nanosecond excitation reactions

A detailed discussion of the results obtained with the nanosecond excitation reactions are given in this section. The discussion includes the details of the analyzed experimental results with Fourier-transform Infrared (FTIR) spectroscopy. Calculations concerning the energy introduced into the system are given for each reaction.

6.2.1 Methane reacting with itself

6.2.1.1 Without laser excitation

The experimentally measured FTIR-spectrum of methane in the gas phase is given in figure 6.15. The spectrum is measured in absorbance as a function of wavenumber.

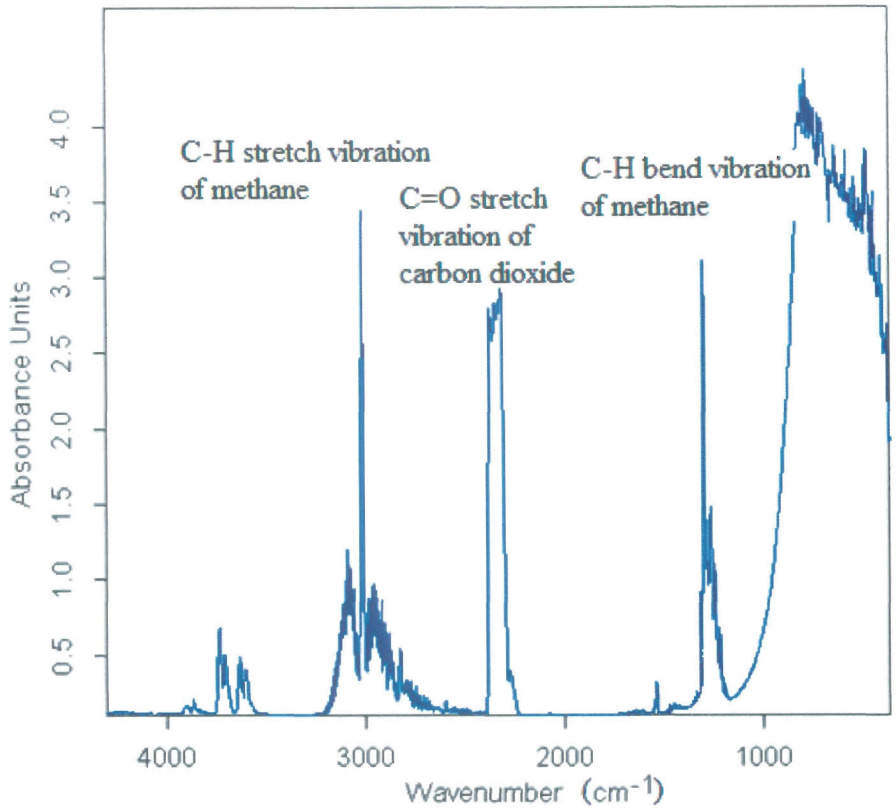

Figure 6.15 FTIR-spectrum of methane in the gas phase before excitation.

Table 6.8 gives the summary of the characterization of the peaks present in the spectrum (figure 6.15).

Table 6.8 Infrared characterization of peaks in methane FTIR-spectrum

Wavenumber (cm^{-1})	Intensity	Description	Remarks
1302.61	Medium - Strong	C-H asymmetric bend vibration	v_4 fundamental of CH_4
1520	Weak	C-H symmetric bend vibration	v_2 fundamental of CH_4
2375.82	Strong	C=O stretch vibration	v_3 fundamental of carbon dioxide
2949.79	Weak	C-H symmetric stretch vibration	v_1 fundamental of CH_4
3060.02	Strong	C-H asymmetric stretch vibration	v_3 fundamental of CH_4
			Thus CH_4 present

The data in table 6.8 confirms that methane is present in the analysed spectrum. Overtone vibrations and combinations thereof are present in the spectrum. These overtones have already been discussed in earlier work done by Hess and co-workers [Hess, 1980]. The spectrum also shows traces of carbon dioxide at 2375 cm^{-1}, which is one of the impurities present in the sample. Apart from these impurities, the spectrum corresponds well with the calculated- and literature values. Two important observations of the experimental spectrum are that there is no evidence of C–C stretch- or bend vibrations nor CH_3-deforming that would suggest other hydrocarbons.

6.2.1.2 Excitation at 1.6 µm

6.2.1.2.1 Three hours experiment

Figure 6.16 shows the FTIR-spectrum of methane taken after 3 hours of excitation. The spectrum is measured in absorbance as a function of wavelength.

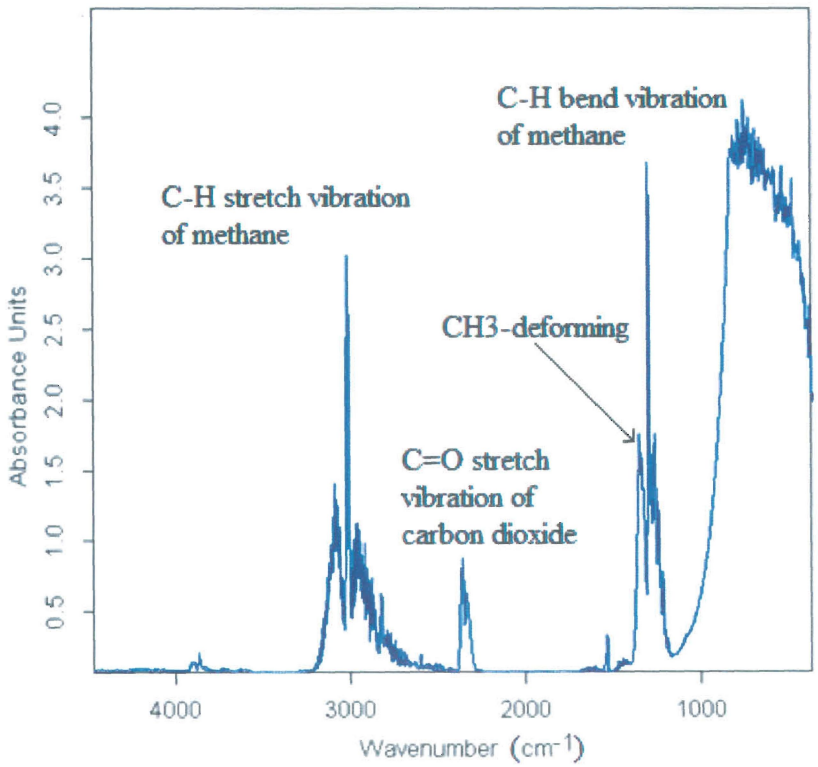

Figure 6.16 FTIR-spectrum of methane after 3 hours of excitation at 1.67 µm.

Table 6.9 gives the characterization of the peaks present in the spectrum (figure 6.16).

Table 6.9 Infrared characterization of peaks in methane FTIR-spectrum

Wavenumber (cm^{-1})	Intensity	Description	Remarks
728.96	Strong	C-C deforming bend vibration	v_9 fundamental of C_2H_6
825.03	Strong	C-H bend vibration	Cis- alkene
1302.42	Strong	C-H asymmetric bend vibration	v_4 fundamental of CH_4
1355	Medium	CH_3-deforming vibration	v_6 fundamental of C_2H_6
1540.43	Weak	CH_3-deforming vibration	v_8 fundamental of C_2H_6
		C-H symmetric bend vibration	v_2 fundamental of CH_4
2908.9	Medium	C-H symmetric stretch vibration	v_1 fundamental of CH_4
2970.2	Strong	C-H asymmetric stretch vibration	v_5 fundamental of C_2H_6 v_3 fundamental of CH_4 v_7 fundamental of C_2H_6 Thus possible CH_4 and C_2H_6 present
3114.98	Weak	=C-H stretch vibration	Cis- alkene Thus possible alkene present

Because the stretch- and bend vibrations of methane and ethane are almost identical, careful interpretation of the spectral data is necessary. The only structural difference between the two molecules is the C–C bond in ethane. As a result of this bond, CH_3-deforming occurs in the region between 1350 cm^{-1} to 1470 cm^{-1}. The data in table 6.9 suggest that vibrational modes that indicate CH_3-deformation are indeed present in the spectrum. It therefore suggests that ethane could have formed during the excitation reaction.

There is also a noticeable difference in the absorption peaks at ~2300 cm^{-1} in figure 6.15 when compared to figure 6.16. These absorption peaks seemed to have almost disappeared in figure 6.16. This could be as a result of possible carbon dioxide dissociation. This carbon dioxide is however only an impurity and is therefore in

small quantities. However, the result of this dissociation could lead to oxidative coupling of methane in which ethane and ethylene is produced. This reaction should therefore explain the =C–H stretch vibrations present in the sample. However oxidative coupling of methane also produces water in the process and this is in conflict with the observations since no water is identified in the gas analysis or visible in the gas cell. As a result, a different reaction called non-oxidative coupling of methane could have taken place. This reaction produces hydrogen instead of water which is more suiting to the observations.

The average energy transferred from the laser system for the three hour-excitation reaction is given in figure 6.17. Each bar indicates the average energy transferred over 3000 pulses (5 minute intervals).

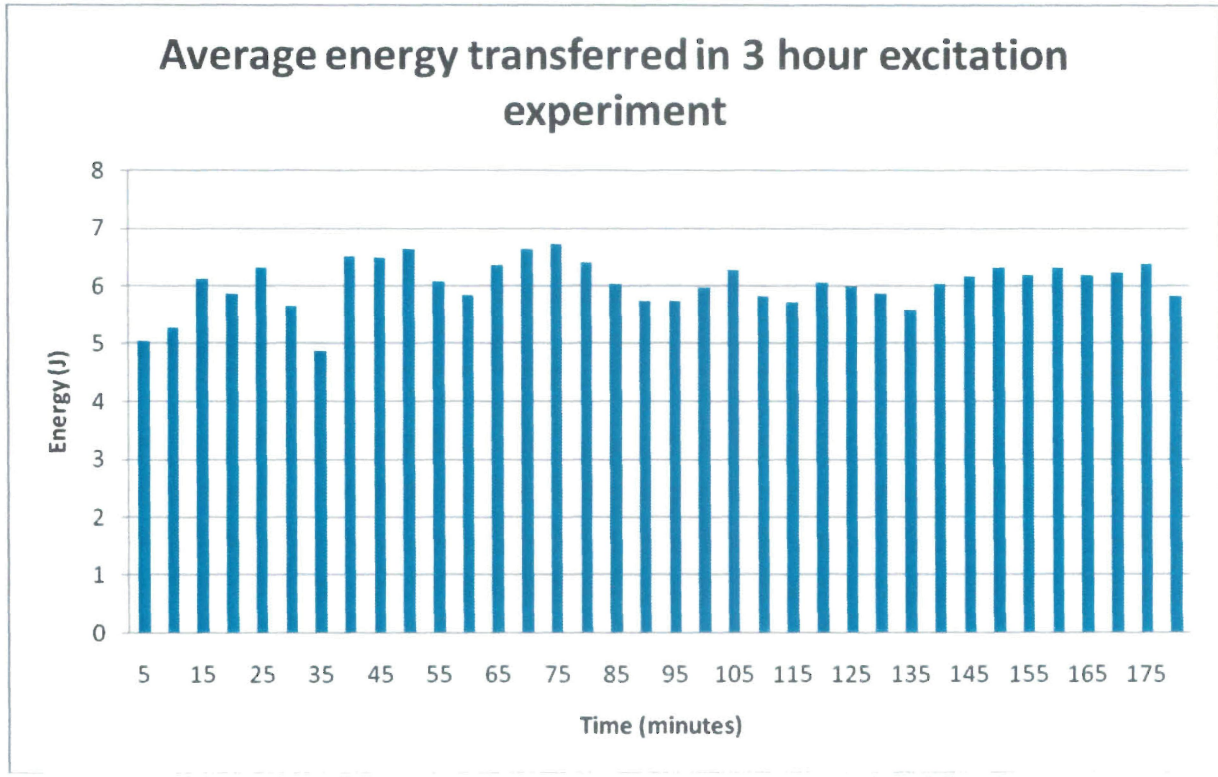

Figure 6.17 Average energy transferred in 5 minute-intervals for three hour-experiment.

The data show that the total amount of energy transferred during the three hours is 217.002 J. This however does not give any information regarding the area of the

laser beam which comes in contact with the gas molecules. Therefore it is necessary to express the energy in terms of fluence. Fluence can be defined as the number of particles (this case radiation) for each unit area. Table 6.10 gives the average pulse energy with the calculated fluence for the 3 hour-experiment.

Table 6.10 Measured pulse energy with calculated fluence

Time (min)	Energy (mJ/pulse)	Fluence (J/cm^2)
5	1.682	0.05354
10	1.759	0.05599
15	2.04	0.06494
20	1.952	0.06213
25	2.1	0.06684
30	1.88	0.05984
35	1.626	0.05176
40	2.164	0.06888
45	2.162	0.06882
50	2.212	0.07041
55	2.026	0.06449
60	1.946	0.06194
65	2.119	0.06745
70	2.212	0.07041
75	2.235	0.07114
80	2.13	0.06780
85	2.01	0.06398
90	1.912	0.06086
95	1.906	0.06067
100	1.988	0.06328
105	2.09	0.06653
110	1.941	0.06178
115	1.901	0.06051
120	2.017	0.06420
125	1.993	0.06344
130	1.95	0.06207
135	1.859	0.05917
140	2.011	0.06401
145	2.055	0.06541
150	2.099	0.06681
155	2.059	0.06554
160	2.101	0.06688
165	2.062	0.06564

170	2.073	0.06599
175	2.121	0.06751
180	1.941	0.06178
	2.009277778	0.06396

The data suggest that the average pulse energy and average fluence of the entire three hour-experiment was 2.0093 mJ and 0,06396 J/cm^2 respectively, with a beam area of 0.031416 cm^2. The average power for the three hour-experiment is then calculated as follows:

$$P = E_{pulse} \times f$$
$$= (2.0093 \text{ mJ}) \times 10 \text{ Hz}$$
$$= 20.093 \text{ mW}$$

6.2.1.2.2 Five hours experiment

Figure 6.14 shows the FTIR-spectrum of methane taken after 5 hours of excitation. The spectrum is measured in absorbance as a function of wavelength.

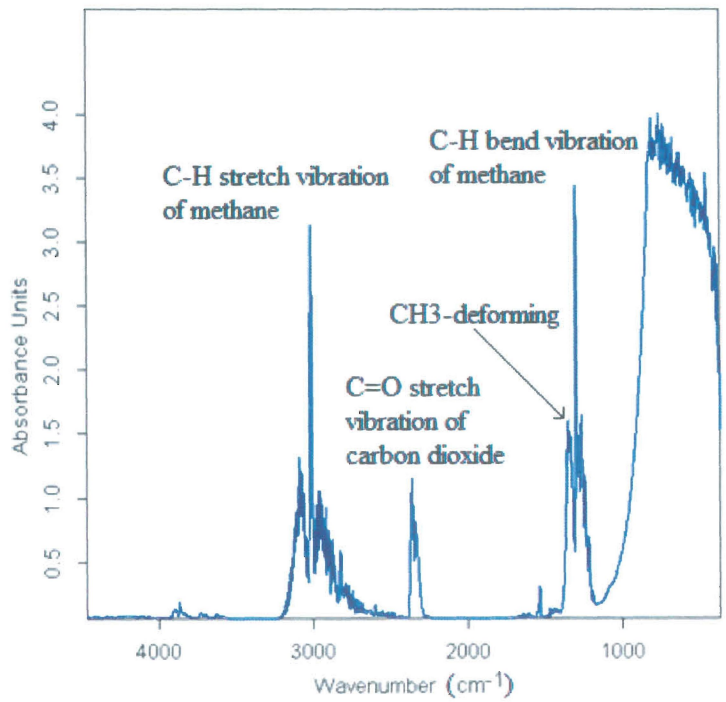

Figure 6.18 FTIR-spectrum of methane after 5 hours of excitation at 1.67 μm.

Table 6.11 gives the characterization of the peaks present in the spectrum (figure 6.14).

Table 6.11 Infrared characterization of peaks in methane FTIR-spectrum

Wavenumber (cm^{-1})	Intensity	Description	Remarks
736.79	Strong	C-C deforming bend vibration	v_9 fundamental of C_2H_6
815.67	Strong	C-H bend vibration	Cis- alkene
1302.5	Medium - Strong	C-H asymmetric bend vibration	v_4 fundamental of CH_4
1355.17	Medium	CH_3-deforming vibration	v_6 fundamental of C_2H_6
1540.51	Weak	CH_3-deforming vibration C-H symmetric bend vibration	v_8 fundamental of C_2H_6 v_2 fundamental of CH_4
2898.83	Weak	C-H symmetric stretch vibration	v_1 fundamental of CH_4
2981.06	Strong	C-H asymmetric stretch vibration	v_5 fundamental of C_2H_6 v_3 fundamental of CH_4 v_7 fundamental of C_2H_6 Thus possible CH_4 and C_2H_6 present
3124.11	Weak	=C-H stretch vibration	Cis- alkene Thus possible alkene present

The data in table 6.11 suggest that there are vibrational modes of methane and possibly ethane present in the spectrum. The intensity of the absorption peaks at ~2300 cm^{-1} in figure 6.18 have decreased which suggest that possibly dissociation of carbon dioxide has occurred. The resulting non-oxidative coupling of methane as previously explained, therefore explains the =C–H stretch vibrations present in the sample.

The average energy transferred from the laser system for the five hour-excitation reaction is given in figure 6.19.

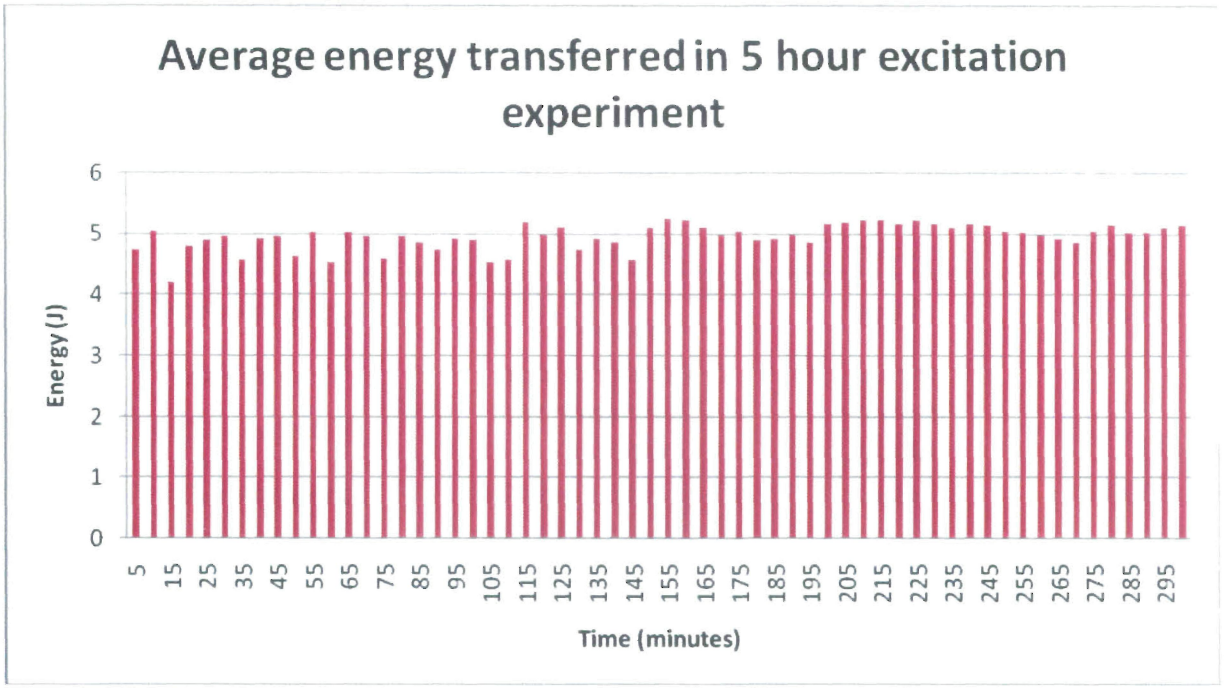

Figure 6.19 Average energy transferred in 5 minute-intervals for five hour-experiment.

The data show that the total amount of energy transferred during the five hours is 296.85 J. The average fluence of the system is then calculated by using the average pulse energy for the entire 5 hours. Table 6.12 gives the average pulse energy with the calculated fluence for the 5 hours in 5 minute intervals.

Table 6.12 Measured pulse energy with calculated fluence

Time (min)	Energy (mJ/pulse)	Fluence (J/cm^2)
5	1.58	0.05029
10	1.68	0.05348
15	1.4	0.04456
20	1.6	0.05093
25	1.63	0.05188
30	1.65	0.05252
35	1.52	0.04838
40	1.64	0.05220
45	1.65	0.05252
50	1.54	0.04902
55	1.67	0.05316
60	1.51	0.04806

65	1.67	0.05316
70	1.65	0.05252
75	1.53	0.04870
80	1.65	0.05252
85	1.62	0.05157
90	1.58	0.05029
95	1.64	0.05220
100	1.63	0.05188
105	1.51	0.04806
110	1.52	0.04838
115	1.73	0.05507
120	1.66	0.05284
125	1.7	0.05411
130	1.58	0.05029
135	1.64	0.05220
140	1.62	0.05157
145	1.52	0.04838
150	1.7	0.05411
155	1.75	0.05570
160	1.74	0.05539
165	1.7	0.05411
170	1.66	0.05284
175	1.68	0.05348
180	1.63	0.05188
185	1.64	0.05220
190	1.66	0.05284
195	1.62	0.05157
200	1.72	0.05475
205	1.73	0.05507
210	1.74	0.05539
215	1.74	0.05539
220	1.72	0.05475
225	1.74	0.05539
230	1.72	0.05475
235	1.7	0.05411
240	1.72	0.05475
245	1.71	0.05443
250	1.68	0.05348
255	1.67	0.05316
260	1.66	0.05284
265	1.64	0.05220
270	1.62	0.05157

275	1.68	0.05348
280	1.71	0.05443
285	1.67	0.05316
290	1.67	0.05316
295	1.7	0.05411
300	1.71	0.05443
	1.65	0.05249

The data suggest that the average pulse energy and average fluence of the entire five hour-experiment was 1.65 mJ and 0.05249 J/cm^2 respectively, with a beam area of 0.031416 cm^2. The average power for the five hour-experiment is then calculated as follows:

$$P = E_{pulse} \times f$$
$$= (1.6492 \text{ mJ}) \times 10 \text{ Hz}$$
$$= 16.492 \text{ mW}$$

It is important to express the excitation energy in terms of power (Watt), since the time of excitation does not give any information on the energy being transferred. As a result, by increasing the irradiation power the excitation time can be shortened.

6.2.2 Methane and carbon dioxide reactions

6.2.2.1 Without laser excitation

This section will discuss the reactions containing the 1:1 methane and carbon dioxide gas mixture. The FTIR-spectrum of the gas mixture is given in figure 6.16. The spectrum will serve as a basis to identify any possible products formed in the excitation reactions.

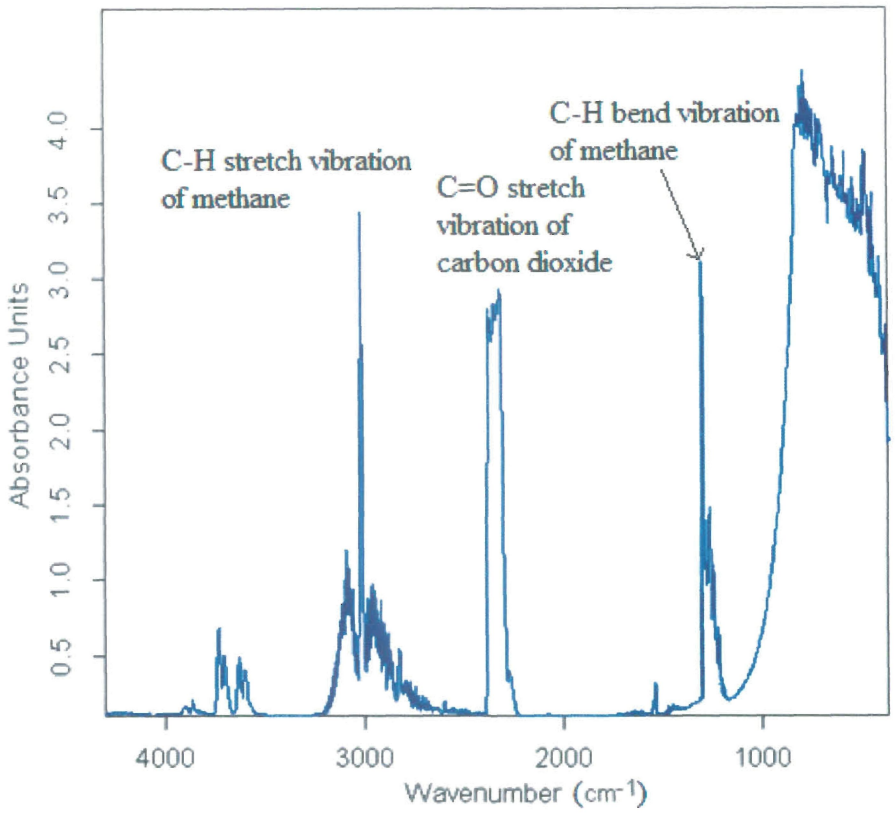

Figure 6.20 The FTIR-spectrum of the 1:1 methane and carbon dioxide gas mixture before excitation.

The spectrum shows the peak intensities in absorbance units as a function of wavenumber. Table 6.13 gives the characterization of the peaks present in the FTIR-spectrum of figure 6.20.

Table 6.13 Infrared characterization of peaks in methane and carbon dioxide mixture

Wavenumber (cm^{-1})	Intensity	Description	Remarks
658.22	Strong	C=O bend vibration	v_2 fundamental of CO_2
1303.07	Medium - Strong	C-H asymmetric bend vibration	v_4 fundamental of CH_4
1354.93	Medium	C=O symmetrical stretch vibration	v_1 fundamental of CO_2
2303.75	Strong	C=O asymmetrical stretch vibration	v_3 fundamental of CO_2

			Thus CO_2 present in mixture
2960.03	Weak	C-H symmetric stretch vibration	v_1 fundamental of CH_4
3016.11	Strong	C-H asymmetric stretch vibration	v_3 fundamental of CH_4 Thus CH_4 present in mixture

The experimental data in table 6.13 correlate well with the calculated data (discussed in section 6.1) for the vibrational modes of both methane and carbon dioxide. This proves that the FTIR-spectrum taken in figure 6.20 do contain methane and carbon dioxide as indicated in the spectrum.

6.2.2.2 Excitation at 1.6 µm

6.2.2.2.1 Three hours experiment

The FTIR-spectrum taken of the gas mixture after 3 hours of excitation is given in figure 6.21.

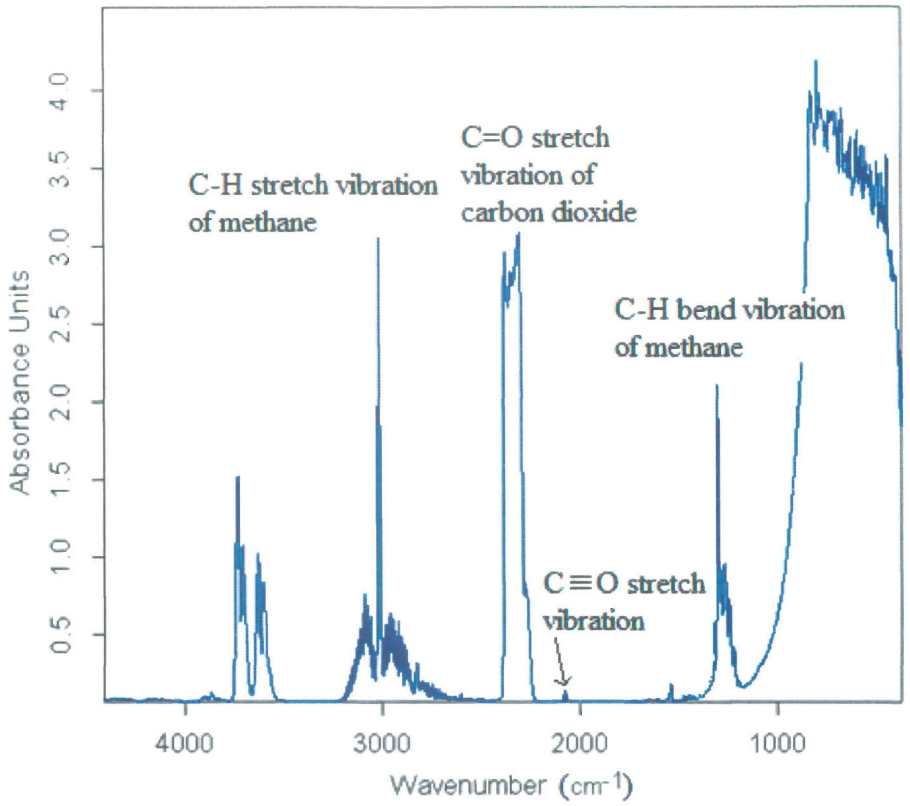

Figure 6.21 The FTIR-spectrum of the 3 hours excited methane and carbon dioxide gas mixture at 1.6 μm.

The spectrum shows the peak intensities in absorbance as a function of the wavenumber. Table 6.14 gives the characterization of the peaks present in the FTIR-spectrum of figure 6.21.

Table 6.14 Infrared characterization of peaks in methane and carbon dioxide mixture

Wavenumber (cm^{-1})	Intensity	Description	Remarks
450 - 890	Strong (Broad)	C=O bend vibration	ν_2 fundamental of CO_2
1304.68	Strong	C-H asymmetric bend vibration	ν_4 fundamental of CH_4
1356.79	Medium - Strong	C=O symmetrical stretch vibration	ν_1 fundamental of CO_2
1542.07	Weak - Medium	C-H symmetric bend vibration	ν_2 fundamental of CH_4

2078.62	Weak	C≡O stretch vibration	Only vibrational mode of CO Thus possible CO present
2350.75	Strong	C=O asymmetrical stretch vibration	ν_3 fundamental of CO_2 Thus CO_2 present in mixture
2950.98	Medium	C-H symmetric stretch vibration	ν_1 fundamental of CH_4
3018.53	Strong	C-H asymmetric stretch vibration	ν_3 fundamental of CH_4 Thus CH_4 present in mixture
3600	Medium	OH stretch vibration	Possible alcohol present

The experimental data in table 6.14 suggest that both methane and carbon dioxide are still present in the gas mixture. There is however, a noticeable difference if the FTIR-spectrum of the 3 hours excited (figure 6.21) and the FTIR-spectrum of the reference (figure 6.20) is compared with one another. In figure 6.21 at 2078.62 cm^{-1} there is an absorption peak indicating the C≡O stretch vibrations of carbon monoxide. This peak is not present in figure 6.20 and thus suggests that carbon monoxide has possibly formed during the excitation reaction. Theoretically, this is what is predicted by the reaction equation (section 6.1.5.2) and should therefore indicate that the reaction occurs. The absorption peak of the C≡O vibration is very weak because there is only a small difference in dipole moment. The reason for this is because although oxygen is more electronegative (greater electronegativity) than carbon, the energy of the HOMO is closer to that of carbon's p-orbitals which results in a greater electron density at the carbon atom. This is also the reason why all reactions involving carbon monoxide occurs through the carbon and not the oxygen. The absorption peak at 3600 cm^{-1} is characteristic of an alcohol OH stretch vibration.

Figure 6.22 shows a graph of the energy put into the system as a function of time.

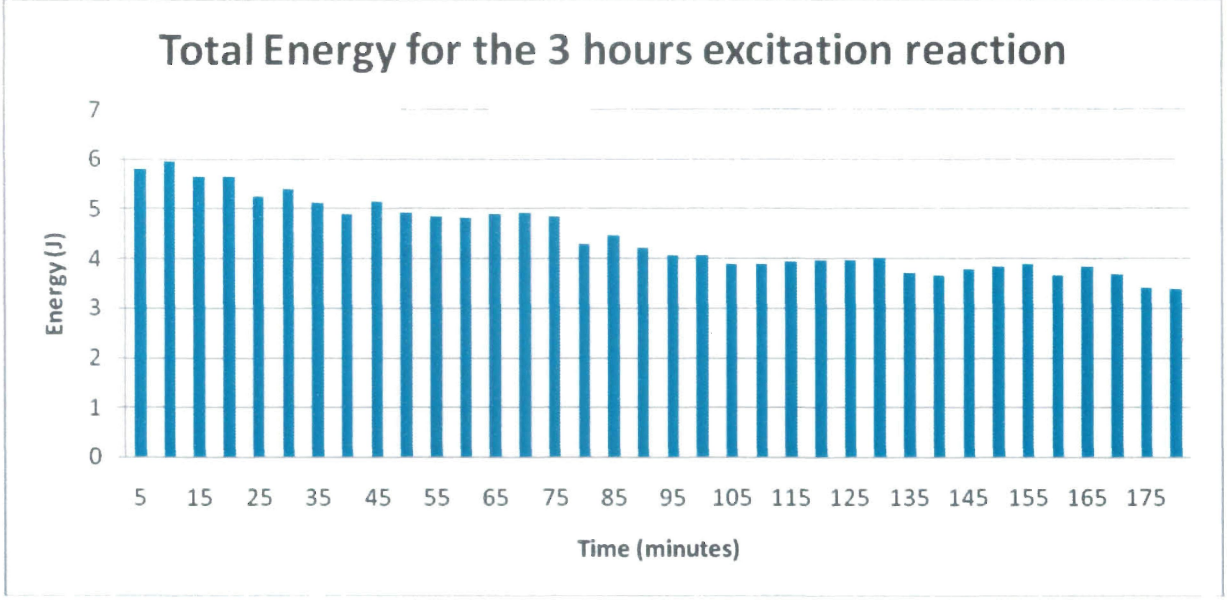

Figure 6.22 The measured energy put into the system for the three hours mixed gas excitation experiment.

The bars indicate the energy of the 3000 pulses for each 5 minutes. This gives a total energy of 159.96 J entered into the system. The average fluence of the system is then calculated by using the average pulse energy for the entire 3 hours. Table 6.15 gives the average pulse energy with the calculated fluence for the 3 hours in 5 minute intervals.

Table 6.15 Measured pulse energy with calculated fluence

Time (min)	Energy (mJ/pulse)	Fluence (J/cm^2)
5	1.94	0.06175
10	1.99	0.06334
15	1.89	0.06016
20	1.89	0.06016
25	1.75	0.05570
30	1.8	0.05730
35	1.71	0.05443
40	1.63	0.05188
45	1.72	0.05475
50	1.64	0.05220
55	1.62	0.05157
60	1.61	0.05125
65	1.63	0.05188

70	1.64	0.05220
75	1.62	0.05157
80	1.43	0.04552
85	1.49	0.04743
90	1.41	0.04488
95	1.36	0.04329
100	1.36	0.04329
105	1.3	0.04138
110	1.3	0.04138
115	1.31	0.04170
120	1.32	0.04202
125	1.32	0.04202
130	1.34	0.04265
135	1.24	0.03947
140	1.22	0.03883
145	1.26	0.04011
150	1.28	0.04074
155	1.3	0.04138
160	1.22	0.03883
165	1.28	0.04074
170	1.23	0.03915
175	1.14	0.03629
180	1.13	0.03597
	1.48	0.04715

The data suggest that the average pulse energy and average fluence of the entire three hour-experiment was 1.48 mJ and 0.04715 J/cm^2 respectively, with a beam area of 0.031416 cm^2. The average power for the three hour-experiment is then calculated as follows:

$$P = E_{pulse} \times f$$
$$= (1.4811 \text{ mJ}) \times 10 \text{ Hz}$$
$$= 14.8111 \text{ mW}$$

6.2.2.2.2 Five hours experiment

The FTIR-spectrum taken of the gas mixture after 5 hours of excitation is given in figure 6.23.

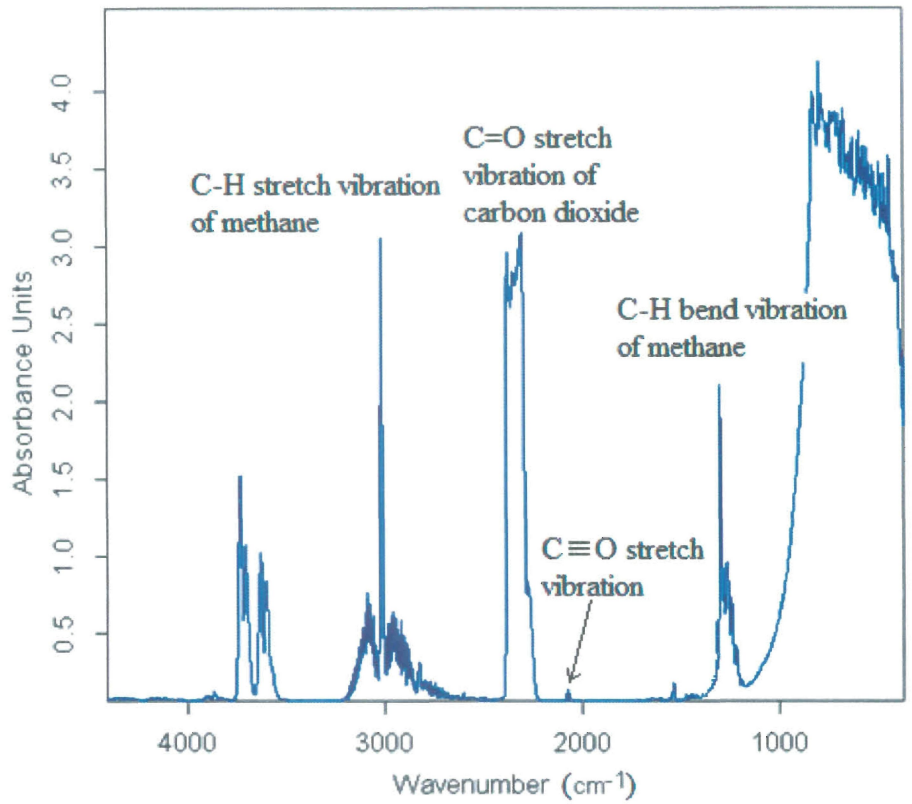

Figure 6.23 The FTIR-spectrum of the 5 hours excited methane and carbon dioxide gas mixture at 1.6 μm.

The spectrum shows the peak intensities in absorbance as a function of the wavenumber. Table 6.16 gives the characterization of the peaks present in the FTIR-spectrum of figure 6.23.

Table 6.16 Infrared characterization of peaks in methane and carbon dioxide mixture

Wavenumber (cm^{-1})	Intensity	Description	Remarks
737.34	Strong	C=O bend vibration	ν_2 fundamental of CO_2

1303.14	Strong	C-H asymmetric bend vibration	v_4 fundamental of CH_4
1354.92	Medium - Strong	C=O symmetrical stretch vibration	v_1 fundamental of CO_2
1540	Weak - Medium	C-H symmetric bend vibration	v_2 fundamental of CH_4
2100	Weak	C≡O stretch vibration	Only vibrational mode of CO Thus possible CO present
2379.62	Medium	C=O asymmetrical stretch vibration	v_3 fundamental of CO_2 Thus CO_2 present in mixture
2949.84	Medium	C-H symmetric stretch vibration	v_1 fundamental of CH_4
3016.2	Strong	C-H asymmetric stretch vibration	v_3 fundamental of CH_4 Thus CH_4 present in mixture
3628.13	Medium	OH stretch vibration	Possible alcohol present

Again as in table 6.15, the experimental data in table 6.16 suggest that both methane and carbon dioxide are still present in the gas mixture. The C≡O vibrational mode is present in the spectrum (figure 6.23) but at a very low intensity. This suggests that carbon dioxide has possibly formed during the excitation reaction. The absorption peak at 3628.13 cm^{-1} suggests that traces of OH stretch vibrations are possibly present in the sample.

The measured energy for the corresponding time intervals is shown in figure 6.24.

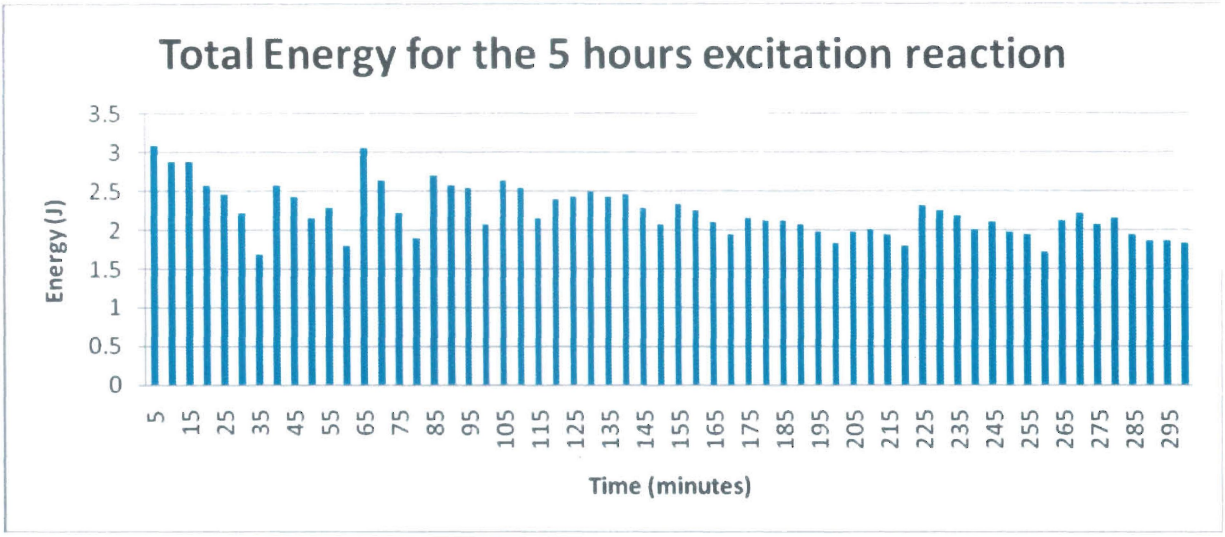

Figure 6.24 The measured energy put into the system for the five hours mixed gas excitation experiment.

This gives a total energy of 133.92 J entered into the system. This is much less that the three hours experiment. The reason for this is because the average pulse energy has decreased due to the instability of the laser system (see table 6.17). The average pulse energy and the calculated average fluence of the system are summarized in table 6.17.

Table 6.17 Measured pulse energy with calculated fluence

Time (min)	Energy (mJ/pulse)	Fluence (J/cm^2)
5	1.03	0.03279
10	0.96	0.03056
15	0.96	0.03056
20	0.86	0.02737
25	0.82	0.02610
30	0.74	0.02355
35	0.56	0.01783
40	0.86	0.02737
45	0.81	0.02578
50	0.72	0.02292
55	0.76	0.02419
60	0.6	0.01910
65	1.02	0.03247
70	0.88	0.02801
75	0.74	0.02355

80	0.63	0.02005
85	0.9	0.02865
90	0.86	0.02737
95	0.85	0.02706
100	0.69	0.02196
105	0.88	0.02801
110	0.85	0.02706
115	0.72	0.02292
120	0.8	0.02546
125	0.81	0.02578
130	0.83	0.02642
135	0.81	0.02578
140	0.82	0.02610
145	0.76	0.02419
150	0.69	0.02196
155	0.78	0.02483
160	0.75	0.02387
165	0.7	0.02228
170	0.65	0.02069
175	0.72	0.02292
180	0.71	0.02260
185	0.71	0.02260
190	0.69	0.02196
195	0.66	0.02101
200	0.61	0.01942
205	0.66	0.02101
210	0.67	0.02133
215	0.65	0.02069
220	0.6	0.01910
225	0.77	0.02451
230	0.75	0.02387
235	0.73	0.02324
240	0.67	0.02133
245	0.7	0.02228
250	0.66	0.02101
255	0.65	0.02069
260	0.57	0.01814
265	0.71	0.02260
270	0.74	0.02355
275	0.69	0.02196
280	0.72	0.02292
285	0.65	0.02069

290	0.62	0.01974
295	0.62	0.01974
300	0.61	0.01942
	0.74	0.02368

The data suggest that the average pulse energy and average fluence of the entire five hour-experiment was 0.74 mJ and 0.02368 J/cm^2 respectively, with a beam area of 0.031416 cm^2. The average power for the three hour-experiment is then calculated as follows:

$$P = E_{pulse} \times f$$
$$= (0.744 \text{ mJ}) \times 10 \text{ Hz}$$
$$= 7.44 \text{ mW}$$

The average fluence and power of the five hour-experiment is clearly much less than that of the three hours experiment. This is caused by the instability of the nanosecond laser system. As a result, the shorter three hour excitation experiment which delivered more energy per second (higher power) than the five hour experiment, was more efficient throughout the three hour-irradiation process than the five hour-irradiation process.

6.3 Femtosecond excitation reactions

This section will discuss the details of the results obtained with the femtosecond excitation reactions. The results comprise the characterization of vibrational spectra with Fourier transform infrared spectroscopy (FTIR). Calculations concerning the energy introduced into the system are given for each reaction.

6.3.1 Methane reacting with itself

The reaction of methane with itself at an excitation wavelength of 1.6 μm is described in this section.

6.3.1.1 Three hours experiment

Figure 6.25 shows the FTIR-spectrum of methane taken after 3 hours of excitation. The spectrum is measured in absorbance as a function of wavelength.

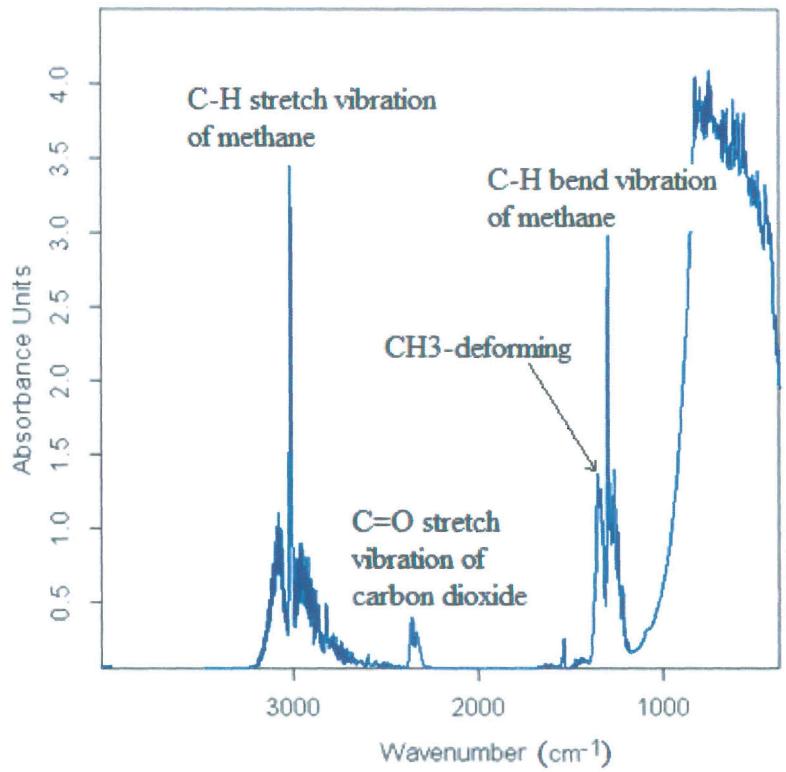

Figure 6.25 FTIR-spectrum of methane after three hours of excitation at 1.6 μm.

Table 6.18 gives the characterization of the peaks present in the FTIR-spectrum of figure 6.25.

Table 6.18 Infrared characterization of peaks in methane FTIR-spectrum

Wavenumber (cm^{-1})	Intensity	Description	Remarks
752.1	Strong	C-C deforming bend vibration	v_9 fundamental of C_2H_6
828.2	Strong	C-H bend vibration	Cis- alkene
1301.74	strong	C-H asymmetric bend vibration	v_4 fundamental of CH_4
1354.17	Medium	CH_3-deforming vibration	v_6 fundamental of C_2H_6
1539.59	Weak	CH_3-deforming vibration	v_8 fundamental of C_2H_6

		C-H symmetric bend vibration	v_2 fundamental of CH_4
2906.87	Weak - Medium	C-H symmetric stretch vibration	v_1 fundamental of CH_4 v_5 fundamental of C_2H_6
2979.04	Strong	C-H asymmetric stretch vibration	v_3 fundamental of CH_4 v_7 fundamental of C_2H_6 Thus possible CH_4 and C_2H_6 present
3112.96	Weak	=C-H stretch vibration	Cis- alkene Thus possible alkene present

The data in table 6.18 suggest that ethane has possibly formed during the excitation of methane. However, only further analysis of the sample would confirm this. The absorption peaks at ~2300 cm^{-1} in figure 6.15 have again decreased in figure 6.25as in figure 6.16 which suggests that possibly dissociation of carbon dioxide has occurred. The resulting oxidative coupling of methane or as previously explained, possible non-oxidative coupling of methane, therefore explains the =C–H stretch vibrations present in the sample.

In order to calculate the pulse- and total energy of the 3 hour-experiment, it is necessary to convert the measured energy from mW to mJ. By definition, 1 W is equal to 1 J/s. The average power transferred by the system for the entire three hour-experiment is 52 mW (52 mJ/s) with a repetition rate of 1 KHz (1000 s^{-1}). The pulse energy can then be calculated as follows:

$$E_{pulse} = \frac{Energy\ per\ second}{frequency}$$

$$= \frac{52\ mJ.s^{-1}}{1000\ s^{-1}}$$

$$= 0.052\ mJ/pulse$$

The total energy for the entire three hours is calculated as follows:

Number of pulses in three hours = 10800 s × 1000 pulses

$$= 1.08 \times 10^7 \text{ pulses}$$

Therefore,

$$E_{Total} = E_{pulse} \times Total\ number\ of\ pulses$$
$$= (0.052\ \text{mJ/pulse}) \times (1.08 \times 10^{7}\ \text{pulses})$$
$$= 5.616. \times 10^{5}\ \text{mJ}$$
$$= 561.6\ \text{J}.$$

The average fluence can then be calculated:

$$Fluence_{Avg} = \frac{E_{pulse}}{Contact\ Area}$$
$$= \frac{0.052\ mJ}{0.031416\ cm^2}$$
$$= 1.655\ \text{mJ/cm}^2$$
$$= 1.655 \times 10^{-3}\ \text{J/cm}^2.$$

The calculations show that the average pulse energy and therefore the average fluence, of this femtosecond experiment is much lower than that of the corresponding nanosecond experiment. However, the total energy transferred from the femtosecond laser system is much higher than that of the nanosecond laser system and because the repetition rate is also much higher, the work done by the laser system is much higher. This results in more energy being absorbed by the reactant(s) in a smaller time-scale, which therefore increases the laser's excitation efficiency.

6.3.1.2 Five hours experiment

Figure 6.26 shows the FTIR-spectrum of methane taken after 5 hours of excitation. The spectrum is measured in absorbance as a function of wavelength.

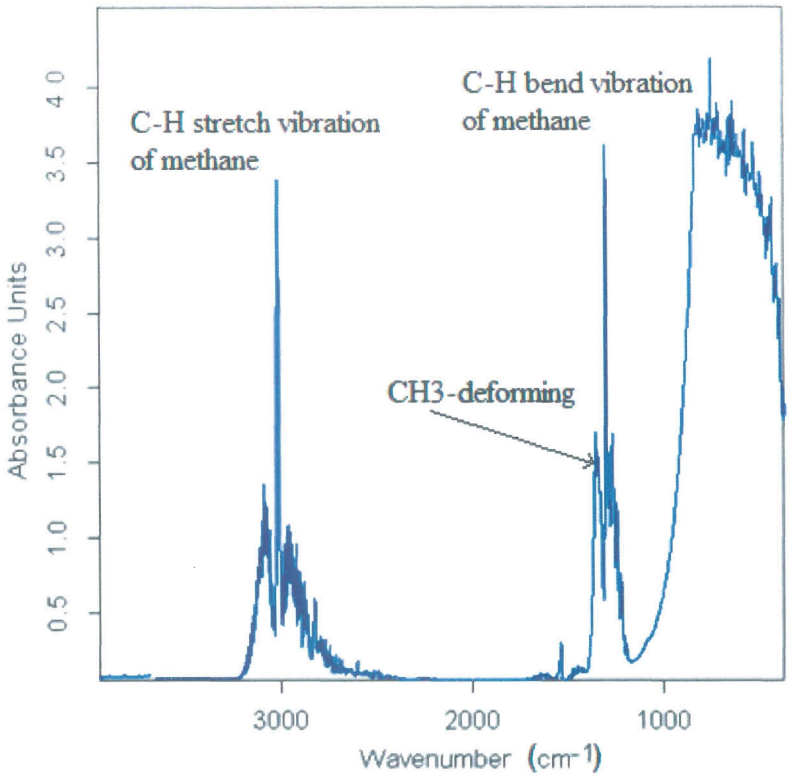

Figure 6.26 FTIR-spectrum of methane after five hours of excitation at 1.6 μm.

Table 6.19 gives the characterization of the peaks present in the FTIR-spectrum of figure 6.26.

Table 6.19 Infrared characterization of peaks in methane FTIR-spectrum

Wavenumber (cm^{-1})	Intensity	Description	Remarks
750.44	Strong	C-C deforming bend vibration	v_9 fundamental of C_2H_6
812.38	Strong	C-H bend vibration	Cis- alkene
1302.42	strong	C-H asymmetric bend vibration	v_4 fundamental of CH_4
1355.22	Medium	CH_3-deforming vibration	v_6 fundamental of C_2H_6
1540.48	Weak	CH_3-deforming vibration	v_8 fundamental of C_2H_6
2908.88	Weak - Medium	C-H symmetric bend vibration C-H symmetric stretch vibration	v_2 fundamental of CH_4 v_1 fundamental of CH_4 v_5 fundamental of C_2H_6

2981.05	Strong	C-H asymmetric stretch vibration	v_3 fundamental of CH_4 v_7 fundamental of C_2H_6 Thus possible CH_4 and C_2H_6 present
3097.1	Weak	=C-H stretch vibration	Cis- alkene Thus possible alkene present

The data in table 6.19 suggest that methane is still present in the sample and that ethane has possibly formed during the excitation experiment. The absorption peaks at ~2300 cm^{-1} in figure 6.15 have completely disappeared in figure 6.26 which suggests that possibly complete dissociation of carbon dioxide has occurred. The resulting non-oxidative coupling of methane as previously explained, therefore explains the =C–H stretch vibrations present in the sample.

The average power delivered by the femtosecond laser system for the five hour-experiment was 55 mW. From this the pulse energy is calculated as follows:

$$E_{pulse} = \frac{Energy\ per\ second}{frequency}$$
$$= \frac{55\ mJ.s^{-1}}{1000\ s^{-1}}$$
$$= 0.055\ \text{mJ/pulse}$$

The total energy for the entire five hours is calculated as follows:
Number of pulses in five hours = 18000 s × 1000 pulses
$= 1.8\times10^7$ pulses

Therefore,

$$E_{Total} = E_{pulse} \times Total\ number\ of\ pulses$$
$$= (0.055\ \text{mJ/pulse})\times(1.8\times10^7\ \text{pulses})$$
$$= 9.9\times10^5\ \text{mJ}$$
$$= 990\ \text{J}.$$

The average fluence can then be calculated:

$$Fluence_{Avg} = \frac{E_{pulse}}{Contact\ Area}$$
$$= \frac{0.055\ mJ}{0.031416\ cm^2}$$
$$= 1.7507\ \text{mJ/cm}^2$$
$$= 1.7507\times10^{-3}\ \text{J/cm}^2.$$

For the five hour-experiment, the power was slightly higher than that of the three hour-experiment and due to the extended duration, the calculations suggested that the pulse- and total energy was higher for the five hour-experiment than for the three hour-experiment. This could have caused the complete dissociation of the carbon dioxide that was witnessed in the analysed FTIR-results.

6.3.2 Methane and carbon dioxide reactions

The reaction of methane and carbon dioxide at an excitation wavelength of 1.6 μm is described in this section.

6.3.2.1 Three hours experiment

Figure 6.27 shows the FTIR-spectrum of the methane and carbon dioxide mixture taken after 3 hours of excitation. The spectrum is measured in absorbance as a function of wavelength.

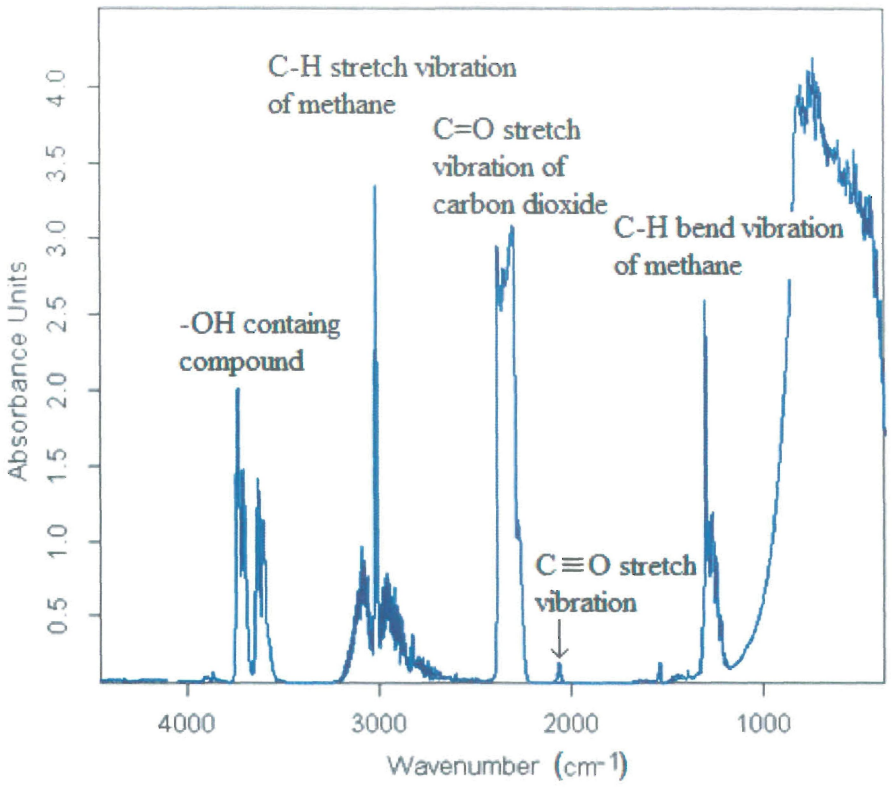

Figure 6.27 FTIR-spectrum of methane and carbon dioxide mixture after 3 hours of excitation at 1.6 μm.

Table 6.20 gives the characterization of the peaks present in the FTIR-spectrum of figure 6.27.

Table 6.20 Infrared characterization of peaks in methane and carbon dioxide mixture

Wavenumber (cm^{-1})	Intensity	Description	Remarks
741.33	Strong	C=O bend vibration	v_2 fundamental of CO_2
1302.85	Strong	C-H asymmetric bend vibration	v_4 fundamental of CH_4
1354.98	Medium - Strong	C=O symmetrical stretch vibration	v_1 fundamental of CO_2
1550	Very Weak	C-H symmetric bend vibration	v_2 fundamental of CH_4
2100	Weak	C≡O stretch vibration	Only vibrational mode of CO Thus possible CO present

2301.15	Strong	C=O asymmetrical stretch vibration	v_3 fundamental of CO_2 Thus CO_2 present in mixture
2939.49	Weak	C-H symmetric stretch vibration	v_1 fundamental of CH_4
3016	Strong	C-H asymmetric stretch vibration	v_3 fundamental of CH_4 Thus CH_4 present in mixture
3627.98	Medium	OH stretch vibration	Possible alcohol present

The data in table 6.20 suggest that methane and carbon dioxide is still present in the mixture. The spectrum again shows a small absorption peak at ~2100 cm^{-1} that should indicate that carbon monoxide formed during the excitation process. The absorption peak at 3627.98 cm^{-1} suggests that traces of OH stretch vibrations are possibly present in the sample.

The average power delivered by the femtosecond laser system for the three hour-experiment was 40 mW. From this the pulse energy is calculated as follows:

$$E_{pulse} = \frac{Energy\ per\ second}{frequency}$$
$$= \frac{40\ mJ.s^{-1}}{1000\ s^{-1}}$$
$$= 0.04\ \text{mJ/pulse}$$

The total energy for the entire three hours is calculated as follows:
Number of pulses in three hours = 10800 s × 1000 pulses
$= 1.08\times10^7$ pulses

Therefore,

$$E_{Total} = E_{pulse} \times Total\ number\ of\ pulses$$
$$= (0.04\ \text{mJ/pulse})\times(1.08\times10^7\ \text{pulses})$$
$$= 4.32\times10^5\ \text{mJ}$$
$$= 432\ \text{J}.$$

The average fluence can then be calculated:

$$Fluence_{Avg} = \frac{E_{pulse}}{Contact\ Area}$$
$$= \frac{0.04\ mJ}{0.031416\ cm^2}$$
$$= 1.27323\ mJ/cm^2$$
$$= 1.27323 \times 10^{-3}\ J/cm^2.$$

The calculations show that for the femtosecond laser experiments the average pulse energy and fluence is much less than the nanosecond experiments. However, the total energy and power of the femtosecond laser system is much higher than the nanosecond laser system.

6.3.2.2 Five hours experiment

Figure 6.28 shows the FTIR-spectrum of the methane and carbon dioxide mixture taken after 5 hours of excitation. The spectrum is measured in absorbance as a function of wavelength.

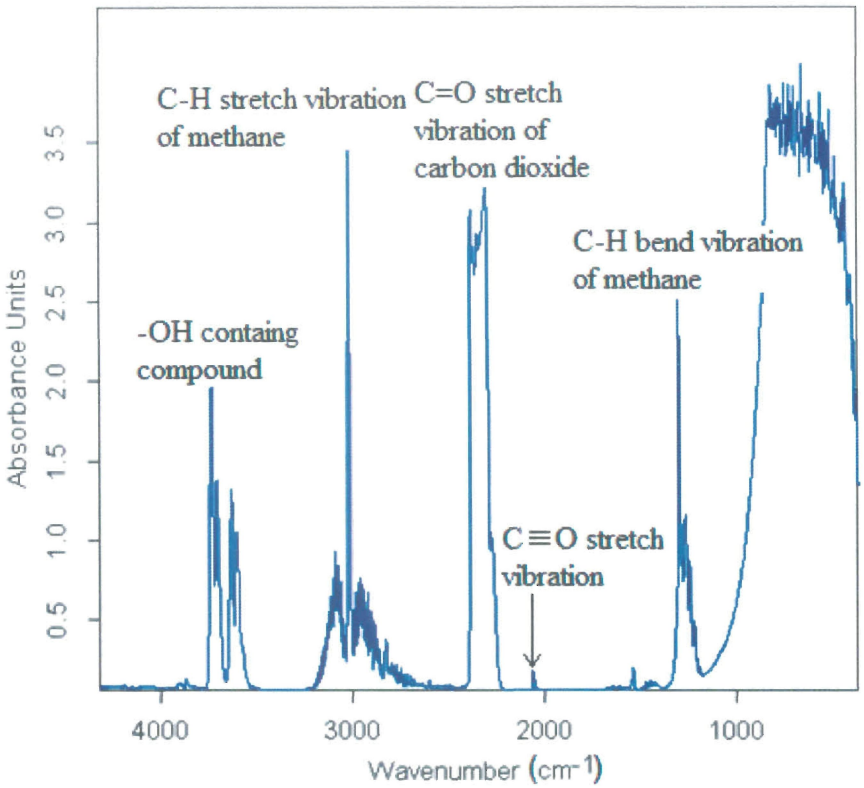

Figure 6.28 FTIR-spectrum of methane and carbon dioxide mixture after 5 hours of excitation at 1.6 μm.

Table 6.21 gives the characterization of the peaks present in the FTIR-spectrum of figure 6.28.

Table 6.21 Infrared characterization of peaks in methane and carbon dioxide mixture

Wavenumber (cm^{-1})	Intensity	Description	Remarks
749.03	Strong	C=O bend vibration	v_2 fundamental of CO_2
1302.88	Strong	C-H asymmetric bend vibration	v_4 fundamental of CH_4
1354.96	Medium - Strong	C=O symmetrical stretch vibration	v_1 fundamental of CO_2
1550	Very Weak	C-H symmetric bend vibration	v_2 fundamental of CH_4
2100	Weak	C≡O stretch vibration	Only vibrational mode of CO Thus possible CO present

2303.97	Strong	C=O asymmetrical stretch vibration	v_3 fundamental of CO_2 Thus CO_2 present in mixture
2939.48	Weak	C-H symmetric stretch vibration	v_1 fundamental of CH_4
3016.03	Strong	C-H asymmetric stretch vibration	v_3 fundamental of CH_4 Thus CH_4 present in mixture
3628.1	Medium	OH stretch vibration	Possible alcohol present

The data suggest that only methane and carbon dioxide is present in the mixture. The spectrum of figure 6.28 is almost identical to figure 6.27 and therefore suggests that the C≡O absorption peak gives an indication that the reaction occurred during the excitation process. The absorption peak at 3628.1 cm^{-1} suggests that traces of OH stretch vibrations are possibly present in the sample.
The average power delivered by the femtosecond laser system for the five hour-experiment was 45 mW. From this the pulse energy is calculated as follows:

$$E_{pulse} = \frac{Energy\ per\ second}{frequency}$$
$$= \frac{45\ mJ.s^{-1}}{1000\ s^{-1}}$$
$$= 0.045\ \text{mJ/pulse}$$

The total energy for the entire three hours is calculated as follows:
Number of pulses in five hours = 18000 s × 1000 pulses $= 1.8\times10^7$ pulses

Therefore,

$$E_{Total} = E_{pulse} \times Total\ number\ of\ pulses$$
$$= (0.045\ \text{mJ/pulse})\times(1.8\times10^7\ \text{pulses})$$
$$= 8.1\times10^5\ \text{mJ}$$
$$= 810\ \text{J}.$$

The average fluence can then be calculated:

$$Fluence_{Avg} = \frac{E_{pulse}}{Contact\ Area}$$
$$= \frac{0.045\ mJ}{0.031416\ cm^2}$$
$$= 1.4324\ \text{mJ/cm}^2$$
$$= 1.4324 \times 10^{-3}\ \text{J/cm}^2.$$

The results of the femtosecond excitation experiments suggests that it is more desirable to use the femtosecond laser system to irradiate the samples since it is more stable and delivers more power than the nanosecond laser system.

Chapter 7
Summary and conclusions

7.1 Summary

In this study, it was attempted to activate methane in a reaction with itself and with carbon dioxide by means of laser excitation. Molecular modelling was used to study some properties of the molecules participating and produced in the reactions and help make predictions on the outcomes of the reactions.

7.1.1 Molecular modelling

A series of calculations were performed to determine the properties of methane, ethane and carbon dioxide. These calculations included geometric optimization-, electronic state-, excited state- and vibrational state calculations. Material Studios and Spartan '06 were software packages used to perform the calculations.

It was found that the results of the geometry optimization calculations corresponded well with the values from literature. Electronic state calculations verified that the molecular orbital diagram of methane had four bonding molecular orbitals of which three were of same energy and one with lower energy. The results showed that the HOMO was a triple degenerate molecular orbital of energy -13.56457 eV and the LUMO a single molecular orbital of energy 5.43626 eV. Figure 7.1 (also figure 6.1) gives an illustration of the calculated molecular orbital of methane.

Excited state calculations of the first excited state of methane revealed that there is an increase in the bond energy of one of the C–H bonds. This increase in bond energy indicates the decrease in stability of the molecule which causes the bond between the hydrogen and carbon to weaken. The data showed that at ~3.7 Å the C–H bond energy would have increased to ~-310 kcal/mol which would indicate the point of breaking. This is equal to an energy increase of ~140 kcal/mol (~580 kJ/mol) which gives a reasonable correlation to the known dissociation energy of the C–H bond of methane.

Results from the vibrational state calculations corresponded well with the values from literature for all the studied molecules. Fundamental modes were calculated with their respective contributions to identify the strongest fundamental vibration.

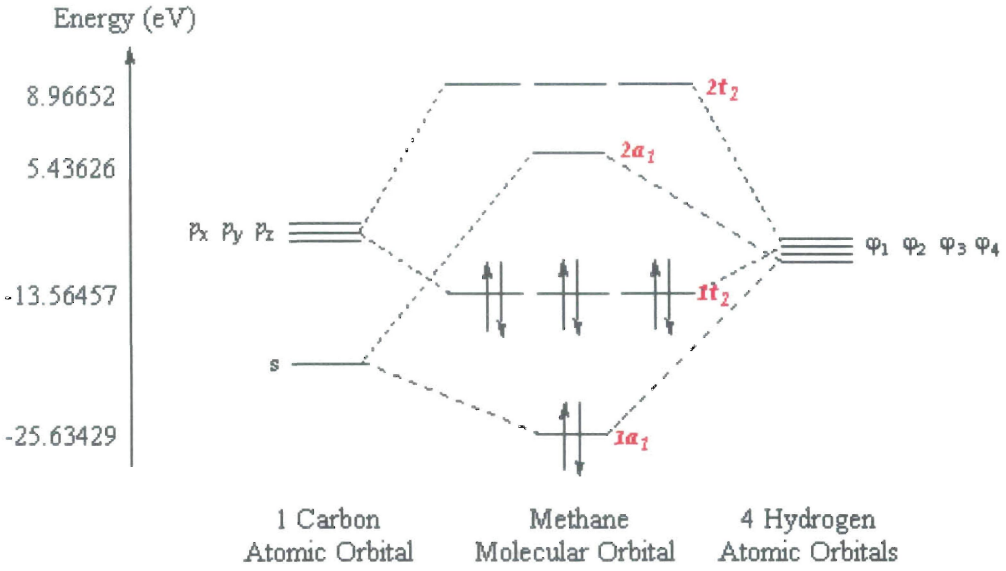

Figure 7.1 The calculated molecular orbital diagram of methane with average molecular orbital energies.

Table 7.1 lists the strongest fundamental for each of the studied molecules with their respective wavelengths. These values were calculated with the DMol^3 method and DND basis set. This was done to determine the most desirable wavelength to use for the excitation of methane.

		Wavelength (cm^{-1})		
Molecule	Fundamental	DMol^3	Literature	Reference
Methane	v_3	3096.7	3030	Hess, 1980
Carbon dioxide	v_3	2428.1	2348.1	http://www.chemtube3d.com/vibrationsCO2.htm
Ethane	v_5	2958.1	2895.67	Hepp, 1999

The results showed that the ν_3 fundamental of methane was its strongest vibrational mode. This wavelength however, was difficult to generate with the laser systems that were used to perform the excitation experiments, so instead the much easier accessible wavelength (1.67 μm) of its overtone ($2\nu_3$) was chosen. The calculated infrared spectra were also used to identify and characterize the absorption peaks found in the experimentally obtained results.

7.1.2 Excitation experiments

Two main reactions were investigated; the first was the reaction in which methane reacted with itself and the second, where methane reacted with carbon dioxide. For each reaction the sample was excited by two different laser systems. These systems were designed and set up to allow the laser light to pass through the gas cell, after which the energy of the light could be measured. The first laser system was a seeded Nd:YAG powered nanosecond laser system which used a Lambda Physik optical parametric power oscillator (OPPO) to generate the desired wavelength of 1.6 μm. The second system was a Ti:Sapphire powered femtosecond laser system which used an optical parametric amplifier (OPA) to generate the desired wavelength of 1.6 μm. For all experiments the high pressure gas cell was filled to a pressure of 150 kPa and placed in the necessary position.

The experiments were divided into two main categories; the first was excitation with the nanosecond laser system and the second, excitation with the femtosecond laser system. Each category consisted of two excitation experiments in which the excitation time for each reaction was varied. After excitation, the sample was analysed with the use of Fourier transform infrared (FTIR) spectroscopy.

The FTIR-results for the self-reacting methane experiments revealed that the samples contained traces of ethane and ethylene after excitation took place. This meant that the reaction did produce ethane for both laser systems used which confirmed that ethane could indeed be produced from infrared photo-excitation of methane. However, the discovery of ethylene traces suggested that oxidative- or non-oxidative coupling of methane (NOCM) occurred during excitation. Figure 7.2 illustrates a complex model of the OCM reaction over a La_2O_3/CaO catalyst as

determined by Stansch [Stansch, 1994]. The scheme included nine heterogeneously catalysed- and one homogeneous non-catalytic (reaction 8) reactions. These reactions are as follows:

(1) Total oxidation of methane to carbon dioxide,
(2) Oxidative coupling of methane to ethane,
(3) Partial oxidation of methane to carbon monoxide,
(4) Oxidation of carbon monoxide to carbon dioxide,
(5) Oxidative dehydrogenation of ethane to ethylene,
(6) Oxidation of ethylene to carbon monoxide,
(7) Steam reforming of ethylene,
(8) Thermal dehydrogenation of ethane to ethylene,
(9) Conversion of CO to CO_2 and vice versa by water-gas shift reaction.

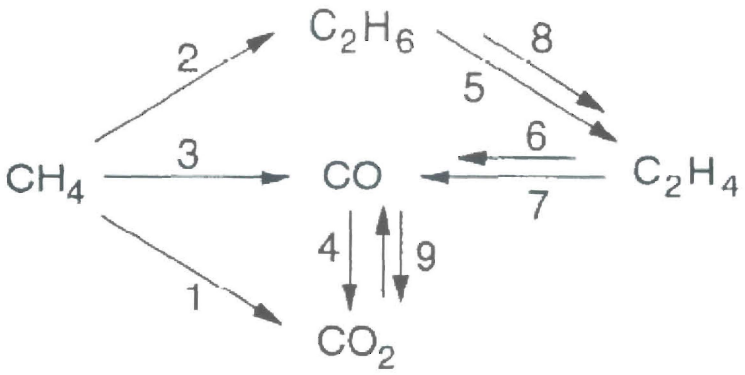

(1) $CH_4 + 2\,O_2 \longrightarrow CO_2 + 2\,H_2O$

(2) $CH_4 + 0.5\,O_2 \longrightarrow C_2H_6 + H_2O$

(3) $CH_4 + O_2 \longrightarrow CO + H_2O$

(4) $CO + 0.5\,O_2 \longrightarrow CO_2$

(5) $C_2H_6 + 0.5\,O_2 \longrightarrow C_2H_4 + 2\,H_2O$

(6) $C_2H_4 + 2\,O_2 \longrightarrow 2\,CO + 2\,H_2O$

(7) $C_2H_4 + 2\,H_2O \longrightarrow 2\,CO + 4\,H_2$

(8) $C_2H_6 \longrightarrow C_2H_4 + H_2$

(9) $CO + H_2O \rightleftharpoons CO_2 + H_2$

Figure 7.2 Reaction scheme of the OCM over the La_2O_3/CaO catalyst [Stansch, 1994].

For non-oxidative coupling of methane, ethane and hydrogen are produced in the same manner as the photodissociation of methane to ethane in the atmosphere. As discussed in chapter 6, dissociation of methane occurs to form methyl radicals, which then combine to form ethane. This reaction is initiated by the absorption of VUV-radiation (<160 nm) which corresponds to electronic excitation. The UV-absorption spectrum of methane reveals that strong absorption occurs at ~126 nm which is ideal for conducting experiments that use photo-irradiation from a broadband VUV-lamp. This was the case for the study by Yuliati and co-workers that used photocatalysis to produce a number of C_2-hydrocarbons (ethane and

ethylene) over a gallium oxide photocatalyst [Yuliati, 2008]. The findings of the study suggested that thermal energy does not greatly enhance the dissociation of methane which suggests that the process can be performed at room temperature.
For this study however, the results revealed that coupling of methane did occur for a system in which no photocatalyst was used and in which the excitation wavelength was in the near-infrared region. Mostly ab initio studies on these molecules in the infrared region have been done till date and very little research on NOCM in the infrared region. This opens the door for enormous research on photo-excitation in the IR- and UV-region for this process and others that require catalysts.

Figure 7.3 shows the FTIR-spectra of the self-reacting methane reactions with their respective average power values. The spectra illustrate how the varied power of the different laser systems influenced the results. This suggests that the yield or effectiveness of the reaction is dependent on the power of the laser system (number of photons per second).

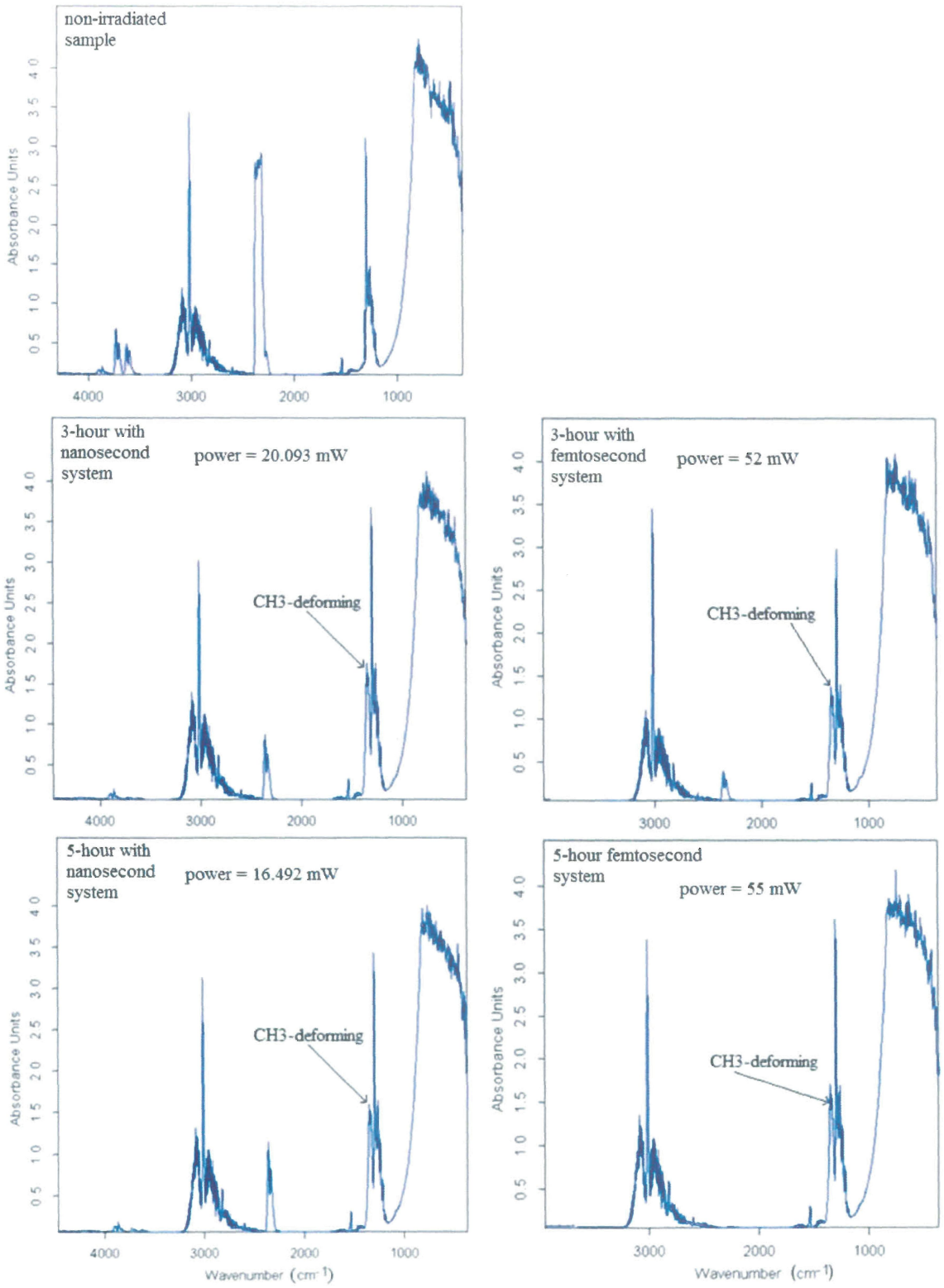

Figure 7.3 FTIR-spectra of the self-reacting methane reactions.

The FTIR-results of the methane and carbon dioxide reaction revealed that in all experiments, there were traces of C≡O stretch vibrations at ~2100 cm^{-1}. In the endothermic reaction of methane and carbon dioxide, carbon monoxide and hydrogen is produced. This process is called dry reforming of methane (DRM). Although the intensity of the C≡O absorption peak was very low due to the small dipole moment of the molecule, it still suggested that the reduction of carbon dioxide by methane took place. The cause for the small dipolemoment is as a result of the HOMO's energy being closer to the p-orbitals of the carbon which causes a greater electron density near the carbon. Also, traces of OH stretch vibrations were found at ~3600 cm^{-1} in all the samples of the methane and carbon dioxide experiments. The presence of these OH stretch vibrations together with the C≡O vibrations suggest that a different reaction could have occurred during the irradiation process. The suggested reaction is as follows:

$$CH_4 + CO_2 \rightarrow CO + CH_3OH$$

Here, the reaction of methane and carbon dioxide produces carbon monoxide and methanol. The results therefore suggest that methanol was formed instead of hydrogen. This also suggests that under these conditions, methane would prefer to undergo the coupling reaction where methanol is formed, instead of the decomposition reaction.

Figure 7.4 shows the FTIR-spectra of the methane and carbon dioxide mixtures with their respective average power values. By comparing the spectra, the influence of the higher power femtosecond laser system can be seen through the increase of the carbon monoxide peak at ~2100 cm^{-1} and the OH-containing compound at ~3600 cm^{-1}.

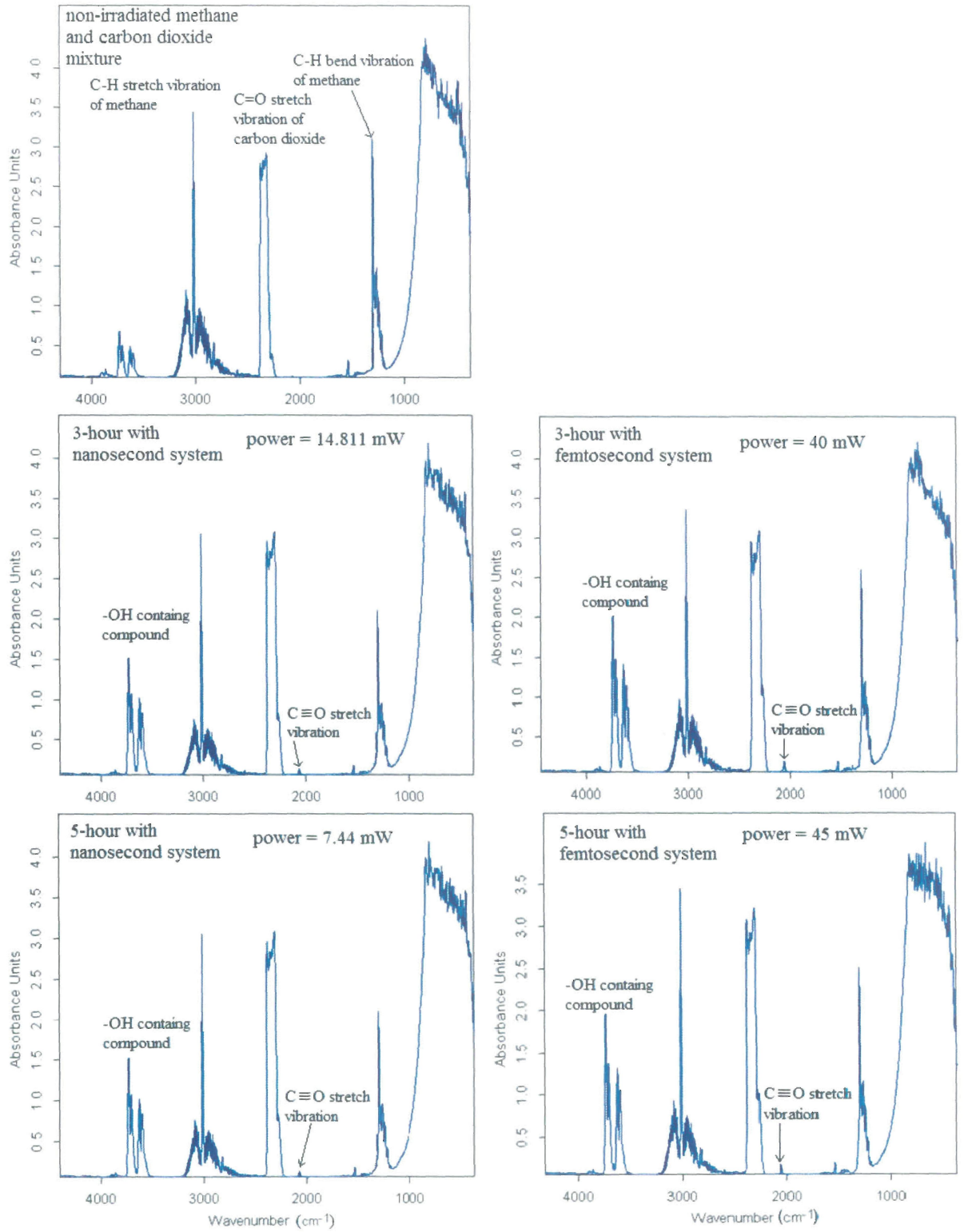

Figure 7.4 FTIR-spectra of the methane and carbon dioxide mixture reactions.

As in the self-reacting reaction of methane, the reaction of methane and carbon dioxide are commonly performed in the presence of a catalyst. The advantage of using a catalyst is that the rate of the reaction is increased but the disadvantages however are that these catalysts are expensive and deactivation of the catalyst occurs at high temperatures. Therefore, by using photo-excitation many properties such as the dynamics of these reactions can be studied under normal conditions (room temperature and atmospheric pressure). This means that for instance C–H bond activation, that is usually sensitive to the surface structure of the catalysts, can now instantly occur through the absorption of photons at the correct wavelength.

Many applications (industrial use and medical research) for lasers do already exist due to the diversity of the available lasers and from a personal perspective this property makes it ideal for future research in many different fields, especially chemistry.

7.2 Conclusion and recommendations

In this study experimental results showed that:

(1) C–H bond activation by means of infrared photo-excitation occurred,
(2) Possible oxidative- or non-oxidative coupling of methane to produce ethane is possible without the use of catalysts,
(3) Dehydrogenation of ethane to ethylene occurred,
(4) NOCM can proceed at room temperature when irradiated,
(5) Production of carbon monoxide from methane and carbon dioxide was indicated,
(6) The possible production of methanol during the methane and carbon dioxide reaction could be investigated,
(7) Methane prefers to undergo coupling reaction instead of decomposition when activated by infrared laser pulses,
(8) Photo-excitation with high-powered laser systems enables reactions with a large ΔG that normally require the use of stable catalysts and high temperatures, to occur.

Molecular modelling proved to be a useful technique to make reasonably accurate predictions on structural-, electronic- and vibrational properties on the molecules in the studied reactions.

Future work with molecular modelling could include a detailed analysis on the reaction mechanisms of the particular reactions. This analysis should describe thermodynamic properties of the reaction paths and address the aspect of intermediate states. Molecular modelling could also be used to study the surface structure of some catalysts and the influences it plays in the particular reactions.
Recommended techniques for the analysis of the products include:

(1) Gas chromatography (GC),
(2) Time-of-flight mass spectroscopy (TOF MS).

Other recommendations and future work are:

(1) Pump-probe activation experiments with femtosecond laser system to study the dynamics of intermediate states,
(2) Excitation at different wavelengths (UV- and MIR region),
(3) Experimental study on catalyst surfaces,
(4) Study on the kinetics of the reactions,
(5) Optimization of specific reaction products produced by femtosecond laser techniques.

Bibliography:

- Accelrys Inc., A Short History of Early Computing; www.mathub.com/history/compchem.html
- Accelrys Inc., Quantum Chemistry, from Schrodinger to QCPE and on; www.mathhub.com/history/quantum.html
- Ashcroft, A.T., Cheetham, A.K., Green, M.L.H. and Vernon, P.D.F., Nature 1991, 352, 225.
- Atkinson, R., Baulch, D.L., Cox, R.A., Hampson, R.F., Jr., Kerr, J.A., Troe, J., J. Chem. Ref. Data, 1992, 6, 1125.
- Boudart, M., Adv. Catal. 1969, 20, 153.
- Bray, M.R., Deeth, R.J. and Paget, V.J., Prog. Reaction Kinetics, 1996, 21, 169.
- Brownsword, R.A., Hillenkamp, M., Laurent, T., Vatsa, R.K., Volpp, H.R., Wolfrum, J., Chem. Phys. Lett., 1997, 266, 259.
- Burghgraef, H., Jansen, A.P.and Van Santen, R.A., Faraday Discuss. 1993, 96, 337.
- Chen, Q., Schweitzer, E.J.A. and Van Den Oosterkamp, P.F., Oxidative Pyrolysis of Ethane, Ind. Eng. Chem. Res., 1997, 36, 3248.
- Clark, T., A Handbook of Computational Chemistry, John Wiley and Sons, New York, 1985.
- Corness, W.D., Ha, M.P., Sun, Y., and Kollman, P.A., J. Comput. Chem. 1996, 17, 1541.
- Cornils, B. and Herrmann W.A., Applied Homogeneous Catalysis with Organometalic, 1996.
- Curtiss, L.A., Raghavachari, K., Encycl. Comput. Chem., 1998, 2, 1104.
- Davidson, E.R., Encycl. Comput. Chem., 1998, 3, 1811.
- Delley, B., J. Chem. Phys., 1990, 92, 508.
- Delley, B., J. Chem. Phys., 2000, 113, 7756.
- Delley, B., J. Phys. Chem., 1996, 100, 6107.
- Ebrahim, H.A. and Jamshidi, E., Synthesis gas production by zinc oxide reaction with methane: elimination of greenhouse gas emission form a metallurgical plant, Energy Conversion and Management, 2004, 45, 345.

- Geusic, J. E., et al., Laser oscillations in Nd-doped yttrium aluminum, yttrium gallium and gadolinium garnets, Appl. Phys. Lett., 1964, 4 (10), 182.
- Grant, G.H., Richards, W.G., Computational Chemistry, Oxford, 1995.
- Hansen, J., Sato, M., Ruedy, R., Lacis, A., Oinas, V., Global warming in the twenty-first century: An alternative scenario, Center for Climate Systems Research, Columbia University, 2000.
- Heck, A.J.R., Zare, R.N. and Chandler, D.W., J. Chem. Phys., 1996, 104, 3399.
- Hepp, M., Herman, M., Weak Combination Bands in the 3-mm Region of Ethane, Journal of Molecular Spectroscopy, 1999, 197, 56–63.
- Hertzberg, G., Molecular spectra and molecular structure, Vol. III: Electronic spectra and electronic structure of polyatomic molecules, Van Nostrand, New York, 1966.
- Hess, P., Kung, H.A., Moore, C.B., Vibration→vibration energy transfer in methane, J. Chem. Phys., 1980, 72, 5525.
- Holder, A.J., Encycl. Comput. Chem., 1998, 1, 8.
- House, J.E., Fundamentals of Quantum Mechanics, Academic Press, San Diego, 1998.
- http://content.answers.com/main/content/wp/en/1/14/Spontaneousemission.png
- http://csi.chemie.tu-darmstadt.de/ak/immel/script/redirect.cgi?filename=http://csi.chemie.tu-darmstadt.de/ak/immel/tutorials/orbitals/molecular/methane.html.
- http://en.wikipedia.org/wiki/Ethane, Access date: 2008/10/07
- http://en.wikipedia.org/wiki/Fischer-Tropsch, Access date: 2007/08/07
- http://en.wikipedia.org/wiki/Methane , Access date: 2007/02/07
- http://en.wikipedia.org/wiki/Nonlinear_optics, Access date: 2008/08/07
- http://en.wikipedia.org/wiki/Optical_parametric_oscillator, Access date: 2008/08/07
- http://en.wikipedia.org/wiki/Selection_rule, Access date: 2007/09/17
- http://en.wikipedia.org/wiki/Term_symbol, Access date: 2007/09/18
- http://en.wikipedia.org/wiki/Wave-particle_duality, Access date: 2007/09/18
- http://physics.schooltool.nl/quantumoptics/images/content/emission.gif

- http://upload.wikimedia.org/wikipedia/en/thumb/0/07/Kerr-lens_Modelocking.png/400px-Kerr-lens_Modelocking.png
- http://www.accelrys.com
- http://www.ch.ic.ac.uk/vchemlib/course/mo_theory/main.html
- http://www.cem.msu.edu/~reusch/VirtualText/Spectrpy/UV-Vis/spectrum.htm
- http://www.chem.wayne.edu/~hbs/chm6440/PES.gif
- http://www.chemtube3d.com/vibrationsCH4.htm.
- http://www.chemtube3d.com/vibrationsCO2.htm.
- http://www.ecobridge.org/content/g_cse.htm.
- http://www.fml.ethz.ch/education/CatalReactEngin/Methane_Activation
- http://www.hydrocarbons-technology.com/
- http://www.kayelaby.npl.co.uk/chemistry/3_7/3_7_3.html
- http://www.midac.com/apnotes/Tn-100.PDF
- http://www.mike-willis.com/Tutorial/PF_files/Picture12.jpg
- http://www.mrnuke.com/wsupics/work/pump-probe.jpg
- http://www.naturalgas.org/business/demand.asp#industrydemand
- http://www.nature.comnaturejournalv421n6925imagesnature01430-f1.2.jpg
- http://www.science.uwaterloo.ca/~cchieh/cact/c120/bondel.html
- http://www.thebigview.com/spacetime/quantumtheory.html
- http://www.wavefun.com
- http://www.worldoil.com/Magazine/MAGAZINE_DETAIL.asp?ART_ID=2808&MONTH_YEAR=Feb
- http://xbeams.chem.yale.edu/~batista/vvv/node29.html.
- Hu, Y.H., Ruckenstein, E., Adv. Catal., 2004, 48, 297.
- Jachimowski, T.A., Hagedorn, C.J., Weinberg, W.H., Surf. Sci., 1997, 393, 126.
- Jensen, F., Introduction to Computational Chemistry, John Wiley and Sons, New York, 1999.
- Karplus, S., Bersohn, R., J. Chem. Phys., 1969, 51, 2040.
- Kato, Y., Yoshida, H., Satsuma, A., Hattori, T., Micro. Mesopor., 2002, 51, 223.

- Keller, U., Knose, W.H., 'tHooft, G.W., Roskos, H., Woodward, T.R., Cunningham, J.E., Sivco, D.L.,Cho, A.Y., Adv. Sol. State Lasers, 1991, 10, 115.
- Klier, K., Hess, J.S. and Herman R.G., J. Chem. Phys. 1997, 107, 4033.
- Le Bel, J.A., Bull. Soc. Chim. Fr., 1874, 22, 337.
- Levine, J.S., The photochemistry of atmospheres, Ed. Levine, J.S., Academic Press, New York, 1985.
- Lewis, D.F., Chem. Rev., 1986, 86, 1111.
- Mahan, B.H., Mandal, R., J. Chem. Phys., 1962, 37, 207.
- Mark, M.F. and Maier, W.F., J. Catal., 1996, 164, 122.
- McMaster, M.C.and Madix, R.J., J. Chem. Phys. 1993, 98, 15.
- Pauling, L., The nature of the chemical bond, Ithaca, 1940.
- Robin, M.B., Higher excited states of polyatomic molecules, Vol. I, Academic Press, New York, 1974.
- Ross, J.R.H., Catal. Today, 2005, 100, 151.
- Rostrum-Nielsen, J.R. and Bak Hansen, J.H., J. Catal., 1993, 144, 38.
- Roterman, I.K., Gibson, K.D., Scheraga, J Biomol. Struct. Dynam., 1989, 7, 421.
- Rullière, C., Femtosecond Laser Pulses, Springer, Second Ed., 2003.
- Sabatier, P., Senderens, J.B., New Synthesis of methane, Compt. Rend., 1902, 134, 514.
- Sagadeev, E.V. and Sagadeev, V.V., High Temperatures of Carbon Compounds, 2004, 42, 3, 421.
- Science News, Jun. 2005, 25, 167, 26, 410.
- Seets, D.C., Reeves, C.T., Ferguson, B.A., Wheeler, M.C., Mullins, C.B., J. Chem. Phys., 1997, 107, 10229.
- Solomon, S., Qin, D., Manning, M., Alley, R.B., Berntsen, T., Bindoff, N.L., Chen, Z., Chidthaisong, A., Gregory, J.M., Hegerl, G.C., Heimann, M., Hewitson, B., Hoskins, B.J., Joos, F., Jouzel, J., Kattsov, V., Lohmann, U., Matsuno, T., Molina, M., Nicholls, N., Overpeck, J., Raga, G., Ramaswamy, V., Ren, J., Rusticucci, M., Somerville, R., Stocker, T.F., Whetton, P., Wood, R.A., Wratt, D., Technical Summary. In: Climate Change 2007: The Physical Science Basis. Contribution of Working Group I to the Fourth

Assessment Report of the Intergovernmental Panel on Climate Change, Cambridge University Press, Cambridge, United Kingdom and New York, NY, USA, 2007.

- Stansch, Z., Ph.D. thesis Ruhr-University Bochum, Bochum, 1994.
- Stewart, J.J.P., Encycl. Comput. Chem., 1998, 3, 2080.
- Telle, H.H., Ureña, A.G., Donovan, R.J., Laser chemistry: spectroscopy, dynamics and applications, John Wiley & Sons Ltd, 2007.
- Thauer, R.K., Biochemistry of Methanogenesis: a Tribute to Marjory Stephenson, Microbiology, 1998, 144, 2377.
- Van Leeuwen, P.W.N.M., Morokuma, K. and Van Lenthe, J.H., Theoretical Aspects of Homogeneous Catalysis, Kluwer Academic Publishers, 1995.
- Van Sittert, C.G.C.E., Lachmann, G., Molecular Modeling, 2006.
- Van't Hoff, J.H., La Chimie dans l'Espace, 1875.
- Watanabe, K., J. Chem. Phys., 1957, 26, 542.
- Wayne, C.E., Wayne, R.P., Photochemistry, Oxford University Press, Oxford, 1996.
- Wei, J., Iglesia, E., Angew. Chem. Int. 2004, 43, 3685.
- Wei, J., Iglesia, E., J. Catal., 2004, 225, 116.
- Wei, J., Iglesia, E., J. Phys. Chem. B, 2004, 108, 2253.
- Wei, J., Iglesia, E., J. Phys. Chem. B, 2004, 108, 4094.
- Yuliati, L., Hamajima, T., Hattori, T., Yoshida, H., Chem. Commun., 2005, 4824.
- Yuliati, L., Itoh, H., Yoshida, H., Photocatalytic conversion of methane and carbon dioxide over gallium oxide, Chem. Phys. Letters, 2008, 452, 1-3, 178-182.
- Yuliati, L., Itoh, H., Yoshida, H., Stud. Surf. Sci. Catal., 2006, 162, 961.
- Yuliati, L., Tsubota, M., Satsuma, A., Itoh, H., Yoshida, H., J. Catal., 2006, 238, 214.
- Zewail, A.H., Rose, T.S., Rosker, M.J., Femtosecond Real-Time Observation of Wave Packet Oscillations (Resonance) in Dissociation Reactions, J. Chem. Phys., 1988, 88, 6672.